Remote Sensing Series 86

Emiliano Casalini

Imaging of Moving Objects in Airborne SAR

Remote Sensing Laboratories
Department of Geography
University of Zurich, 2022

Front page: SAR image of the Lake Constance with a defocused signature of a large-sized vessel (top), refocused two-dimensional image and three-dimensional reconstruction of the aforementioned vessel (bottom left and right, respectively).

Casalini, Emiliano

Imaging of Moving Objects in Airborne SAR

Remote Sensing Series, Vol. 86
Remote Sensing Laboratories, Department of Geography, University of Zurich
Switzerland, 2022

ISBN: 978-3-906894-21-8

This work was approved as a PhD thesis by the Faculty of Science of the University of Zurich in the fall semester 2021. Doctorate committee: Prof. Dr. Alexander Damm-Reiser (chair), Dr. Daniel Henke (dissertation supervisor), Prof. Dr. Michael Schaepman, Prof. Dr. Ross Stuart Purves, and Prof. Dr. Pierfrancesco Lombardo.

Imaging of Moving Objects in Airborne SAR

Dissertation

zur

Erlangung der naturwissenschaftlichen Doktorwürde
(Dr. sc. nat.)

vorgelegt der

Mathematisch-naturwissenschaftlichen Fakultät

der

Universität Zürich

von

Emiliano Casalini

aus

Italien

Promotionskommission

Prof. Dr. Alexander Damm-Reiser (Vorsitz)

Dr. Daniel Henke (Leitung der Dissertation)

Prof. Dr. Michael Schaepman

Prof. Dr. Ross Stuart Purves

Prof. Dr. Pierfrancesco Lombardo

Zürich, 2021

Abstract

Remote sensing is one of the most effective and promising methods to observe the Earth's surface and its processes. Its unique features make it possible to acquire information-rich images of large areas at various spatial, temporal and spectral resolutions. Among remote sensing techniques, RADAR (RAdio Detection and Ranging) techniques, such as Synthetic Aperture RADAR (SAR), are particularly attractive as they allow to obtain an electromagnetic image from an area or object of interest regardless of weather and light conditions. The spectrum of applications is large and various, ranging from environmental and social studies to safety and security management.

The interpretation of a SAR image, unfortunately, is very challenging as it presents features that are not commonly seen in optical images. This is especially true for moving objects, whose signature is oftentimes blurred and displaced from the real position, hence making it impossible to retrieve further information (e.g., back-scattering properties, dimensions, and shape). The need for automatic procedures to produce well-focused images of a moving object is, without a doubt, crucial to many applications, including human activity monitoring, search-and-rescue and urban planning. Though plenty of work has been done in this field, the recent technological advances in electronics and the development of more flexible acquisition platforms have widened the range of RADAR applications but, at the same time, have also introduced new challenges yet to be thoroughly addressed.

This dissertation concentrates on the derivation of two- and three-dimensional imaging algorithms for refocusing moving objects in SAR imagery. Several experiments, involving different types of sensors and objects, were conducted to test the adequacy of the proposed algorithms. The obtained results demonstrate that, provided the motion parameters of the moving object are accurately estimated, it is possible to design an imaging algorithm capable of strongly reducing the defocusing effects. From an unshaped blob of pixels, the moving object signature is transformed into a well-focused image with much more precise details. Hence, the motion parameters and dimensions of a moving object, whether on land or at sea, could be estimated with a percent error not larger than 5 % and 7 %, respectively. Moreover, in the case of large vessels, the results were so precise that, with visual inspection of the final point clouds, various parts of the object could be correctly identified. A thorough discussion of the main findings emphasizes both advantages (e.g., the ability to deal with different kinds of objects, and to work under different conditions) and limitations (e.g., the assumption that different points on the same object present the same

relative motion) of the proposed algorithms, and suggests potential future research directions.

Zusammenfassung

Die Fernerkundung ist eine der erfolgreichsten und vielversprechendsten Methoden zur Beobachtung der Erdoberfläche und deren Prozesse. Dank ihrer einzigartigen Eigenschaften können informationsreiche Bilder von grossen Gebieten in verschiedenen räumlichen, zeitlichen und spektralen Auflösungen erfasst werden. Unter den Fernerkundungstechniken sind RADAR-Techniken (RAdio Detection and Ranging) wie Synthetic Aperture RADAR (SAR) besonders attraktiv, da sie es ermöglichen, unabhängig von den Wetter- und Lichtverhältnissen ein elektromagnetisches Bild von einem Gebiet oder einem Objekt von Interesse zu erhalten. Das Spektrum der Anwendungen ist vielfältig und reicht von Umwelt- und Sozialstudien bis hin zum Sicherheitsmanagement.

Die Interpretation eines SAR-Bildes gestaltet sich, aufgrund von Merkmalen, die in optischen Bildern nicht anzutreffen sind, als äusserst anspruchsvoll. Dies gilt insbesondere für sich bewegende Objekte, deren Signatur oft unscharf und von der realen Position abweichend dargestellt wird. Dies verunmöglicht die Ermittlung weiterer Informationen (z. B. Eigenschaften der Rückstreuung, Abmessungen und Form). Die Bereitstellung an automatisierten Verfahren zur Erzeugung gut fokussierter Bilder eines sich bewegenden Objekts ist zweifellos von entscheidender Bedeutung für viele Anwendungen, einschliesslich der Überwachung menschlicher Aktivitäten, der Seenotrettung sowie der Stadtplanung. Die jüngsten technologischen Fortschritte in der Elektronik und die Entwicklung flexiblerer Aufnahmeplattformen haben das Spektrum der RADAR-Anwendungen erweitert, gleichzeitig aber auch neue Herausforderungen mit sich gebracht, welche es noch zu bewältigen gilt.

Diese Dissertation konzentriert sich auf die Entwicklung von zwei- und dreidimensionalen Bildgebungsalgorithmen zur Refokussierung bewegter Objekte in SAR-Bildern. Um die Eignung der vorgeschlagenen Algorithmen zu testen, wurden mehrere Experimente mit verschiedenen Sensortypen und Objekten durchgeführt. Die erzielten Ergebnisse zeigen, dass es möglich ist, einen Bildgebungsalgorithmus zu entwickeln, der die Defokussierungseffekte stark reduziert, vorausgesetzt, die Bewegungsparameter des sich bewegenden Objekts werden genau geschätzt. Die Signatur eines sich bewegenden Objektes, ursprünglich als eine unförmige Ansammlung von Pixeln erkennbar, wird in ein gut fokussiertes Bild mit viel präziseren Details überführt. Die Bewegungsparameter und die Abmessungen eines sich bewegenden Objekts, entweder an Land oder auf See, können mit einem prozentualen Fehler von höchstens 5 % bzw. 7 % erfasst werden. Bei grossen Schiffen waren die Ergebnisse sogar so genau, dass bei der visuellen Inspektion der endgültigen Punktwolken verschiedene Teile des Objekts

korrekt identifiziert werden konnten. In einer ausführlichen Diskussion der wichtigsten Ergebnisse werden sowohl die Vorteile (z. B. die Fähigkeit, mit verschiedenen Objektarten sowie unter verschiedenen Bedingungen zu funktionieren) als auch die Grenzen (z. B. die Annahme, dass verschiedene Punkte desselben Objekts dieselbe relative Bewegung aufweisen) der vorgeschlagenen Algorithmen hervorgehoben und mögliche zukünftige Forschungsrichtungen aufgezeigt.

Contents

Abstract **i**

Zusammenfassung **iii**

1 Introduction **1**
1.1 Remote Sensing for Human Activity Monitoring 1
1.2 Introduction to Synthetic Aperture RADAR 3
1.3 SAR Limitations for Moving Object Imaging 4
1.4 Detection and Imaging of Moving Objects with SAR 6
1.4.1 Detection Techniques 6
1.4.2 Two-Dimensional Imaging 6
1.4.3 Three-Dimensional Imaging 8
1.5 Objective and Research Questions 8
1.6 Structure of the Dissertation 10

2 Refocusing FMCW SAR Moving Target Data in the Wavenumber Domain **11**
2.1 Abstract 12
2.2 Introduction 12
2.3 Method 14
2.3.1 Sensor and Experiment Set-Up 14
2.3.1.1 Experiment #1 15
2.3.1.2 Experiment #2 15
2.3.2 Overview 16
2.3.3 Signal Model 17
2.3.4 Moving Target Focusing 20
2.3.5 Moving Target Refocusing 22
2.3.6 Validation Methods 24
2.4 Results 25
2.4.1 Simulation Results 25
2.4.1.1 Experiment #1 25
2.4.1.2 Experiment #2 27
2.4.2 Experimental Results 27
2.4.2.1 Experiment #1 27
2.4.2.2 Experiment #2 29
2.5 Discussion 32

2.5.1 General Comments . . . 32
2.5.2 Refocusing Algorithm . . . 32
2.5.3 Summary and Outlook . . . 34
2.6 Appendix . . . 35

3 Moving Target Refocusing With the FMCW SAR System MIRANDA-35 37
3.1 Abstract . . . 38
3.2 Introduction . . . 38
3.3 Method . . . 40
3.3.1 Sensor and Experimental Set-up . . . 40
3.3.1.1 Experiment #1 . . . 41
3.3.1.2 Experiment #2 . . . 41
3.3.2 Processing Chain . . . 41
3.3.2.1 GMTI and Data Cropping . . . 42
3.3.2.2 Image Inversion Mapping . . . 42
3.3.2.3 Automatic Time Window Selection . . . 44
3.3.2.4 Motion Compensation . . . 44
3.3.2.5 Range Doppler Imaging . . . 45
3.3.2.6 Doppler to Cross-range Scaling . . . 46
3.3.2.7 CLEAN . . . 46
3.3.3 Validation Methods . . . 46
3.4 Results . . . 47
3.4.1 Experiment #1 . . . 47
3.4.2 Experiment #2 . . . 49
3.5 Discussion . . . 50
3.5.1 Refocusing Algorithm . . . 50
3.5.2 Summary and Outlook . . . 52

4 Multi-View Three-Dimensional Radar Imaging of Moving Targets with Time-Domain Processing 55
4.1 Abstract . . . 56
4.2 Introduction . . . 56
4.3 Method . . . 58
4.3.1 Sensor and Experimental Set-up . . . 58
4.3.2 GBP Algorithm . . . 59
4.3.3 Moving Target Imaging . . . 60
4.3.3.1 Overview of the Processing Chain . . . 60
4.3.3.2 Motion Parameters Estimation . . . 60
4.3.3.3 Modified GBP Algorithm . . . 61
4.3.3.4 3-D Reconstruction . . . 62
4.3.4 Validation Methods . . . 64
4.4 Results . . . 64

4.5 Discussion 66
4.5.1 Algorithm Performances 66
4.5.2 CSAR 72
4.5.3 General Comments 73
4.5.4 Summary and Outlook 73

5 Synopsis **75**
5.1 Main Results 75
5.2 Conclusions 79
5.3 Outlook 80
5.3.1 Pixel-Dependent Refocusing 80
5.3.2 Terahertz RADAR Imaging 82
5.3.3 Further Applications 82

Acknowledgements **93**

List of Abbreviations

ATI	Along-Track Interferometry
CFAR	Constant False Alarm Rate
CSA	Chirp Scaling Algorithm
CSAR	Circular SAR
DPCA	Displaced-Phase-Center Antenna
DSM	Digital Surface Model
DTM	Digital Terrain Model
FMCW	Frequency-modulated Continuous-wave
FSA	Frequency Scaling Algorithm
FT	Fourier Transform
GBP	Global Backprojection
GMTI	Ground Moving Target Indication
GPS	Global Positioning System
IFT	Inverse Fourier Transform
InISAR	Interferometric ISAR
IRW	Impulse Response Width
ISAR	Inverse SAR
ISLR	Integrated Side-lobe Ratio
LIDAR	LIght Detection and Ranging
LPFT	Local Polynomial Fourier Transform
LSE	Least Square Error
MLE	Maximum Likelihood Estimator
MoComp	Motion Compensation
MT	Moving Target
NRS	Normalized Relative Speed
PDF	Probability Density Function
PoSP	Principle of Stationary Phase
PRF	Pulse Repetition Frequency
PRI	Pulse Repetition Interval
PSF	Point Spread Function
PSLR	Peak to Side-lobe Ratio
PTRS	Point Target Reference Spectrum
RADAR	RAdio Detection and Ranging
RCM	Range Cell Migration
RCS	Radar Cross-section
RFM	Reference Function Multiplication
RS	Remote Sensing
RVP	Residual Video Phase
SAR	Synthetic Aperture RADAR
SNCR	Signal-to-Noise-and-Clutter Ratio

SNR	Signal-to-Noise Ratio
STAP	Space-Time Adaptive Processing
UAV	Unmanned Aerial Vehicle
WDA	Wavenumber Domain Algorithm
2-D	Two-dimensional
3-D	Three-dimensional
2D-FT	Two-dimensional Fourier Transform
2D-IFT	Two-dimensional Inverse Fourier Transform

Chapter 1

Introduction

1.1 Remote Sensing for Human Activity Monitoring

Remote Sensing (RS) has been defined in a variety of ways, but, at its essence, it is the science of obtaining information about an object or phenomenon through the analyses of data acquired by a sensor that is not in direct contact with the target of investigation [1]. This definition, though adequate, is very broad and includes numerous applications (e.g., archaeology, architecture, medicine, and robotics) that are not discussed herein. For the scope of this dissertation, a more suitable definition can be formulated as follows: RS is the science of obtaining information about the Earth's surface, using images acquired by airborne or spaceborne sensors, and using electromagnetic radiation reflected or emitted from the Earth's surface [2].

RS is performed with either a passive or an active sensor [1, 2]. Passive sensors do not emit electromagnetic waves, and they exploit the radiation either reflected or emitted from the Earth's surface. To this class belongs, for instance, an imaging spectrometer, an optical system capable of acquiring coregistered images in many spectrally contiguous bands [3, 4]. Active sensors, on the other hand, are equipped with their own source of radiation and, in turn, they are not dependent on the light conditions of the area under analysis. They can be subdivided into two main groups: LIght Detection and Ranging (LIDAR) [5, 6] and RAdio Detection and Ranging (RADAR) [7, 8]. The latter usually operates at longer wavelengths, which are less sensitive to smaller objects (e.g., atmospheric particles, droplets, and water particles). Hence, not only is RADAR better suitable for long range applications, but it is also not affected by weather conditions, thus making it especially attractive for RS applications.

The primary advantage of RS is the ability to provide regional- to global-scale products with fine spatial, temporal and spectral resolution. This, along with the fact that both sensors and acquisition platforms have recently become more accessible, has made RS a powerful tool for a vast number of applications. These range from environmental applications (e.g., observation of land [9, 10], bodies of water [11, 12], and snow and ice [13–15]) to social sciences (e.g., deriving population distribution data-sets [16, 17], and detecting urban deprived areas [18, 19]).

Of particular importance is RS of human activities on land and at sea, which is crucial for many fields, including urban planning, safety and security management,

search-and-rescue, etc. For instance, traffic flows are important for building historic data-sets for traffic prediction, or deriving insights for future infrastructure developments. Reliable, detailed and continuous traffic data at regional-to-global scale can be obtained either with optical or RADAR techniques, as demonstrated in [20] and [21, 22], respectively. In the latter, the authors present two different processing methods for wide area traffic monitoring using an airborne and a spaceborne RADAR sensor, respectively. The proposed methods can successfully detect moving objects, estimate their position, velocity and direction of motion. Nonetheless, these methods cannot differentiate between small-, mid- and large-sized moving objects, and cannot discriminate between objects with similar dimensions but different shapes.

Furthermore, RS is widely used to detect and monitor illegal human activities (e.g., illegal fishing, logging, mining, and waste discharge), which have potentially deleterious effects on environments and ecosystems. Particularly common are waste discharge events at sea, which can result in a serious damage to the marine environment. Oftentimes, these events are not a consequence of an accident, but a result of illegal activities, including deliberately discharging engine room wastes. The vessels responsible for such activities either manipulate or switch off the on-board vessel monitoring system, hence making it impossible for law enforcements to identify them. To this end, RADARs are nowadays used not only to detect the presence of suspicious vessels [23], but also to monitor the consequences of their activities such as, for instance, in the case of oil spills [24, 25]. Though these algorithms have been proven to be a useful tool for waste discharge events at sea, they are not designed to identify the responsible vessels.

RS techniques can also be used to help design effective maritime search-and-rescue operations. With the rapid growth of maritime trade and transportation, and the recent development of migration phenomena by sea, rapid detection and effective monitoring of vessels in distress has become a major concern. A thorough overview of vessel detection with RADAR and optical imagery can be found in [26] and [27], respectively. Both technologies can provide timely and accurate geospatial information of distressed vessels, which is crucial for supporting humanitarian actions, as presented in [28–31]. The migrant crisis at Europe's southern borders has increased migration outflows from north Africa to Europe. Many migrants are forced to cross the Mediterranean sea with unreliable boats, or even with small rubber inflatables, which are in no way suitable to travel such long distances. In [30, 31], the authors demonstrate that spaceborne RADAR sensors can successfully detect a rubber boat lying almost stationary on a lake bed. However, in a realistic scenario where the boat is in motion, the proposed algorithms cannot accurately estimate, among many parameters, its dimensions. Since the latter give a rough idea of the maximum number of migrants on-board, the usefulness of these algorithms for search-and-rescue missions is somewhat limited.

In conclusion, RS techniques are essential tools for monitoring human activities on Earth. Designing algorithms that consider the spatio-temporal dynamics of such

FIGURE 1.1: SAR image of the German A 48 highway acquired by the MIRANDA-35 sensor on the 20th of June 2016.

activities is the key for better understanding geographic phenomena (e.g., environmental disasters, human migrations, pollution, traffic flows, and urban growth). Though most of the RS systems are not yet capable of detecting a person from an image, they can, however, detect man-made objects, such as vehicles (e.g., boats, cars, ships, trains, and trucks). Hence, the main objective of this dissertation is to study the impact of the motion of man-made objects on RADAR products, and to assess what information can be retrieved from the objects themselves.

1.2 Introduction to Synthetic Aperture RADAR

Most of RADAR systems are designed to carry out a specific set of primary tasks (e.g., detection, ranging, and Doppler frequency estimation) [7]. Although this operating mode is more than adequate for many applications (e.g., airport surveillance, detection of meteorological phenomena, and speed measurement), it is intrinsically unable to provide two-dimensional products, such as an electromagnetic image of the Earth's surface, therefore making it unfit for Earth observation missions.

Synthetic Aperture RADAR (SAR) is a frequently exploited technique for Earth's surface monitoring in all-light and all-weather conditions [32, 33]. In SAR, the sensor is mounted on-board a moving platform (e.g., aircraft, drone, and satellite), and its forward motion *synthesizes* a long antenna. The received signal is processed by means of any of the available SAR focusing techniques [32, 33], thus resulting in an electromagnetic image with high resolution both in range and azimuth. The high accuracy of SAR products, along with a resolution in the order of cm, has led to a vast set of applications, including ice monitoring [34], oceanography [35], topographic mapping [36] and wide area surveillance [37]. To further appreciate the importance of SAR, it should be reminded that, unlike optical and LIDAR systems, it can operate

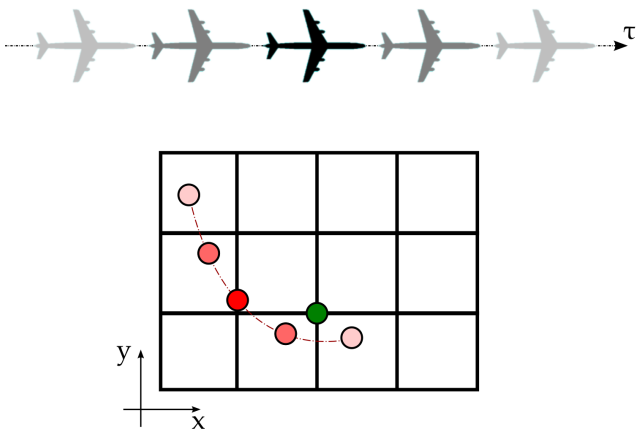

FIGURE 1.2: Simplified sketch of a stripmap SAR acquisition [38]: point-like stationary object (green circle), point-like moving object (red circles) and corresponding trajectory (red dashed line).

successfully with unfavourable weather conditions, which are common, for instance, in the tropics and the Arctic.

An exemplary SAR image is depicted in Fig. 1.1. This image was chosen in light of the fact that it contains many features that are unique to SAR images, thus helping the reader to grasp both limits and possibilities of this technology. The image comprises many different objects, both natural and man-made: fields, trees, buildings, a road sign, a short stretch of an highway and, lastly, a moving vehicle. Even those who have never seen a SAR image beforehand will be able to retrieve most of the information content from Fig. 1.1, as it is quite similar to the corresponding optical image. This is especially true for stationary objects, which appear to be very well-focused. Moving objects, on the other hand, regardless of whether they are artificial or natural, appear blurred in the image. More specifically, for the exemplary image in Fig. 1.1, all tree crowns are defocused, a clear indicator that the data were acquired with windy conditions. As for the moving vehicle, not only is its signature defocused, but it is also displaced from the road on which it is travelling. These effects, namely, blurring and displacement, are very well-known in the SAR community, and they always affect the signature of a moving object [39, 40].

1.3 SAR Limitations for Moving Object Imaging

The first question that needs to be addressed is "when is an object in motion?" In the SAR community, an object is in motion when it moves with respect to a reference point, which is a stationary point located on ground. Icebergs, as well as glaciers, landslides, flock of birds, or tree crowns and transportation vehicles, are only few examples of moving objects in SAR imagery.

Fig. 1.2 depicts the conventional stripmap acquisition mode, comprising two point-like objects, one with own motion and one without (i.e., the reference point). As SAR technology deploys a moving platform, both objects are in motion with respect to

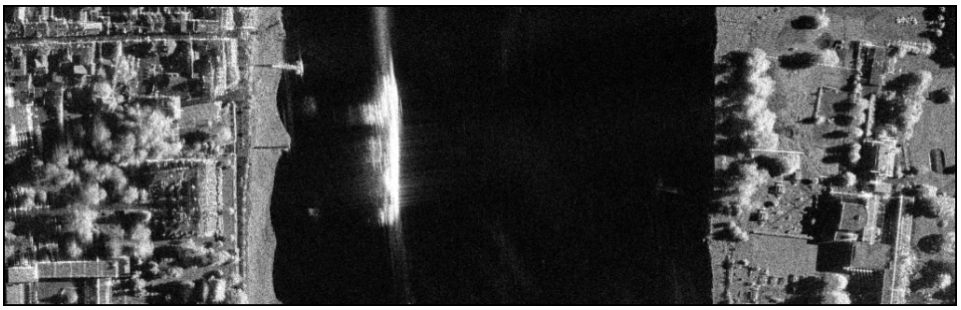

FIGURE 1.3: SAR image of the Rhine river acquired by the MIRANDA-35 sensor on the 11th of September 2018.

the antenna phase center, the point from which the electromagnetic radiation spreads outwards. Hence, both range histories, the distances between phase center and objects, vary substantially within the observation time. Unfortunately, SAR processors can only compensate for the range history of the reference point. As a consequence, after the image formation process, the moving object signal is characterized by a residual range history, which causes the aforementioned effects. More specifically, the along- and cross-track component (see x- and y-axis in Fig. 1.2, respectively) of the residual range history are responsible for the blurring and displacement, respectively [39, 40].

To fully understand how likely these effects are when observing dynamic processes with SAR, it is necessary to relate the motion to both the illumination time and the operating wavelength. The illumination time is defined as the time span during which a given scatterer on ground is illuminated by the antenna. Its value varies greatly depending on a variety of factors (e.g., acquisition geometry, antenna pattern, and platform altitude), reaching up to several seconds for airborne scenarios. In this time, an excursion (i.e., the difference between maximum and minimum value) of the residual range history in the order of the wavelength, or even smaller, would prevent the received signal from being coherently integrated, and thus optimally focused. For spaceborne applications, common values of the operating wavelength range from 3 m to 3 cm, while for short-range airborne applications they reach as low as 3 mm.

Most of dynamic processes change so slowly that the focusing quality of the final image is not affected, even when using long illumination times and short wavelengths. The glacier *Jakobshavn Isbrae*, in Greenland, is generally considered to be the fastest glacier in the world, with speeds up to 40 m per day, which translates into less than half a millimeter per second. Buildings, on the other hand, under normal conditions, experience vertical motions with rates up to tens of mm per year. Hence, the SAR image of a moving glacier, or of a building undergoing a deformation process, will very likely exhibit a high degree of focusing. Man-made moving objects (e.g., trains, vehicles, and satellites), on the contrary, usually move much faster. The SAR image of a short stretch of the Rhine river is shown in Fig. 1.3. The shores of the rivers, crowded with buildings and trees, are clearly visible on the left- and right-hand side of the image. In the middle of the river, whose pixels are characterized by low amplitude and thus darker grays, one can identify a bright signature produced by a moving vessel.

As SAR processing failed at compensating for its range history, the resulting product exhibits blurring effects, therefore making it more challenging, or even impossible, to retrieve meaningful information, including geometry and electromagnetic properties, and to successfully recognize the object. This prompts the need for the development of imaging algorithms that are primarily designed to remove the undesired effects characterizing the signature of a moving object in SAR imagery.

1.4 Detection and Imaging of Moving Objects with SAR

1.4.1 Detection Techniques

The detection of moving objects in SAR imagery is the prerequisite for refocusing and recognition. This processing step depends on many factors, including the number of available receiving channels and their arrangement, the radar parameters as well as the specific ground scenario. The detection of a moving object with low radial velocity is usually more challenging as the signal spectrum is overlaid with that of the ground clutter, the signal back-scattered by the static scene, which is usually characterized by a much higher power. State-of-the-art techniques for detecting moving objects buried in clutter relies on using multiple receiving channels, such as in the case of Along-Track Interferometry (ATI) [41], Displaced-Phase-Center Antenna (DPCA) [42] and Space-Time Adaptive Processing (STAP) [43].

Moving objects with high radial velocity are more easily detectable as the Doppler frequency shifts the signal spectrum outside of the main beam clutter. In absence of aliasing effects (i.e., when the spectrum is *folded* around the Nyquist frequency), the object signature is not overlaid with that of the static scene and the detection can be performed by means of simple amplitude-based techniques [44].

Lastly, it is worth highlighting that the clutter characteristics play a key role in designing the detection scheme. The signature of a land vehicle (e.g., cars, trains, and trucks) is most likely to compete with ground-clutter produced by the neighbouring stationary objects (e.g., building, fields, and streets). Vice-versa, for a maritime vehicle, the signature is almost certainly imaged on the very same body of water through which it travels. The water conditions, as well as the operating wavelengths, determine whether there is need for a clutter removal technique [26].

1.4.2 Two-Dimensional Imaging

There exists a vast amount of literature on refocusing moving objects in SAR imagery. The design of an imaging algorithm depends on many different factors, the most important ones being processing domain, RADAR technology, system specifications, desired application, *a-priori* knowledge, etc.

A commonly adopted approach consists in modifying well-known focusing algorithms to *match* the signal back-scattered from the moving object. In this regard,

in [45, 46], the authors have successfully exploited the Wavenumber Domain Algorithm (WDA) and the Chirp Scaling Algorithm (CSA) to perform moving object imaging. Alternatively, an optimal matching scheme can be derived from the signal spectrum of the moving object. In this context, the keystone transform was proven to be an appropriate and effective method to compensate for the range cell migration, as illustrated in [40, 47, 48], which is the main responsible for signature blurring. In [49], the authors identify the moving object response in the SAR image domain, use it to derive the signal spectrum and, lastly, to design the imaging scheme.

What all these works have in common is that they are based upon assumptions that are unlikely to hold in realistic scenarios. Not only they assume the sensor to fly with a perfectly linear trajectory and at a constant velocity, but they also use simplistic models of range history. When dealing with more complicated scenarios, the aforementioned algorithms are sub-optimal and likely to fail, hence prompting the need for a more sophisticated solution. Inverse SAR (ISAR) is a state-of-the-art imaging algorithm capable of handling a wider range of motions [50–52]. Oftentimes, ISAR processing is combined with autofocus, the latter referring to any technique designed to estimate the range history of a moving object from its back-scattered signal. In [53], an ISAR autofocus algorithm is presented: the range history is modelled as a finite-order polynomial, and its coefficients are iteratively estimated on the basis of the image contrast. Though ISAR processing was originally designed for ground-based systems, similar techniques have been developed to handle SAR data-sets, acquired with a moving platform. To do so, the signature of the moving object is firstly detected, back-projected onto the received data domain and, lastly, ISAR processed [54, 55].

When designing an imaging algorithm, the characteristics of the transmitted waveform have to be taken into consideration. Until few years ago, most of SAR sensors made use of pulsed-technology, while only recently it has become more common to use Frequency-modulated Continuous-wave (FMCW) technology [7]. The main difference is given by the nature of the transmitted signal: unlike pulsed-SAR, which transmits a sequence of extremely short pulses, FMCW-SAR transmits almost continuously. As a consequence, FMCW-SAR needs little power to operate, hence defining a more compact and cost-effective system capable of obtaining performances as good as those of pulsed-SAR. Though FMCW-technology is well renowned, only few researches have dealt with the imaging of moving objects in FMCW-SAR imagery. All aforementioned methods, which are not designed to handle the peculiarities of FMCW signals, cannot precisely image moving objects. In [56, 57], the authors present a FMCW-ISAR signal model, analyze the FMCW-induced image distortions and develop an autofocus algorithm. However, this algorithm was applied only to X-band data-sets with meter scale range resolution, and hence it is not clear whether a similar method could successfully handle data-sets acquired at higher frequencies and with larger bandwidths.

1.4.3 Three-Dimensional Imaging

Two-dimensional products are not suitable for properly representing three-dimensional objects, whether stationary or moving, especially when the geometry is complex. In both SAR and ISAR, the third dimension is projected onto the imaging plane, thus making the interpretation of the image more difficult. However, the three-dimensional geometry of the moving object can be reconstructed with different techniques. One way to subdivide them is to consider the number of receiving channels. Most of single-channel techniques exploit concepts that were originally designed for photogrammetric applications. Given a sequence of RADAR images, the three-dimensional geometry of an object of interest can be derived, provided that the relative motion with respect to the sensor is known [58]. As demonstrated in [59,60], the factorization method, which is quite popular in the computer vision domain [61], can effectively reconstruct the third dimension from a sequence of ISAR images. Nevertheless, this approach relies on the correct association of the same scatterer through the different frames. This is not at all trivial as the back-scattering properties of an object might change drastically within fractions of second, hence making the factorization method unpractical.

Multi-channel state-of-the-art solutions combines ISAR processing with interferometry, introducing the concept of Interferometric ISAR (InISAR). The receiving antennae are usually arranged in two orthogonal baselines, defining an L-shaped configuration, which is particularly suitable for reconstructing moving objects [62]. An ISAR-based algorithm specifically designed for imaging large vessels is presented in [63]. In [64], the authors give a thorough description of three-dimensional InISAR theory, with a particular emphasis on the analysis of the imaging plane. The reconstruction of moving objects or, in general, RADAR imaging, crucially benefits from observing the object from different aspect angles. In fact, when relying on a single image, it is common to experience shadowing effects produced when parts of the object block the electromagnetic signal, therefore making it impossible to illuminate the whole surface. To avoid this, multiple sensors or, alternatively, longer observation times, prevent shadowing effects from corrupting the final products [65]. The imaging algorithm in [64] is the state-of-the-art for reconstructing the three-dimensional geometry of a moving object. However, its performances are strictly dependent on how accurately the imaging plane is estimated. Even a small error can greatly affect the geolocation accuracy of a given scatterer, thus producing three-dimensional products with unrealistic dimensions that are of no use to most applications. For instance, in the case of search-and-rescue missions, under- or overestimating the dimensions of a vessel in distress can result in an inappropriate response plan, with potentially disastrous consequences in terms of loss of life.

1.5 Objective and Research Questions

This thesis aims to solve methodological issues related to the imaging of moving objects in SAR imagery, in order to expand application fields of SAR RS. A particular

problem is that SAR is designed to image the static scene, and thus cannot handle moving objects. Hence, this thesis focuses on designing imaging algorithms, with the primary objective of producing well-focused electromagnetic images of moving objects from SAR data-sets. Particular attention is paid to tailoring the imaging algorithm to the RADAR technology, the system specifications as well as the acquisition geometry.

Moving Object Refocusing in FMCW-SAR Imagery

Due to recent developments in hardware technology, FMCW-SAR has become a frequently exploited solution for imaging the Earth's surface from an airborne platform. FMCW-technology allows to design low-cost, low-powered and compact systems, while maintaining performances comparable to pulsed-SAR. While interest in this technology has steadily increased, there is still a vast, unexploited potential that needs to be identified and assessed. To this end, when designing any imaging algorithm, it should be taken into consideration that FMCW waveforms differ from pulsed-SAR signals and, in turn, the signature of a moving object will preserve this characteristics.

The research question for this Chapter is formulated as follows: "How far is it possible to refocus a moving object using an algorithm based on the focusing technique that produced the input FMCW-SAR image?"

Moving Object Refocusing with a Light-Weight Platform

The need for lighter platforms has led to the use of light-weight aircrafts and, more recently, small-sized Unmanned Aerial Vehicles (UAVs) for airborne SAR applications. Because of the limited payload capacity, they are usually equipped with a very compact sensor, operating at higher carrier frequencies. Unlike heavier aircrafts or satellites, these solutions are more flexible, cost-effective and can handle non-linear acquisition geometries. On the other hand, the light weight makes them particularly susceptible to wind disturbances, which negatively impacts on the quality of the SAR products. The light-weight factor and its implications, in combination with the high operating frequency, increase the difficulty of the refocusing task, and cast doubts on the effectiveness of light-weight platforms for moving object imaging.

The research question for this Chapter is formulated as follows: "How good can state-of-the-art ISAR-based techniques perform when resources are poor and physical design constraints are present, such as in the case of light-weight systems?"

Three-Dimensional Imaging with a Circular Acquisition

Both two- and three-dimensional stripmap SAR products are usually characterized, among many other features, by shadowing effects, and therefore parts of the object are not visible. Non-linear acquisition geometries such as, for instance, a circular flight-path, are better suitable for imaging purposes as they allow to observe a moving object from different viewing angles. The information retrieved from different images can be merged, thus producing a more reliable final product.

The research question for this Chapter is formulated as follows: “To what extent are three-dimensional imaging techniques capable of retrieving geometrical features of a moving object from circular SAR data?”

1.6 Structure of the Dissertation

Chapter 1 defines the framing of this thesis by outlining the context, reviewing the state-of-the-art, and identifying research gaps. Particular attention is paid to SAR technology, whose contribution to RS is emphasized by giving an overview of the most prominent peer-reviewed contributions. The problem of moving objects in SAR imagery is highlighted with exemplary images, the reasons behind it are briefly explained and, lastly, a thorough overview over the imaging of moving objects is given. Finally, the research questions this study sought to answer are presented.

Chapter 2 is based on a first-authored, peer-reviewed journal article [66], published in IEEE Transactions on Geoscience and Remote Sensing. It demonstrates how the well-known WDA can be adjusted to refocus moving objects in FMCW-SAR imagery. The publication is self-contained in terms of structure and content.

Chapter 3 is based on a first-authored, peer-reviewed journal article [67], published in IEEE Journal of Selected Topics in Applied Earth Observations and Remote Sensing. It evaluates the imaging capabilities of a light-weight FMCW-SAR system when using state-of-the-art ISAR-based techniques. The publication is self-contained in terms of structure and content.

Chapter 4 is based on a first-authored, peer-reviewed journal article [38], submitted in IEEE Transactions on Geoscience and Remote Sensing. It presents how to refocus moving objects with a time-domain processor, and it demonstrates the potential of using a circular acquisition geometry for imaging purposes. The publication is self-contained in terms of structure and content.

Chapter 5 answers the individual research questions, summarizes the main findings from the publications of Chapters 2–4, and provides concluding remarks. Finally, an outlook of potential future research directions is given.

Chapter 2

Refocusing FMCW SAR Moving Target Data in the Wavenumber Domain

Emiliano Casalini, Max Frioud, David Small and Daniel Henke

This chapter is based on the peer-reviewed article: IEEE Transactions on Geoscience and Remote Sensing, vol. 57, no. 6, pp. 3436–3449, 2019; DOI: 10.1109/TGRS.2018.2884830. It is reprinted as the final submitted manuscript and has been modified to fit the layout of this thesis.

E. Casalini and D. Henke conceptualized the study. E. Casalini elaborated the methodology, performed the analysis and interpreted the results. M. Frioud and D. Henke contributed to the analysis and the interpretation of the results. E. Casalini wrote the first draft of the manuscript. E. Casalini, D. Small and D. Henke participated in the writing and editing of the final manuscript.

2.1 Abstract

FMCW SAR are now commonly adopted solutions for producing high resolution electromagnetic images of the earth surface. However, many SAR applications, such as detection or imaging of moving targets, have not yet been thoroughly researched for FMCW scenarios. This paper presents a refocusing technique that works in the wavenumber domain and is based on the reference spectrum of a point-like moving target. The method is illustrated using simulated experiments, and is further tested by processing real data collected by the Ka-band MIRANDA-35 sensor. The obtained results are validated and compared with independent ground measurements, thus demonstrating the accuracy of the presented method.

2.2 Introduction

The compactness, cost effectiveness and very high spatial resolutions have made FMCW SAR a frequently exploited solution for imaging the earth surface. The main difference between common pulsed SAR and FMCW SAR lies in the different nature of the transmitted signal. Pulsed SAR transmits short pulses [32], whereas FMCW SAR transmits relatively long sweeps [68]. In general, transmission times are such that the stop-and-go approximation is not valid. However, in the FMCW SAR scenario, the variation of the instantaneous slant-range during transmission considerably affects the raw data by introducing a range walk term [68] and an additional range-dependent range-azimuth coupling term [69]. These effects have to be dealt with when focusing both stationary and moving targets. In recent years, a number of algorithms that were originally designed for focusing pulsed SAR data have been modified in order to account for the aforementioned FMCW effects [69–72]. A state-of-the-art WDA was proposed in [69]: this algorithm not only deals with the range walk term, but also compensates for the range-dependent range-azimuth coupling term which was neglected by the previously proposed signal models [68]. Although FMCW SAR focusing has been well-researched, the detection and imaging of ground moving targets in FMCW SAR images has only rarely been addressed [57, 73–76]. A Ground Moving Target Indication (GMTI) solution was suggested in [73]: when using triangularly frequency-modulated signals, the separate processing of the two slopes produces distinct images where the moving target is registered to different positions. In [57], it was shown that moving target signatures can be refocused by means of ISAR in combination with an auto-focusing technique. The FMCW signal model, originally introduced for stationary targets [69], was modified in [74] for moving targets. Furthermore, conventional FMCW SAR

focusing algorithms can be adjusted to serve GMTI purposes: moving target detection and focusing can be obtained by modifying, respectively, the Frequency Scaling Algorithm (FSA) [75] and the WDA [76]. More specifically, the last two solutions exploit the concept of Normalized Relative Speed (NRS) which has proven to be a powerful tool for wide-band SAR environments [46, 77–79]. This parameter can be used to modify both time [77] and wavenumber domain-based focusing algorithms [78] to detect and focus moving targets. The latter approach has been successfully applied to TerraSAR-X and TanDEM-X images [79], thus demonstrating its feasibility of processing data collected by different types of SAR sensors.

In this paper, we concentrate on the design of a wavenumber domain-based algorithm for refocusing moving targets in SAR images originally produced by the WDA [69]. Existing approaches (see [44]) were exploited in order to perform moving target indication as that was not the main focus of this work. The proposed algorithm is designed on the basis of the theory of focusing moving targets before the formation of the complex image. Such a problem, which has been thoroughly discussed for the pulsed SAR case, has also been addressed for the FMCW SAR scenario [76]: however, the authors' dissertation is designed on a simplified signal model which does not take into account the platform's motion during transmission. By making use of a more realistic solution, we derive the spectrum of a point-like moving target after conventional SAR focusing, thus emphasizing the phase component responsible for defocusing. The signal is then remapped onto a new and more favourable domain and the aforementioned phase component is compensated for by applying a properly designed filter. Unlike ISAR-based algorithms, where the conversion from Doppler to azimuth is not straightforward and requires a mandatory scaling step [57], the refocused signature is obtained here by directly applying an Inverse Fourier Transform (IFT). In case the target's motion was not *a-priori* known, a set of tentative NRSs are tested, and the estimate is made based on the entropy values of the refocused images. In order to assess the capabilities of the proposed algorithm, both simulated and real data were processed, where the latter were collected by the MIRANDA-35 system developed by Fraunhofer FHR [80].

The remainder of the paper is organized as follows. In Section 2.3.1 we introduce the MIRANDA-35 sensor, its specifications and we describe the experiments' set-ups. Section 2.3.2 gives an overview of the proposed method and outlines those processing steps not discussed in detail in the rest of the paper. Section 2.3.3 introduces the signal model of a point-like moving target; the theoretical foundations for focusing moving targets before the formation of the complex image are given in Section 2.3.4, and the refocusing algorithm is presented in Section 2.3.5. Section 2.3.6 lists the available ground measurements used to validate the results. The obtained performances were assessed by

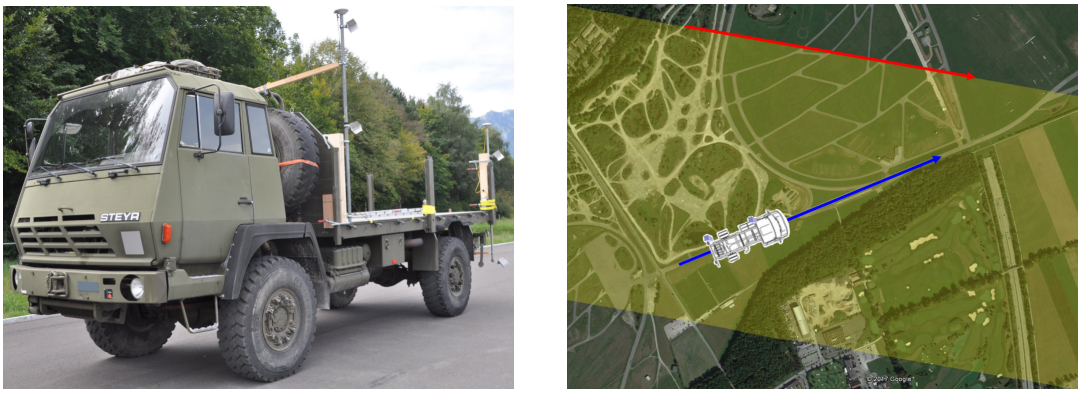

(a) (b)

FIGURE 2.1: (a) Target of interest: Steyr truck with four dihedral corner reflectors, (b) Google Earth image of the *Thun* test-site: (red) Sensor's flightpath, (blue) Target's path, (yellow) Swath

Parameter	Value
Carrier frequency	35 GHz
Bandwidth	1 GHz
PRF	1695.53 Hz
Azimuth beam-width	3 deg
Mid-swath slant-range	2003.32 m
Swath width	791.21 m
Sampling frequency	9.77 MHz

TABLE 2.1: System Parameters: Experiment #1

processing both simulated and real data, as shown in Sections 2.4.1 and 2.4.2. Finally, a detailed analysis of the results and potential research directions are given in Section 2.5.

2.3 Method

2.3.1 Sensor and Experiment Set-Up

The SAR sensor utilized in the experiments was the Fraunhofer FHR MIRANDA-35 system [80]. This is an airborne sensor transmitting FMCW signals at Ka-band and capable of achieving centimetre resolution. The system is comprised of one transmitting and up to four receiving antennas, allowing for a variety of acquisition modes. Two experiments, held during distinct campaigns, are discussed here in detail.

Parameter	Value
Carrier frequency	35 GHz
Bandwidth	0.3 GHz
PRF	6781.49 Hz
Azimuth beam-width	3.3 deg
Mid-swath slant-range	1171.07 m
Swath width	639.36 m
Sampling frequency	13.02 MHz

TABLE 2.2: System Parameters: Experiment #2

FIGURE 2.2: Google Earth image of the *Bassenheim* test-site: (red) Sensor's flightpath, (blue) Targets' path, (yellow) Swath

2.3.1.1 Experiment #1

The experiment was conducted in Summer 2017 in the surroundings of the town of *Thun*, in the canton of *Bern*, Switzerland. The main system parameters, which have also been used to generate the simulated data-set discussed in Section 2.4.1.1, are summarized in Table 2.1. The deployed platform (i.e., the *Diamond DA42 Centaur*) had a mean altitude of 1377 m above ground, an average speed of $49\,\mathrm{m\,s^{-1}}$ and a mean incidence angle of 55 deg. The target of interest, which is shown in Fig. 2.1a, was equipped with four dihedral corner reflectors and two Global Positioning System (GPS) antennas. These were attached on two poles at different heights (see Fig. 2.1a, right), and they were tilted according to the platform's heading, thus ensuring they would be properly illuminated during the acquisition time. The experimental set-up is depicted in Fig. 2.1b: the nominal platform's heading was 100 deg, whereas the target was driven at constant velocity with an approximate angle of 67.5 deg with respect to North. This, in turn, resulted in both an along- and a cross-track motion, making the target's signature smeared and displaced along the azimuth axis. The sensor was flown a number of times over the area of interest and different data-takes were collected: for each of them, the target's speed was modified to test the method under different conditions.

2.3.1.2 Experiment #2

The experiment was conducted in Summer 2016 in the municipality of *Bassenheim*, in the district *Mayen-Koblenz*, Germany. The sensor was mounted on the ultra-light-weight FHR Delphin platform to record the traffic flows of the A61 highway which presented a variety of moving targets. The main system parameters, which were used to generate the simulated data-set discussed in

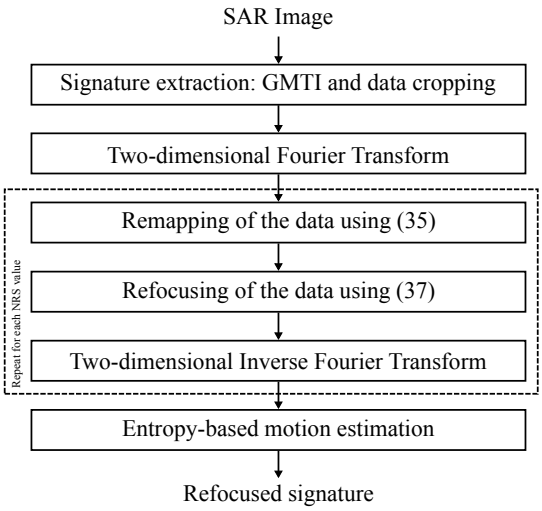

FIGURE 2.3: Block diagram of the refocusing algorithm

Section 2.4.1.2, are summarized in Table 2.2. The flightpath had a mean altitude of 745 m above ground, an average platform speed of $35\,\mathrm{m\,s^{-1}}$ and a mean incidence angle of 60 deg. The experimental set-up is depicted in Fig. 2.2: the nominal platform's heading was 140 deg, while the targets presented different orientations with respect to the flightpath. Similarly to Experiment #1, all moving targets presented a combination of along- and cross-track motion. However, due to the adopted geometry and the specific test-site, the resulting radial velocities were substantially higher, emphasizing the impact of the motion on the final signatures.

2.3.2 Overview

The block diagram of the proposed algorithm is sketched in Fig. 2.3. The first step consists of performing moving target indication: the choice of the detector depends on the specific data-set and does not fundamentally change the final product. For our experiments, due to the very favourable circumstances (see Section 2.5.1 for details), the targets of interest of both experiments were easily detectable by making use of an amplitude-based technique similar to the detection step in [44]. The derived pixels were then grouped together and de-noised using morphological filtering [81]. Subsequently, a border tracing algorithm was used to connect contiguous objects and obtain meaningful information such as the center of mass and size [82]. A rectangular crop, whose position and dimensions are defined on the basis of previously estimated geometric features, was selected to extract the useful signal. Consequently, a Two-dimensional Fourier Transform (2D-FT) was performed in order to map the cropped data from the spatial into the wavenumber domain. Moving target refocusing was then performed for each NRS: for a detailed discussion, please refer to Section 2.3.5.

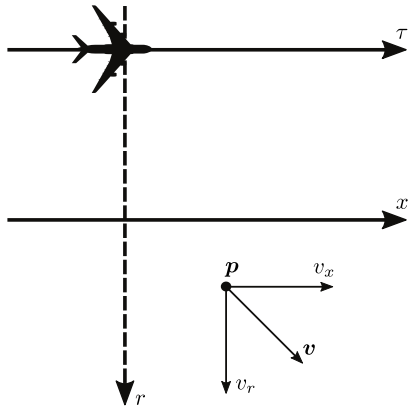

FIGURE 2.4: Geometry of the system

Lastly, the NRS yielding the image with the best degree of focusing was estimated on the basis of the obtained entropy values. The entropy is a measure of the smoothness of a distribution [83]: higher degrees of focusing result in sharper images and thus smaller entropy values. In light of the above, the entropy value was computed for the entire set of tentative NRSs, and then the estimate was consequently derived.

2.3.3 Signal Model

The mathematical symbols used throughout the entire paper are briefly listed below.

c	Speed of light
f_τ, f	Azimuth and range frequency
f_0	Transmitted signal carrier frequency
K_r	Transmitted signal chirp rate
k_x, k_r	Azimuth and range wavenumber
k_w	Slant-range wavenumber
r_c	Reference range for dechirp-on-receive
σ_0	Back-scatter coefficient of the point-like target
τ, t	Azimuth and range time variables
τ_0	Time of closest approach
v_p	Platform velocity
v_x, v_r	Target azimuth and range velocity
x_0, r_0	Target azimuth and range position at time of closest approach

The adopted geometry was the common side-looking strip-map SAR geometry as shown in Fig. 2.4. The SAR antenna, which was assumed to be moving with a constant velocity v_p through a perfectly linear trajectory, pointed along a fixed direction and its footprint illuminated a strip of the earth's surface.

Within this strip, a point-like target moved with a given azimuth and range velocity, namely v_x and v_r, which were assumed to be constant during the SAR integration time.

Let the vectors describing the time-variant position of sensor and target, respectively $\boldsymbol{p}^{\boldsymbol{sar}}(\tau)$ and $\boldsymbol{p}(\tau)$, be defined as

$$\boldsymbol{p}^{\boldsymbol{sar}}(\tau) = [p_x^{sar}(\tau),\, p_r^{sar}(\tau)] = (v_p\tau,\, 0) \tag{2.1}$$

$$\boldsymbol{p}(\tau) = [p_x(\tau),\, p_r(\tau)] = [x_0 + v_x(\tau - \tau_0),\, r_0 + v_r(\tau - \tau_0)]. \tag{2.2}$$

The leading edge of the FMCW SAR signal, which was originally transmitted at time τ, was received at time $\tau+\tau_d$. Thus, the relation between the round-trip delay τ_d and the one-way range delays is as follows

$$\tau_d = \frac{R(\tau) + R(\tau + \tau_d)}{c} \tag{2.3}$$

where

$$R(\tau) = \|\boldsymbol{p}^{\boldsymbol{sar}}(\tau) - \boldsymbol{p}(\tau)\| \tag{2.4}$$

$$R(\tau + \tau_d) = \|\boldsymbol{p}^{\boldsymbol{sar}}(\tau + \tau_d) - \boldsymbol{p}(\tau + \tau_d)\| \tag{2.5}$$

with $\|\cdot\|$ being the Euclidean norm operator. By replacing (2.5) in (2.3) and solving the resulting equation for τ_d, we obtain

$$\tau_d = 2\beta \left[\frac{R(\tau)}{c} + \frac{v^2}{c^2}(\tau - \tau_0)\right] \tag{2.6}$$

where v and β represent, respectively, the norm of the relative velocity vector and the Doppler factor, and can be expressed as

$$v = \sqrt{(v_p - v_x)^2 + v_r^2} \tag{2.7}$$

$$\beta = \frac{1}{1 - \frac{(v_p - v_x)^2 + v_r^2}{c^2}} = \frac{1}{1 - \frac{v^2}{c^2}}. \tag{2.8}$$

Equation (2.6) is slightly different from the dual result of (3) in [74] due to a different assumption on the initial geometry. The solution adopted herein allows us to obtain a neater analytical form of the round-trip delay τ_d, thus easing the following mathematical demonstration. The result in (2.6) is a general solution that holds both for the stationary and non-stationary case: in fact, when forcing $v_x = v_r = 0$, the resulting round-trip delay is equal to (4) in [69].

Assuming to linearly modulate the instantaneous frequency of the transmitted signal with chirp rate K_r, the received signal can be expressed as

$$g_r(\tau, t; \boldsymbol{p}, \boldsymbol{v}) = \sigma_0 \exp\left[j\pi K_r(t - \tau_d)^2\right] \exp\left[j2\pi f_0(t - \tau_d)\right] \tag{2.9}$$

where the vectors $\boldsymbol{p} = \boldsymbol{p}(\tau_0) = [x_0, r_0]$ and $\boldsymbol{v} = [v_x, v_r]$ highlight the dependency on the target parameters. The contribution due to the antenna pattern has been neglected since it does not affect the following results.

The received signal was then processed by means of the dechirp-on-receive technology: firstly, (2.9) was multiplied with a reference signal, that is a delayed and complex conjugated replica of the transmitted signal [73,84]. Subsequently, the Residual Video Phase (RVP) term was removed [84, 85]. At this stage, the dechirped signal can be expressed as

$$g_1(\tau, t; \boldsymbol{p}, \boldsymbol{v}) = \sigma_0 \exp\left[-j2\pi f_0(\tau_d - \tau_c)\right] \exp\left[-j2\pi K_r(t-\tau_c)(\tau_d - \tau_c)\right] \quad (2.10)$$

with τ_c being the time delay associated to the reference range for dechirp-on-receive. As the range frequency variable f is directly linked to the sweep time through the relation $K_r(t - \tau_c) \to f$, (2.10) can be rewritten as

$$g_1(\tau, f; \boldsymbol{p}, \boldsymbol{v}) = \sigma_0 \exp\left[-j2\pi(f_0 + f)(\tau_d - \tau_c)\right] \quad (2.11)$$

Finally, replacing (2.6) in (2.11) yields

$$\begin{aligned} &g_1(\tau_n, t, f; \boldsymbol{p}, \boldsymbol{v}) \\ &\quad = \sigma_0 \exp\left\{-j4\pi\beta(f_0 + f)\left[\frac{R(\tau_n + t)}{c} + \frac{v^2}{c^2}(\tau_n + t - \tau_0) - \frac{r_c}{\beta c}\right]\right\} \end{aligned} \quad (2.12)$$

where the intrinsic two-dimensional nature of the SAR signal has been made explicit by making use of the relation $\tau \to \tau_n + t$. The data are then mapped into the two-dimensional frequency domain via a Fourier Transform (FT) with respect to τ_n, yielding the following result

$$G_1(k_x, k_w; \boldsymbol{p}, \boldsymbol{v}) = \sigma_0 \exp[-j\Phi_1(k_x, k_w; \boldsymbol{p}, \boldsymbol{v})] \quad (2.13)$$

where

$$\Phi_1(k_x, k_w; \boldsymbol{p}, \boldsymbol{v}) = \gamma' \Psi(k_x, k_w; v) r_0 - k_x(v_p t) + k_x(v_p \tau_0) - k_w r_c. \quad (2.14)$$

Equation (2.14) was obtained by means of the Principle of Stationary Phase (PoSP): a step-by-step demonstration of how to derive it can be found in [69,74]. To achieve such a compact form, (2.14) was written as a function of different variables: the azimuth and slant-range wavenumber (i.e., k_x and k_w), the square root term $\Psi(\cdot)$, and the motion-dependent parameters γ and γ'. These are defined as

$$k_x = \frac{2\pi f_\tau}{v_p} \quad (2.15)$$

$$k_w = \frac{4\pi(f_0 + f)}{c} \quad (2.16)$$

$$\Psi(k_x, k_w; v) = \sqrt{\left(\beta k_w\right)^2 - \left[\frac{v}{c}\left(\beta k_w\right) + \frac{k_x}{\gamma}\right]^2} \tag{2.17}$$

$$\gamma = \frac{v}{v_p} \tag{2.18}$$

$$\gamma' = \frac{v}{(v_p - v_x)}. \tag{2.19}$$

The parameter γ, which is the well known NRS, is the ratio of the norm of the relative velocity vector to the platform velocity. The parameter γ' is defined as the ratio of the norm of the relative velocity vector to the relative azimuth speed. As shown in the subsequent sections, γ and γ' are important parameters, as they affect, respectively, the focusing of the moving target and its range registration coordinate.

The first term in (2.14) contains the azimuth modulation, the Range Cell Migration (RCM) and the range-azimuth coupling term [69]. In contrast to the stationary case, where these contributions are dependent on v_p, they are now a function of v. The second term, i.e. $-k_x(v_p t)$, is the range-invariant range walk which is caused by the motion of the platform during transmission [68]. The third term, i.e. $k_x(v_p \tau_0)$, is linearly dependent on the zero-Doppler time and defines the target azimuth coordinate of registration. The fourth and last term, i.e. $-k_w r_c$, is a constant shift intrinsically produced by the dechirp-on-receive processing.

2.3.4 Moving Target Focusing

In this section, we briefly review how to perform moving target focusing before the formation of the complex image by exploiting the NRS γ. The processing is tailored to a given motion: those targets with motion γ become focused while the remaining ones are blurred. This approach is well known in the literature as it has been adopted to perform moving target focusing in pulsed SAR data-sets [46, 77–79]. However, the theoretical foundation for the FMCW SAR scenario has not yet been explicitly derived.

Let us take into consideration the dechirped signal after azimuth FT whose phase response is described by (2.14). In order to facilitate the following discussion, the target-independent phase terms can be assumed to have been priorly removed. As a consequence, the remaining phase can be expressed as

$$\Phi_1'(k_x, k_w; \boldsymbol{p}, \boldsymbol{v}) = \gamma' \Psi(k_x, k_w; v) r_0 + k_x(v_p \tau_0) \tag{2.20}$$

where the $\Psi(\cdot)$-dependent term contains quadratic and higher order phase components. The remaining term is linear along the k_x-axis: it merely produces a constant shift along the azimuth axis, thus not affecting the quality of focusing

of the final product. Moving target focusing can be obtained by remapping the data onto a new domain in a similar fashion to conventional Stolt interpolation. This remapping is implemented by means of an interpolation designed in such a way as to linearise the phase content of the data, thus concentrating the target energy at specific coordinates. This can be formulated as

$$\Psi(k_x, k_w; v) \rightarrow k_r \tag{2.21}$$

with k_r being the newly defined range wavenumber variable. The relation between the slant-range wavenumber k_w and the range wavenumber k_r is obtained by solving (2.21) for k_w, which results in

$$k_w = \left(\frac{v_p}{c}k_x\right) + \sqrt{\left(\frac{v_p}{c}k_x\right)^2 + \frac{1}{\beta}\left[\left(\frac{k_x}{\gamma}\right)^2 + k_r^2\right]}. \tag{2.22}$$

Let us now look at the connections between moving target focusing and conventional focusing. The latter is obtained by, amongst various steps, implementing the Stolt interpolation which is defined as [69]

$$\left[\Psi(k_x, k_w; v)\right]\big|_{\substack{v_x=0\\v_r=0}} = \Psi(k_x, k_w; v_p) \rightarrow k_r. \tag{2.23}$$

The relation between the different wavenumbers is again obtained by solving (2.23) for k_w, thus yielding

$$k_w = \left(\frac{v_p}{c}k_x\right) + \sqrt{\left(\frac{v_p}{c}k_x\right)^2 + \frac{1}{\alpha}(k_x^2 + k_r^2)} \tag{2.24}$$

where α is the stationary case Doppler factor which is defined as

$$\alpha = \beta\big|_{\substack{v_x=0\\v_r=0}} = \frac{1}{1 - \frac{v_p^2}{c^2}}. \tag{2.25}$$

Comparing (2.22) with (2.24) reveals a key point. That is, moving target focusing can be obtained by using already existing algorithms, such as the WDA, as long as the platform velocity v_p is replaced by the relative velocity v. In other words, this is equivalent to rescaling v_p with the NRS γ. By doing so, those moving targets with motion γ are stationary with respect to the rescaled trajectory of the SAR platform, allowing focusing. The above considerations are in accordance with the results carried out for the pulsed SAR case, though the equations are not analytically coincident, due to the adoption of different signal models.

2.3.5 Moving Target Refocusing

The algorithm reviewed in Section 2.3.4 performs moving targets focusing at the expense of blurring the stationary background. It is necessary to process the entire raw data-set, implying a burdensome processing. Lastly, the raw data-sets are not always available, thus making it impossible to adopt the proposed approach. All these problems can be simultaneously tackled by adopting a patch-wise processing that takes as input the focused SAR image, in a similar fashion to [46].

Let us consider an image produced by means of the WDA [69]. Within this image, one moving target has been previously detected: the goal of the proposed algorithm is to refocus its signature, while leaving the neighbouring scene intact. The assumption on the use of the WDA, and thus the Stolt interpolation, implies that the mapping of the data along the k_r-axis was originally accomplished by making use of (2.24). Nonetheless, in order to focus the moving targets, (2.22) should have been used. In light of these considerations, and noting that (2.22) and (2.24) link the same slant-range wavenumber k_w to two different range wavenumbers, namely $k_{r,1}$ and $k_{r,2}$, the following relations hold

$$\frac{1}{\alpha}(k_x^2 + k_{r,1}^2) = \frac{1}{\beta}\left[\left(\frac{k_x}{\gamma}\right)^2 + k_{r,2}^2\right] \tag{2.26}$$

$$k_{r,1} = \Theta(k_x, k_{r,2}; \boldsymbol{v}) = \sqrt{\left(\frac{\alpha}{\beta\gamma^2} - 1\right)k_x^2 + \frac{\alpha}{\beta}k_{r,2}^2} \tag{2.27}$$

$$k_{r,2} = \Omega(k_x, k_{r,1}; \boldsymbol{v}) = \sqrt{\left(\frac{\beta}{\alpha} - \frac{1}{\gamma^2}\right)k_x^2 + \frac{\beta}{\alpha}k_{r,1}^2}. \tag{2.28}$$

The above equations, which are useful when expressing the phase response of the moving target signal throughout the different domains, were obtained assuming that no Doppler ambiguity phenomenon occurs. This kept the formulas compact and improved the readability of the paper; however, for a general solution, which also takes into consideration Doppler ambiguities, please refer to Section 2.6.

The phase response of the moving target signal after 2D-FT (see Fig. 2.3) can be derived on the basis of the following considerations. The original focused SAR image has been obtained by making use of, first, the Reference Function Multiplication (RFM) and, second, the Stolt interpolation, both a function of v_p. The RFM filter is defined as [69]

$$H_{RFM}(k_x, k_w) = \exp[j\Phi_{RFM}(k_x, k_w)] \tag{2.29}$$

where

$$\Phi_{RFM}(k_x, k_w) = \Psi(k_x, k_w; v_p)r_{ref} - k_x(v_p t) - k_w r_c. \tag{2.30}$$

Performing the RFM yields

$$G_2(k_x, k_w; \boldsymbol{p}, \boldsymbol{v}) = G_1(k_x, k_w; \boldsymbol{p}, \boldsymbol{v}) H_{RFM}(k_x, k_w) \\ = \sigma_0 \exp[-j\Phi_2(k_x, k_w; \boldsymbol{p}, \boldsymbol{v})] \quad (2.31)$$

where

$$\Phi_2(k_x, k_w; \boldsymbol{p}, \boldsymbol{v}) = \gamma' \Psi(k_x, k_w; v) r_0 - \Psi(k_x, k_w; v_p) r_{ref} + k_x(v_p \tau_0). \quad (2.32)$$

Subsequently, the signal was mapped into the $k_{r,1}$ domain by performing the Stolt interpolation as defined in (2.23). The signal resulting from the Stolt interpolation, which is also coincident with the output of the 2D-FT (i.e., the very first step of the proposed algorithm) can be formulated as

$$G_3(k_x, k_{r,1}; \boldsymbol{p}, \boldsymbol{v}) = \sigma_0 \exp[-j\Phi_3(k_x, k_{r,1}; \boldsymbol{p}, \boldsymbol{v})] \quad (2.33)$$

where

$$\Phi_3(k_x, k_{r,1}; \boldsymbol{p}, \boldsymbol{v}) = \Omega(k_x, k_{r,1}; \boldsymbol{v}) \gamma' r_0 - k_{r,1} r_{ref} + k_x(v_p \tau_0). \quad (2.34)$$

The processing steps specifically designed for moving target refocusing were introduced next. First, (2.26) was exploited to introduce an additional interpolation step, defined as

$$k_{r,1} \rightarrow k_{r,2}. \quad (2.35)$$

To implement (2.35), the value of γ has to be either known or estimated beforehand. A set of equally spaced tentative NRSs is therefore defined, where the extreme values are chosen according to *a-priori* knowledge of the road model and of the expected speeds. To derive the analytical form of both the required processing steps and of the final output, γ is from now on assumed to be perfectly known.

After remapping the data into the $k_{r,2}$ domain, and after simple mathematical manipulations omitted here, (2.34) can be rewritten as

$$\Phi_3(k_x, k_{r,2}; \boldsymbol{p}, \boldsymbol{v}) = k_{r,2}(\gamma' r_0 - r_{ref}) + \Big[k_{r,2} - \Theta(k_x, k_{r,2}; \boldsymbol{v})\Big] r_{ref} + k_x(v_p \tau_0). \quad (2.36)$$

The second term of (2.36) is the one responsible for moving target defocusing. It is a direct consequence of the RFM filter being matched to v_p rather than v, thus not compensating for the phase contributions due to the *actual* relative motion. Having noted this, moving target refocusing is achieved when removing this term. Let the filter $H(\cdot)$ be defined as

$$H(k_x, k_{r,2}; \boldsymbol{v}) = \exp[j\Phi(k_x, k_{r,2}; \boldsymbol{v})] \quad (2.37)$$

where

$$\Phi(k_x, k_{r,2}; \boldsymbol{v}) = \Big[k_{r,2} - \Theta(k_x, k_{r,2}; \boldsymbol{v})\Big] r_{ref}. \tag{2.38}$$

Multiplying the moving target signal by (2.37) results in

$$\begin{aligned} G_4(k_x, k_{r,2}; \boldsymbol{p}, \boldsymbol{v}) &= G_3(k_x, k_{r,2}; \boldsymbol{p}, \boldsymbol{v}) H(k_x, k_{r,2}; \boldsymbol{v}) \\ &= \sigma_0 \exp[-j\Phi_4(k_x, k_{r,2}; \boldsymbol{p}, \boldsymbol{v})] \end{aligned} \tag{2.39}$$

where

$$\Phi_4(k_x, k_{r,2}; \boldsymbol{p}, \boldsymbol{v}) = k_{r,2}(\gamma' r_0 - r_{ref}) + \frac{k_x}{\gamma}(v\tau_0). \tag{2.40}$$

Equation (2.40) shows that combining (2.35) with (2.37) correctly linearises the phase content of the data along both the k_x- and the newly defined $k_{r,2}$-axis. Finally, the refocused moving target signature is obtained by performing a Two-dimensional Inverse Fourier Transform (2D-IFT), thus yielding the following result

$$g_4(x, r; \boldsymbol{p}, \boldsymbol{v}) = \hat{w}_x(x - v\tau_0)\hat{w}_r(r - \gamma' r_0 + r_{ref}) \tag{2.41}$$

where $\hat{w}_x(\cdot)$ and $\hat{w}_r(\cdot)$ represent the azimuth and range compressed pulse envelopes, respectively.

2.3.6 Validation Methods

In order to validate the obtained products, ground measurements were collected while performing both experiments. Pictures were taken by an optical camera installed on board the platform with a 2 s sample interval. Camcorders were placed on ground at designated positions to record videos of the test-site during the acquisition of the SAR data. All available media were associated to time stamps, making it possible to relate them to the SAR images. The target of interest of Experiment #1 was equipped with two GPSs, which were the main source for the validation of the motion estimates. No GPS was available for Experiment #2, therefore preventing an accurate validation of the motion estimates. However, due to the chosen test-site, the algorithm could be tested on a variety of vehicles presenting different sizes and motions. As a consequence, the products of this experiment were mainly used to assess whether any of the target's geometric features could be extracted. To this end, the available ground measurements (i.e., pictures and videos) were exploited to infer the target's actual length, which was compared to the derived value.

Target ID	x_0	r_0	v_x	v_r
MT_1	0	1975	10	0
MT_2	0	2000	10	0
MT_3	0	2025	10	0

* $[x_0] = [y_0] = \mathrm{m},\ [v] = \mathrm{m\,s^{-1}}$;

TABLE 2.3: Ground Scene: Experiment #1

Target ID	x_0	r_0	v_x	v_r
MT_1	0	880	10	−20
MT_2	0	900	10	−20
MT_3	0	920	10	−20

* $[x_0] = [y_0] = \mathrm{m},\ [v] = \mathrm{m\,s^{-1}}$;

TABLE 2.4: Ground Scene: Experiment #2

2.4 Results

2.4.1 Simulation Results

In this section, we introduce two simulation experiments whose main goal was to illustrate the proposed method and assess its performance. The strip-map SAR geometry depicted in Fig. 2.4 was adopted here to generate the raw datasets. The system parameters, which are chosen according to realistic SAR acquisitions, are listed, respectively, in Table 2.1 and Table 2.2. The antenna pattern was assumed to be rectangular in the azimuth frequency domain to ease the computation of the azimuth resolution. The Point Spread Function (PSF) of the refocused moving target was analysed to characterize the performances of the proposed algorithm. The final assessment was derived on the basis of the following quality parameters: Impulse Response Width (IRW), Peak to Side-lobe Ratio (PSLR) and Integrated Side-lobe Ratio (ISLR).

2.4.1.1 Experiment #1

Three point-like targets with equal Radar Cross-section (RCS) were simulated on the basis of the parameters listed in Table 2.1 and Table 2.3 where Moving Target $(MT)_n$ identifies the n-th MT. This configuration defined the following set of motion parameters:

$$\left\{v \approx 39.1325,\ \ \gamma \approx 0.7965,\ \ \gamma' = 1\right\}$$

For the sake of simplicity, the ground scene was designed to force the same azimuth registration coordinate (i.e., $v\tau_0 = 0\,\mathrm{m}$) for each target. The Doppler centroid was null, thereby keeping the signal's bandwidth within defined Doppler frequencies.

Fig. 2.5a shows the SAR image obtained when focusing the stationary background with conventional SAR processing, whereas the product of the proposed algorithm is depicted in Fig. 2.5b. In order to be able to fully assess the capabilities of the algorithm, a test moving target, namely MT_2, was selected. Its PSF was extracted, up-sampled along both axes and analysed. To avoid

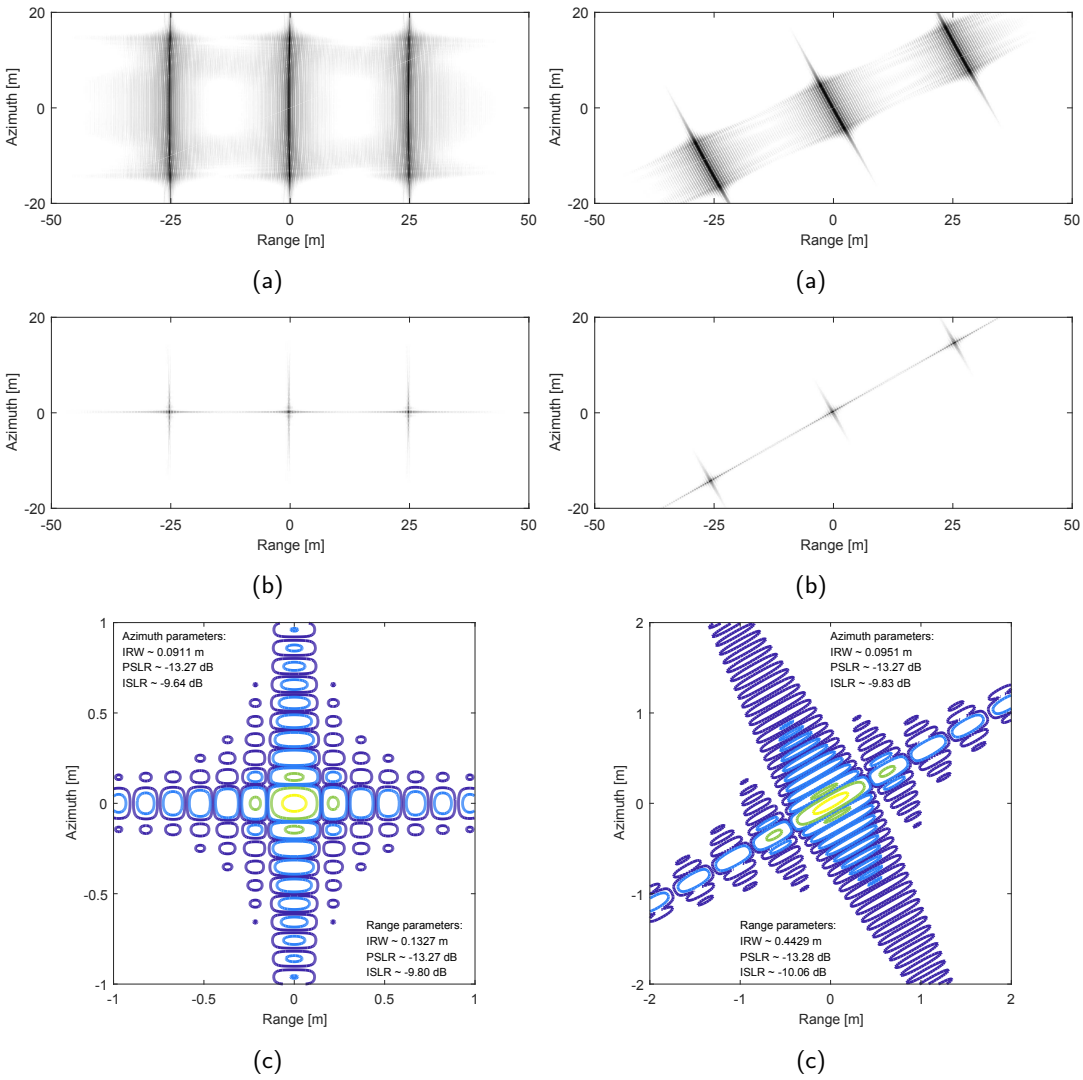

FIGURE 2.5: Experiment #1: (a) Simulated SAR image, (b) Moving target refocusing, (c) PSF after moving target refocusing: the contour lines are at −3, −15, −30 and −40 dB from the peak level

FIGURE 2.6: Experiment #2: (a) Simulated SAR image, (b) Moving target refocusing, (c) PSF after moving target refocusing: the contour lines are at −3, −15, −30 and −40 dB from the peak level

undesired interferences between different signatures, the remaining targets were removed prior to the PSF analysis. The contour of the energy distribution is shown in Fig. 2.5c: no squint was experienced due to the chosen target parameters. The theoretical azimuth and range IRW were computed by making use of, respectively, the Doppler excursion $B_x \approx 381.0931$ Hz and the range bandwidth (see Table 2.1), thus yielding $\rho_x \approx 0.0910$ m and $\rho_r \approx 0.1328$ m. The comparison between the experienced IRWs (see Fig. 2.5c) and the theoretical values, in addition to the two-dimensional PSLR deviating from the theoretical value of −13.26 dB by no more than 0.01 dB, demonstrates the reliable refocusing capabilities of the proposed algorithm.

2.4.1.2 Experiment #2

A different ground scene was simulated according to the parameters listed in Table 2.2 and Table 2.4. The new set of motion parameters was as follows

$$\left\{v \approx 32.3409,\ \ \gamma \approx 0.9132,\ \ \gamma' \approx 1.2725\right\}$$

Unlike the previous experiment, this configuration used high radial velocities, thus producing a data-set with a larger Doppler centroid (i.e., $f_{dc} = 3714.4171\,\text{Hz}$).

The resulting SAR image and refocused signature are depicted in Figs. 2.6a–2.6b. The algorithm's capabilities were once again assessed adopting the previously described procedure. The contour of the energy distribution of MT_2 is shown in Fig. 2.6c: the PSF results to be counter-clockwise rotated through an angle $\eta \approx 29.4547°$ due to the specific geometry and target's motion. The Doppler excursion $B_x \approx 267.9772\,\text{Hz}$ defines $\rho_x \approx 0.0931\,\text{m}$, whereas the range bandwidth (see Table 2.2) determines $\rho_r \approx 0.4426\,\text{m}$. The comparison between theoretical and experienced (see Fig. 2.6c) quality parameters demonstrated that a more challenging relative motion had only limited impacts on the resulting performance.

2.4.2 Experimental Results

To further investigate the performance of the method, results obtained when processing real data-takes are presented in this section. The data-takes were collected by the Fraunhofer FHR MIRANDA-35 system (see [80]) during two different campaigns.

2.4.2.1 Experiment #1

A SAR image from one of the data-takes is shown in Fig. 2.7. The result of the signature extraction step is highlighted in the red box: the target's energy was smeared over a large square area whose sides were approximately 60 m in azimuth and 15 m in range. This image was fed into the refocusing algorithm and processed according to the procedure described in Section 2.3. The GPS installed on board the target registered a slightly fluctuating speed with a mean value of $5.33\,\text{m}\,\text{s}^{-1}$ (target speed was $20\,\text{km}\,\text{h}^{-1}$). This, in combination with the specific geometry and the platform's motion, yielded the nominal NRS $\gamma_n = 0.9195$. Based on the previously described method, the set of tentative γ was defined within an interval ranging from 0.8 to 1.0 with a 0.0001 step size. The best degree of focusing was obtained with $\gamma_g = 0.9389$, thus defining a relative error of 2.11%. The resulting refocused image is shown in Fig. 2.8a:

FIGURE 2.7: Experiment #1, exemplary SAR image: (red) Moving target signature

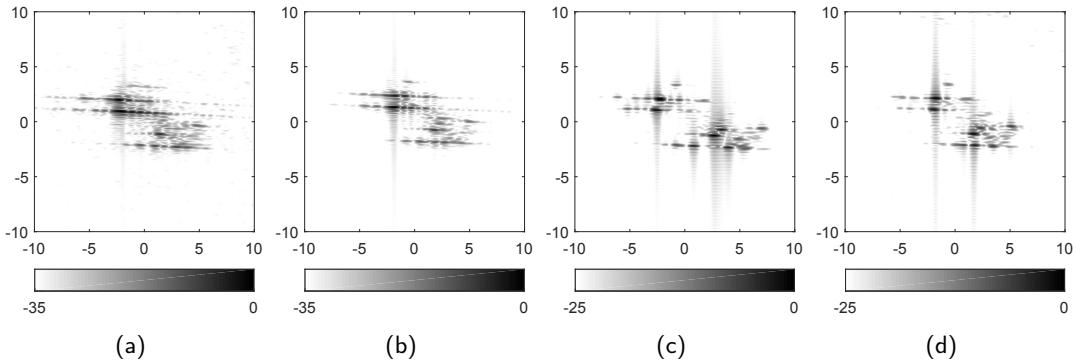

FIGURE 2.8: Experiment #1, refocused target's signatures: (a–d) Data-take #1–4

the target's signature is now limited within a much more restricted area and it is characterized by a limited number of bright scatterers.

The same procedure was then adopted to process all the available data-takes, thus yielding the SAR images depicted in Figs. 2.8a–2.8d. The four data-takes were acquired under almost identical configurations, the most prominent difference being the target speed: its nominal value was $20\,\mathrm{km\,h^{-1}}$ for data-take #1–2, and $40\,\mathrm{km\,h^{-1}}$ for data-take #3–4. The parameters of interest are summarized in Table 2.5: the v_x- and v_r-columns list the target's azimuth and range velocities as provided by the GPS, which are used to compute the nominal NRSs γ_n. These values were then used to validate the estimates γ_g: the resulting percentage errors ranged from the minimum value of 0.79 % up to the maximum value of 4.38 %. Visual inspection of the images revealed that the pair of reflectors installed on the rear of the vehicle (see Figs. 2.8a–2.8d, upper half of the signature) clearly stood out for all data-takes, whereas the front pair was recognizable only in Fig. 2.8c. The theoretical PSF registration points were derived on the basis of the available GPS data, and then compared to the obtained ones: the resulting errors (Euclidean distances) did not exceed $\approx 6\,\mathrm{cm}$.

Data-take	v_x	v_r	γ_n	γ_g	*Error*
#1	$4.42\,\mathrm{m\,s^{-1}}$	$-2.45\,\mathrm{m\,s^{-1}}$	0.9195	0.9389	2.11 %
#2	$4.46\,\mathrm{m\,s^{-1}}$	$-2.44\,\mathrm{m\,s^{-1}}$	0.9187	0.9590	4.38 %
#3	$7.50\,\mathrm{m\,s^{-1}}$	$-4.09\,\mathrm{m\,s^{-1}}$	0.8671	0.8740	0.79 %
#4	$7.58\,\mathrm{m\,s^{-1}}$	$-4.09\,\mathrm{m\,s^{-1}}$	0.8657	0.8964	3.54 %

TABLE 2.5: Results: Experiment #1

(a) (b)

FIGURE 2.9: Experiment #2: (a) Exemplary SAR image: (red) Moving target signature, (b) Corresponding optical image: (red) Moving target image

2.4.2.2 Experiment #2

The available data-take recorded the A61 highway traffic flow during non-rush hours for an approximate duration of 1 min. The data were subdivided into overlapping sub-apertures whose dimension was defined on the basis of the adopted RADAR parameters (see Table 2.2). The azimuth size of the antenna footprint at the mid-swath slant-range can be quantified as $\approx 67.45\,\mathrm{m}$, equivalent to approximately 19 374 pulses. In light of the above, the number of integrated pulses was set to 20 480 (i.e., $\approx 3.02\,\mathrm{s}$), thereby ensuring that the $-3\,\mathrm{dB}$ azimuth beam-width would be fully processed. Within the overall SAR acquisition time, a variety of moving targets drove by in both directions. However, due to the adopted geometry and the specific test-site, trees would frequently occlude the sight to the closer carriageway, thereby substantially affecting the targets' signatures. As a consequence, those targets driving along the aforementioned carriageway were not taken into consideration when assessing the algorithm's refocusing capabilities.

The SAR image of a sub-aperture is depicted in Fig. 2.9a and the respective optical image is shown in Fig. 2.9b. Within the integration time, the antenna

illuminated two moving targets whose elongated signatures were easily recognizable outside the main beam clutter. This stems from the use of a high Pulse Repetition Frequency (PRF) which ensured two quite distinct zones: the endo-clutter zone (see Fig. 2.9a, center) which exhibited the information due to the stationary scene, and the exo-clutter zone (see Fig. 2.9a, left and right) where only moving targets were imaged. The target of interest, highlighted in the red box on both images, was a medium-sized light commercial vehicle moving at high speed along the highway. The sense of its motion was opposite to that of the platform, thus defining a relative velocity vector with a large absolute value. Its energy was smeared over an area with an extension along the azimuth axis of approximately 120 m, which is induced by a large excursion of the radial velocity within the integration time. The signature of interest was extracted and subsequently fed into the proposed algorithm: the best degree of focusing was obtained when processing with $\gamma_g = 1.9427$. The resulting refocused image is shown in Fig. 2.10k.

Based on the available optical images, 18 targets drove along the visible carriageway (i.e., the one opposite sensor's direction). Their signatures were all detected and fed into the refocusing algorithm: the resulting refocused images, combined with the respective optical images, are shown in Fig. 2.10. In order to extract the length of the main axis, the energy image of each refocused signature was compared to a threshold dependent on the specific noise level. Morphological filtering was then performed in order to remove undesired detections (i.e., for instance, contributions due to the secondary lobes of bright scatterers) and to aggregate nearby detections. The resulting lengths, together with other parameters of interest, are summarized in the captions of Fig. 2.10: L_{sar} and L_{opt} represent the lengths derived from SAR and optical images, the latter herein assumed to be the *true* length. The parameter μ exhibits the average value of the squint angle computed at the mid-swath slant-range: substantial differences existed even between adjacent sub-apertures due to the use of an ultra-light-weight platform. Lastly, δ represents the relative orientation of the target trajectory with respect to the sensor's flightpath.

Comparing L_{sar} with L_{opt} revealed that the SAR-derived lengths underestimated the *true* ones: the absolute value of the error ranged from 0.03 m up to 3.26 m, with a mean value of 1.33 m. Nonetheless, the refocused signatures clearly exhibited information on the targets' dimensions, thus making it possible to discriminate between small and large targets.

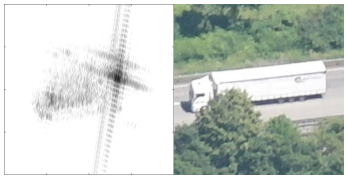

(a) $\gamma_g = 1.4951$, $L_{sar} = 12.21$, $L_{opt} = 15.15$, $\mu = 8.99$, $\delta = 9.80$

(b) $\gamma_g = 1.5135$, $L_{sar} = 12.81$, $L_{opt} = 14.94$, $\mu = 8.80$, $\delta = 10.20$

(c) $\gamma_g = 1.5417$, $L_{sar} = 3.18$, $L_{opt} = 3.44$, $\mu = 8.53$, $\delta = 8.75$

(d) $\gamma_g = 1.5121$, $L_{sar} = 12.17$, $L_{opt} = 15.34$, $\mu = 7.75$, $\delta = 8.75$

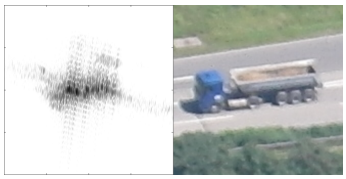

(e) $\gamma_g = 1.5911$, $L_{sar} = 8.65$, $L_{opt} = 10.75$, $\mu = 7.27$, $\delta = 7.75$

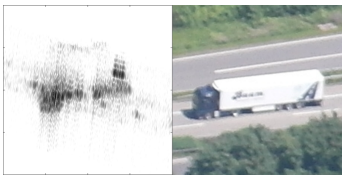

(f) $\gamma_g = 1.6038$, $L_{sar} = 12.19$, $L_{opt} = 15.45$, $\mu = 6.99$, $\delta = 8.00$

(g) $\gamma_g = 1.5855$, $L_{sar} = 8.94$, $L_{opt} = 10.43$, $\mu = 7.03$, $\delta = 8.00$

(h) $\gamma_g = 1.7478$, $L_{sar} = 3.85$, $L_{opt} = 5.40$, $\mu = 7.05$, $\delta = 8.00$

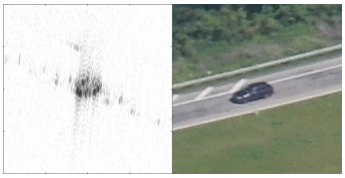

(i) $\gamma_g = 1.9060$, $L_{sar} = 4.04$, $L_{opt} = 4.07$, $\mu = 5.49$, $\delta = 18.70$

(j) $\gamma_g = 1.9511$, $L_{sar} = 3.40$, $L_{opt} = 3.45$, $\mu = 4.70$, $\delta = 5.00$

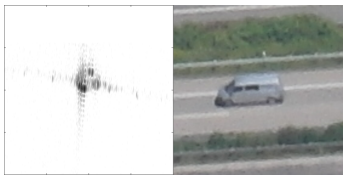

(k) $\gamma_g = 1.9427$, $L_{sar} = 3.35$, $L_{opt} = 5.21$, $\mu = 4.59$, $\delta = 2.50$

(l) $\gamma_g = 1.8848$, $L_{sar} = 3.55$, $L_{opt} = 4.20$, $\mu = 2.77$, $\delta = 3.05$

(m) $\gamma_g = 1.6928$, $L_{sar} = 14.24$, $L_{opt} = 15.36$, $\mu = 5.51$, $\delta = 10.75$

(n) $\gamma_g = 1.7041$, $L_{sar} = 7.08$, $L_{opt} = 7.94$, $\mu = 5.35$, $\delta = 10.75$

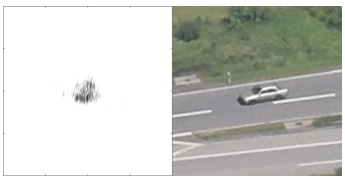

(o) $\gamma_g = 1.5911$, $L_{sar} = 3.57$, $L_{opt} = 3.67$, $\mu = 4.79$, $\delta = 10.55$

(p) $\gamma_g = 1.7916$, $L_{sar} = 3.54$, $L_{opt} = 4.20$, $\mu = 4.69$, $\delta = 10.55$

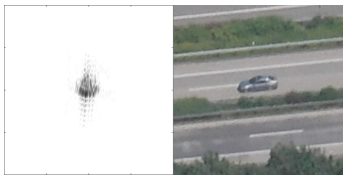

(q) $\gamma_g = 2.0274$, $L_{sar} = 3.04$, $L_{opt} = 4.28$, $\mu = 5.53$, $\delta = 4.90$

(r) $\gamma_g = 1.7676$, $L_{sar} = 6.88$, $L_{opt} = 7.43$, $\mu = 3.13$, $\delta = 4.50$

FIGURE 2.10: Experiment #2, refocused targets' signatures (10 m × 10 m) and corresponding optical images: (a–r) Targets of interest, (caption) γ_g: NRS estimate, L_{sar}: SAR-derived length [m], L_{opt}: *true* length [m], μ: squint angle [deg], δ: relative orientation [deg]

2.5 Discussion

2.5.1 General Comments

The input signal of the proposed algorithm should consist only of the contribution from the moving target of interest. However, additional components such as thermal noise and clutter, which is the signal being back-scattered by undesired targets, were also measured. The superimposition of such signals on the one of interest, in addition to the smearing of the target's energy, can jeopardize the success of the method. Nevertheless, all data-takes discussed herein benefited from favourable circumstances. For Experiment #1, the use of corner reflectors ensured that the target emerged from ground clutter, and thus the contribution due to the latter was assumed to be negligible. Contrariwise, for Experiment #2, targets were imaged in the exo-clutter zone, reducing the interference signal to mainly thermal noise. In light of the above, not only was the detection step uncomplicated, but also the refocusing products were marginally affected. However, when such conditions are not met, clutter rejecting techniques such as STAP (see [43]) should be implemented prior to or in combination with the proposed method.

2.5.2 Refocusing Algorithm

The percentage error committed when estimating the NRS for Experiment #1 ranged between 0.79 % and 4.38 %. Though the estimates were reasonably accurate, interpreting the outputs depicted in Figs. 2.8a–2.8d might not be straightforward. Nonetheless, the following remarks should be kept in mind. First, the energy back-scattered by the corner reflectors was much larger than that from the different structures of the truck. Hence, when refocusing the signature of the target, the contributions due to the corner reflectors were predominant and the truck itself was barely distinguishable. Moreover, as two pairs of reflectors were deployed, one would expect four extremely bright scatterers to stand out in the refocused images. However, although the pair installed on the rear of the truck was visible irrespective of the data-take, the front one did not clearly emerge from the background. Understanding what might have induced such effects is a challenging task, and all the potential causes herein provided are speculative. The spatial proximity between the front pair and the truck cab, also mainly made of metallic materials, could result in defining the effects depicted in the lower half of Figs. 2.8a–2.8d. Also, a faulty installation of the reflectors during the experiment set-up could lead to a non-ideal illumination, thereby preventing the proposed method from precisely refocusing the targets.

Limited ground measurements were available for Experiment #2. Nonetheless, analysing the optical media allowed us to infer the behaviour of the traffic

flow, and to assess the coherency of the estimates. All the large targets (i.e., trucks) moved along the slow-lane of the carriageway at moderate speeds. Contrariwise, small- and medium-sized moving targets (i.e., private cars or light commercial vehicles) exhibited much more diverse motion behaviours. Of particular interest was the car with ID i which was illuminated by the antenna main beam while driving along the connection road between two different highways (see Fig. 2.2, upper blue line). Though moving at a much slower speed compared to other cars, its relative orientation δ defined a substantial range velocity v_r, which translated into a large NRS. The ID q drove along the fast-lane of the carriageway overtaking other vehicles: the specific geometry induced a considerable azimuth velocity v_x, thus defining the largest NRS among the targets of interest. The refocused images could then be exploited to infer whether a given signature was due to a small- or a large-sized vehicle. Although the target's dimensions were preserved in the refocused image (i.e., larger targets induced larger signatures, and vice-versa), the SAR-derived lengths underestimated the *true* ones: the minimum and maximum values of the absolute errors were 0.03 m and 3.26 m respectively, and the mean value was 1.33 m. Nonetheless, the received signal depends on a variety of factors such as the squint angle μ, the relative orientation δ, the target's anisotropic three-dimensional back-scattering properties and its integration time. The latter, that is the time during which the target is illuminated by the antenna main beam, is a fraction of the adopted SAR integration time (i.e., ≈ 3.02 s) as the targets of interest moved opposite to the sensor. In light of that, extracting geometric features from refocused images appears to be quite a challenging task. However, the obtained products demonstrated the feasibility of differentiating vehicle types (i.e., small-, mid- and large-sized targets) on the basis of their signatures. Furthermore, provided that favourable conditions are met, it is also possible to isolate different features within a single signature. A significant example is given by ID n: not only the strong reflectors at the front and rear of the truck were clearly imaged, but also the vertical profile of the truck was preserved.

The following considerations should be taken into account when interpreting the results from both experiments. The data-takes were collected by a millimetre-wave sensor. This made the refocusing much more challenging as the NRS estimate had to be highly accurate to compensate for range histories with a millimetre accuracy. Also, the mismatching of the actual target's motion from the adopted model had a larger impact: small accelerations, which would be negligible when using different RADAR parameters, were critical in our experiments. Nonetheless, although the processing of such data-takes was not trivial, the proposed method proved to be capable of accurately estimating the NRS and of refocusing non-cooperative targets' signatures with satisfying performance.

2.5.3 Summary and Outlook

This paper has presented how to refocus FMCW SAR moving target data by making use of both the WDA and the NRS concept. A limited amount of relevant work has been carried out to research either the imaging or the indication of moving targets in FMCW SAR environments. First, the moving target Point Target Reference Spectrum (PTRS) was derived and expressed in the same analytical form adopted within previously published works that addressed the same problem in a stationary case. From simple visual comparisons between the two PTRSs, it appears clear that the main difference was the parameter describing the relative motion between sensor and target. As a consequence, moving target focusing can be performed by means of the WDA as long as the platform's speed (or the NRS) is replaced with a dual parameter describing the relative motion between sensor and target. The above considerations were then exploited to design a method to refocus moving target signatures. This consisted of two main steps. The first was a remapping of the data onto a new more favourable domain. The second filtered out those residual phase components that *survived* the WDA processing and which were responsible for target defocusing. The method has been tested and validated in a number of ways. Simulations were performed to assess whether the performances would match the expected values. The algorithm behaviour was further investigated by processing real data collected in two distinct experiments. The availability of detailed ground measurements allowed for an accurate validation of the products of Experiment #1: the NRSs were estimated with a relative error up to 4.38%, whereas the registration points of the reflectors were within a 6 cm distance from their theoretical positions. As for Experiment #2, estimates of the target's length and shape were retrieved, therefore allowing for a differentiation of the targets on ground.

The current technological advances suggest that millimetre-wave, centimetre resolution, miniaturized SAR systems are about to become commonly adopted solutions. In light of the above, particular attention should be devoted to designing refocusing (or auto-focusing) techniques not bounded by any assumptions on the relative motion. Also, adopting centimetre resolution systems allows discrimination of the multiple scatterers of the target, each characterized by slightly different motions. Thus, not only the assumption of a constant velocity should be dropped, but also the assumption of a common motion for all the scatterers results in a sub-optimal approach. Future research activities shall focus on imaging moving targets whose signatures are either registered close by or partially overlapped. A particular emphasis shall be put on analysing the impact on the resulting motion estimates, and on assessing the corresponding re-location performance.

2.6 Appendix

The core equations for moving target focusing and refocusing [i.e., respectively, (2.22) and (2.27)] are based on the assumption that the azimuth spectrum is contained within the unambiguous wavenumber bandwidth. Nonetheless, this condition is very unlikely to hold in realistic scenarios, suggesting the need for a general solution. To successfully deal with ambiguous spectra, the ambiguity number M has to be estimated beforehand [86]. Although this is a crucial step, the estimation process is beyond the scope of this work, and M is consequently assumed to be perfectly known.

Let the ambiguous azimuth wavenumber k_x^* be defined as

$$k_x^* = \frac{2\pi f_\tau}{v_p} + \frac{2\pi M \times PRF}{v_p} \tag{2.42}$$

To take into account the ambiguous nature of the spectrum, (2.17) has to be modified by replacing k_x by k_x^*. The relation between k_w and k_r can be obtained by following the procedure described in Section 2.3.4, thus yielding

$$k_w = f(k_x^*, k_r; \boldsymbol{v}) = \left(\frac{v_p}{c} k_x^*\right) + \sqrt{\left(\frac{v_p}{c} k_x^*\right)^2 + \frac{1}{\beta}\left[\left(\frac{k_x^*}{\gamma}\right)^2 + k_r^2\right]} \tag{2.43}$$

The equation linking the range wavenumbers $k_{r,1}$ and $k_{r,2}$ is obtained by equalizing (2.43) and (2.24), and solving for the desired wavenumber. The solution, which is obtained through simple mathematical manipulations omitted here, can be expressed as

$$\begin{aligned} k_{r,1} &= \Upsilon(k_x^*, k_{r,2}; \boldsymbol{v}) \\ &= \left\{ -\ k_x^2 + \alpha\left\{\left[f(k_x^*, k_{r,2}; \boldsymbol{v}) - \left(\frac{v_p}{c} k_x\right)\right]^2 - \left(\frac{v_p}{c} k_x\right)^2\right\}\right\}^{\frac{1}{2}} \end{aligned} \tag{2.44}$$

Chapter 3

Moving Target Refocusing With the FMCW SAR System MIRANDA-35

Emiliano Casalini, Julian Fagir and Daniel Henke

This chapter is based on the peer-reviewed article: IEEE Journal of Selected Topics in Applied Earth Observations and Remote Sensing, vol. 14, pp. 1283–1291, 2020; DOI: 10.1109/JSTARS.2020.3042601. It is reprinted as the final submitted manuscript and has been modified to fit the layout of this thesis.

E. Casalini and D. Henke conceptualized the study. E. Casalini elaborated the methodology, performed the analysis and interpreted the results. J. Fagir contributed to the analysis. D. Henke contributed to the analysis and the interpretation of the results. E. Casalini wrote the first draft of the manuscript. E. Casalini and D. Henke participated in the writing and editing of the final manuscript.

3.1 Abstract

ISAR is a commonly adopted technique for producing high resolution images of moving targets. This paper investigates the imaging capabilities of high-frequency and high-bandwidth systems by means of two distinct experiments. The deployed sensor is the Fraunhofer FHR MIRANDA-35, a millimeter-wave SAR airborne system which transmits frequency-modulated continuous-wave FMCW signals at Ka-band and is capable of achieving centimeter resolution. The performances are assessed by comparing the derived estimates (e.g., radial velocity and acceleration, and dimensions) with independent ground measurements. The resulting accuracy can be summarized as follows: the mean value of the percent error is 2.05 % and 2.11 % for radial velocity and acceleration, respectively, and 4.27 % for the target dimensions.

3.2 Introduction

SAR systems are frequently exploited solutions for earth surface monitoring in all-weather and all-light conditions. Such systems are capable of producing electromagnetic images with enhanced spatial resolution [32], and therefore are a useful tool for, amongst many applications, surveillance and reconnaissance purposes [87, 88]. The need for a broad accessibility to SAR has led to the design of frequency-modulated continuous-wave FMCW waveforms [84]. FMCW SAR differentiates from pulsed SAR due to the transmission of a frequency-modulated signal which covers most of the Pulse Repetition Interval (PRI). As a consequence, high Signal-to-Noise Ratio (SNR) values can be obtained even when using low transmission powers, thus making the system more compact and cost-effective. A detailed analysis of the FMCW SAR signal model, its resulting signal processing aspects and viable hardware solutions can be found in [68].

Conventional SAR processing is designed to compensate for the quadratic and higher order phase terms produced by the static scene. As a consequence, moving targets signals are not coherently integrated, thereby producing signatures which are both blurred and displaced along-track [40]. Many publications have dealt with the imaging of moving targets in SAR images [45, 46, 49, 66, 89]. In [49], the authors derive the moving target image impulse response and its spectrum, which is then used to perform matched filtering. A two-dimensional matched filtering without *a-priori* knowledge of the accurate motion parameters can successfully correct the range cell migration [89]. Alternatively, well-known SAR processors can be adjusted for RADAR imaging purposes: a bank of focusing filters based on the chirp scaling algorithm can efficiently image moving targets [45]. Furthermore, the concept of NRS has been used to modify the

WDA for both pulsed [46] and FMCW SAR [66]. Though yielding fairly good results, the aforementioned algorithms are based upon simplified range history models, which are unlikely to hold, for instance, in maritime scenarios where targets undergo complicated angular motions (e.g., roll, pitch and yaw). This calls for more sophisticated techniques, such as ISAR [50, 51], which is capable of dealing with a wider range of target dynamics. Its main drawback is represented by the unpredictable azimuth resolution which depends on the unknown target dynamics and cannot, therefore, be estimated beforehand. However, ISAR succeeds where most of algorithms fail, thus making it a powerful tool for a number of applications. In light of recent technological developments, ISAR theory has been generalized to include FMCW waveforms: in [56], the authors analyze the image distortions introduced when using such signals and present a more general solution. However, FMCW ISAR algorithms, such as the one introduced in [56], were only applied to X-band data-sets with meter scale range resolution. It remains an open question as to whether such algorithms can successfully process data-sets acquired at higher frequencies and with larger bandwidths.

In this paper, we introduce the Ka-band Fraunhofer FHR MIRANDA-35 experimental sensor [80]. Its RADAR imaging capabilities are discussed on the basis of experimental results obtained when combining state-of-the-art techniques, in a similar fashion to [55]. However, unlike previously published works, the implemented method comprises both pulsed and FMCW SAR techniques that have been developed separately and have never been used in combination. Moreover, in light of its main features (e.g., millimeter-wave wavelength, FMCW technology and ultra-light-weight airborne platform), MIRANDA-35 results to be an interesting case study as the need for extremely compact and low-cost systems, yet characterized by satisfying performances, is raising. Lastly, the results presented herein are of importance as FMCW ISAR processing has never been tested with Ka-band data-sets. At such wavelengths, the target range history needs to be estimated with millimeter accuracy, thereby making the refocusing task way more challenging.

The remainder of the paper is organized as follows. In Section 3.3.1 we introduce the MIRANDA-35 sensor, its specifications and we describe the experiments' set-ups. Section 3.3.2 reviews the implemented processing chain whereas Section 3.3.3 describes the available ground measurements used for validation. The obtained performances were assessed by processing real data-sets acquired during two different experiments, and they are summarized in Section 3.4.1 and 3.4.2. Results and future research directions are thoroughly discussed in Section 3.5.

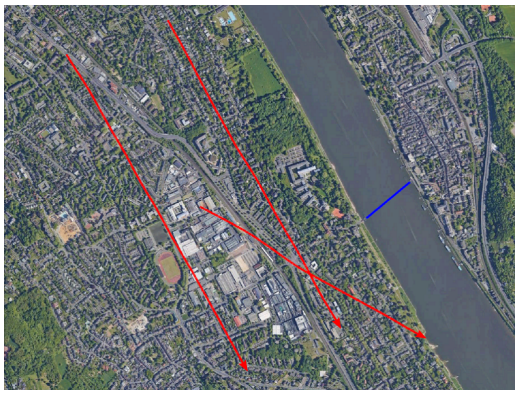

FIGURE 3.1: Experiment #1. Google Earth image of the *Königswinter* test-site: sensor's flightpaths (red), and target's path (blue).

Data-take	#1	#2	#3
Bandwidth [GHz]	0.6	1.25	0.6
PRF [kHz]	10.17	2.54	10.17
Mid-range [m]	622.39	1247.20	622.39
Swath width [m]	235.5	455.47	235.5
Velocity [$\mathrm{m\,s^{-1}}$]	32.63 ± 0.09	35.33 ± 0.03	30.84 ± 0.04
Roll [deg]	0.79 ± 1.23	2.25 ± 0.49	2.33 ± 0.84
Pitch [deg]	-1.35 ± 0.07	-0.17 ± 0.06	1.71 ± 0.23
Yaw [deg]	156.15 ± 0.11	159.56 ± 0.52	126.74 ± 0.14

TABLE 3.1: System and Motion Parameters: Experiment #1

3.3 Method

3.3.1 Sensor and Experimental Set-up

The SAR sensor utilized in the experiments was the Fraunhofer FHR MIRANDA-35 system [80]. This is an airborne sensor transmitting FMCW signals and operating at 35 GHz frequency. The system is composed of one transmitting and up to four receiving antennas which can be arranged both along- and cross-track, thereby allowing for a variety of applications. The minimum and maximum PRF are 1271.57 Hz and 10 172.53 Hz, respectively, whereas the largest usable bandwidth is equal to 1.25 GHz, thus defining a maximum range resolution of 12 cm. Due to its compactness, MIRANDA-35 is mounted on board the ultra-light-weight FHR Delphin platform. Two experiments, held during distinct campaigns, are briefly discussed here.

Data-take	#1	#2	#3
Bandwidth [GHz]	1	1	1
PRF [kHz]	1.69	1.27	1.69
Mid-range [m]	2003.32	2916.46	2003.32
Swath width [m]	791.06	1078.78	791.06
Velocity [$\mathrm{m\,s^{-1}}$]	54.09 ± 0.07	54.18 ± 0.04	55.17 ± 0.02
Roll [deg]	-0.18 ± 0.23	-0.13 ± 0.19	-0.46 ± 0.10
Pitch [deg]	0.34 ± 0.04	0.22 ± 0.13	-0.74 ± 0.02
Yaw [deg]	103.37 ± 0.24	105.48 ± 0.05	100.78 ± 0.11

TABLE 3.2: System and Motion Parameters: Experiment #2

3.3.1.1 Experiment #1

The experiment was conducted in Summer 2018 in the municipality of *Königswinter*, in the district *Rhein-Sieg*, Germany. The mission was designed in order to record the activities of the ferry *Königswinter IV*. The experimental set-up is depicted in Fig. 3.1. The nominal values of the most notable system parameters, together with mean and standard deviation of the platform motion parameters, are listed in Table 3.1.

3.3.1.2 Experiment #2

The experiment was conducted in Summer 2017 in the surroundings of the town of *Thun*, in the canton of *Bern*, Switzerland. The mission was designed in order to study the case of a ground target (i.e., a medium-sized truck) moving at moderate speed along a linear trajectory. The target of interest was equipped with four dihedral corner reflectors attached on two poles at different heights. Table 3.2 summarizes the nominal values of the main system parameters and, additionally, it provides mean and standard deviation of the platform motion parameters. For a more detailed description of the experiment, please refer to [66].

3.3.2 Processing Chain

The main steps of the implemented algorithm are summarized in the block diagram of Fig. 3.2, where intermediate Fourier transforms and other minor operations are omitted for the sake of clarity. The input consists of a processed SAR image in RADAR geometry (i.e., range and cross-range), whereas the output consists of the target refocused signature. The implemented algorithm is capable of dealing with images produced by any focusing algorithm as long as the proper image inversion mapping is exploited. The examples shown within

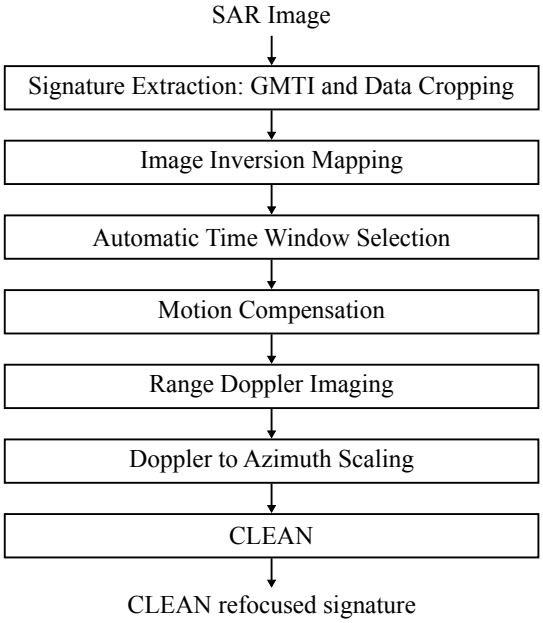

FIGURE 3.2: Block diagram of the implemented algorithm.

this paper, and thus the related inversion mapping, were produced on the basis of the WDA for FMCW signals [69].

3.3.2.1 GMTI and Data Cropping

The multiple spatial degrees of freedom offered by MIRANDA-35 are exploited in order to perform ATI [41]. The resulting interferogram is passed on to a two-dimensional adaptive non-parametric Constant False Alarm Rate (CFAR) detector to determine whether the pixel of interest is occupied by a moving target [90]. This technique estimates the magnitude-phase joint Probability Density Function (PDF) of the terrain interferogram via a histogram-based approach, and it detects potential moving targets by exploiting a threshold contour line. Then, the derived detections are grouped together and de-noised by means of morphological filtering [81]. Consequently, contiguous objects generated by the same target are connected by making use of the border tracing algorithm presented in [82]. Lastly, a rectangular crop is defined based on centroid and size of the final object, and the useful signal is extracted from the SAR image.

3.3.2.2 Image Inversion Mapping

The image inversion mapping is designed on the basis of the focusing technique that was used to produce the algorithm input. The examples shown within this paper were obtained by making use of the WDA for FMCW signals [69]: such an algorithm has proven itself capable of handling high-squint configurations, thereby making it suitable for an ultra-light-weight airborne platform. Its main steps are listed sequentially in the order they are performed: RVP removal,

RFM and Stolt interpolation. The latter represents the main core of the WDA: it is implemented in the two-dimensional wavenumber domain and is designed to linearise the phase content of the data.

The obtained crop, which is represented in RADAR geometry, is remapped in the two-dimensional wavenumber domain by performing an IFT and a Fourier transform FT along the range and azimuth axis, respectively. Let the azimuth wavenumber be referred to as k_x, whereas the slant-range and range wavenumber (i.e., the variable describing the signal along the range direction before and after applying the Stolt interpolation) are k_w and k_r, respectively. The inversion mapping can be formulated as

$$k_r \rightarrow k_w \tag{3.1}$$

where the relation between the different wavenumbers is as follows:

$$k_r = \sqrt{\left(\alpha k_w\right)^2 - \left[\frac{v_p}{c}\left(\alpha k_w\right) + k_x\right]^2} \tag{3.2}$$

with v_p and c being the platform velocity and the speed of light, respectively, and α is the stationary case Doppler factor defined as

$$\alpha = \frac{1}{1 - \frac{v_p^2}{c^2}}. \tag{3.3}$$

The subsequent step consists of reintroducing the range-invariant phase contribution originally removed by the RFM. This is performed by multiplying the output of the inverse Stolt interpolation with a filter whose phase response is expressed as

$$\Phi_{RFM}(k_x, k_w; v_p) = -\sqrt{\left(\alpha k_w\right)^2 - \left[\frac{v_p}{c}\left(\alpha k_w\right) + k_x\right]^2}\, r_{ref} + k_x(v_p t_s) \tag{3.4}$$

with t_s being the fast-time. The last term in (3.4), i.e. $k_x(v_p t_s)$, is the range-invariant range walk which is caused by the motion of the platform during transmission [68]. Lastly, after mapping the signal into the range domain through a FT, the RVP term is restored by means of a filter which introduces a range dependent delay [84]. Its phase response can be expressed as follows:

$$\Phi_{RVP}(r) = \frac{\pi}{\gamma}\left(\gamma\frac{2r}{c}\right)^2 \tag{3.5}$$

where γ and r represent the transmitted signal chirp rate and the range axis, respectively.

The term $(v_p/c)(\alpha k_w)$ in (3.2) and (3.4) is unique to FMCW SAR environments and describes the range-azimuth coupling produced by the sensor motion

during the transmission of the signal. The pulsed SAR solution can be obtained by forcing the sensor position to be stationary during transmission, which is known as stop-and-go approximation. This can be factored into (3.1)–(3.5) by replacing $v_p = 0$.

3.3.2.3 Automatic Time Window Selection

The illumination time for a given target on ground varies greatly depending on a variety of factors (e.g., acquisition geometry, antenna pattern, relative motion between sensor and target, etc.). Within this time span, which can reach up to few seconds for airborne scenarios, the target motion results to be fairly complicated, and conventional imaging algorithms, such as the range Doppler technique, fail. In order to successfully perform RADAR imaging, only a subset of the available echoes (i.e., a window) needs to be processed. Its selection is based on the maximum contrast automatic time window selection algorithm proposed in [91]: the image with the highest contrast determines the *optimum* window position and length.

3.3.2.4 Motion Compensation

Motion Compensation (MoComp) is a crucial step for ISAR processing. The received signal exhibits a phase modulation which is a function of the range variation over time between focusing point and antenna phase center. In case this contribution was not perfectly compensated for, the residual phase term would induce defocusing, thereby jeopardizing the successful interpretation of the final products. In [56], the authors designed a MoComp algorithm for FMCW SAR: as the stop-and-go approximation is no longer valid, the phase modulation results to be dependent on both the fast-time t_s and the slow-time variable n.

The received signal, which was derived in [56], can be expressed as follows:

$$S_b(t_s, n) = K' w(t_s, n, T_s) e^{j\phi_0(t_s, n)} \int_V g(\boldsymbol{x}) e^{j\phi(t_s, n, \boldsymbol{x})} \, \mathrm{d}\boldsymbol{x} \tag{3.6}$$

where $\boldsymbol{x}$ represents the position of a given scatterer, and $g(\cdot)$ is the target reflectivity function. The signal domain, which is identified by $w(\cdot)$, can be approximated as

$$w(t_s, n, T_s) \approx rect\left(\frac{t_s - nT_s}{T_s}\right) \tag{3.7}$$

with T_s being the PRI. Furthermore, the exponential $\phi_0(\cdot)$ in (3.6) can be expressed as follows:

$$\begin{aligned}\phi_0(t_s,n) &= -2\pi(f_c+\gamma t_s)\tau_0(t_s,n)+\pi\gamma\tau_0^2(t_s,n)\\ &= -2\pi(f_c+\gamma t_s)\frac{2R_0(t_s,n)}{c}+\pi\gamma\left(\frac{2R_0(t_s,n)}{c}\right)^2\end{aligned} \tag{3.8}$$

where f_c represents the transmitted signal carrier frequency whereas $R_0(t_s,n)$ describes the range history of the target focusing point.

In case no *a-priori* knowledge was available, $R_0(t_s,n)$ would need to be estimated on the basis of the received signal, thereby introducing the concept of ISAR autofocusing. Autofocusing techniques can be subdivided into two different categories: parametric and non-parametric [92]. The examples shown within this paper were obtained by exploiting the so-called image contrast based technique [93]. This is a parametric technique that models $R_0(t_s,n)$ via a finite-order polynomial as

$$R_0(t_s,n)=\sum_{n=0}^{N}\frac{a_n(t_s+nT_s)^n}{n!} \tag{3.9}$$

The polynomial degree N is empirically designed: for common maritime and ground targets, two coefficients (i.e., the radial velocity and acceleration) describe the range history with sufficient accuracy. On the other hand, the estimate of the polynomial coefficient a_n is obtained by maximizing the contrast of the refocused signature, and the optimization problem is solved by making use of the Nelder–Mead method.

Equation (3.9) emphasizes how the complexity of the MoComp crucially increases in FMCW SAR scenarios. In fact, the number of radial distances that needs to be estimated is equal to $N_f \times N_s$, with N_f and N_s being the number of estimates along the fast- and slow-time, respectively.

3.3.2.5 Range Doppler Imaging

A FT performed along the slow-time successfully implements the range Doppler technique provided that the Fourier domain of the received signal can be approximated with a rectangular grid. This is obtained when the following conditions are satisfied: (i) the effective rotation vector is approximately constant, (ii) the variation of the viewing angle within the integration time is small, and (iii) the signal is narrow-band [50, 51].

After implementation of the range Doppler technique, the energy due to a given scatterer is concentrated at a specific Doppler frequency. Though the imaging formation process is fairly simple, the resulting output is represented

in a non-homogeneous range/Doppler domain, thus making it impossible to retrieve the desired geometric features.

3.3.2.6 Doppler to Cross-range Scaling

Converting Doppler into cross-ranges is a mandatory step in order to represent the refocused signature in a homogeneous domain. As pointed out in [94], the slow-time signal produced by a given scatterer is dependent on the target dynamics. More precisely, both Doppler and chirp-rate are a function of, amongst other parameters, the effective rotation vector modulus Ω_{eff}, which defines the total variation of the viewing angle within the integration time. The relation between chirp-rate and Ω_{eff} can be expressed as follows:

$$m_k = \frac{2f_0\Omega_{eff}^2}{c} r_k \tag{3.10}$$

Equation (3.10) describes a line with axes m_k and r_k representing the chirp-rate and range of the kth scatterer, respectively. The points of such line can be obtained by making use of basic image and signal processing techniques. The PSF of a given scatterer is extracted through image segmentation, and back-projected into the slow-time domain via an IFT. Consequently, the Local Polynomial Fourier Transform (LPFT) is exploited in order to assess what chirp-rate guarantees the best focusing. Then, provided a meaningful set of scatterers is available, it is possible to estimate the slope of the line by means of a Least Square Error (LSE) approach, and thus to derive Ω_{eff}. Lastly, Doppler frequencies can be converted into cross-ranges by making use of

$$\nu_k = -\frac{2f_0\Omega_{eff}}{c} c_k \tag{3.11}$$

with ν_k and c_k being the Doppler frequency and cross-range of the kth scatterer, respectively.

3.3.2.7 CLEAN

The dominant scatterers of the refocused signature are extracted by making use of the CLEAN technique [95]. After estimation of the PSF of the ISAR system, position and complex amplitude of each scatterer are retrieved, and their contribution is iteratively removed from the image.

3.3.3 Validation Methods

Diverse ground measurements were collected during both experiments in order to validate the derived products. Pictures of the illuminated area were taken by an optical camera installed on board the platform with a 2 s sample interval.

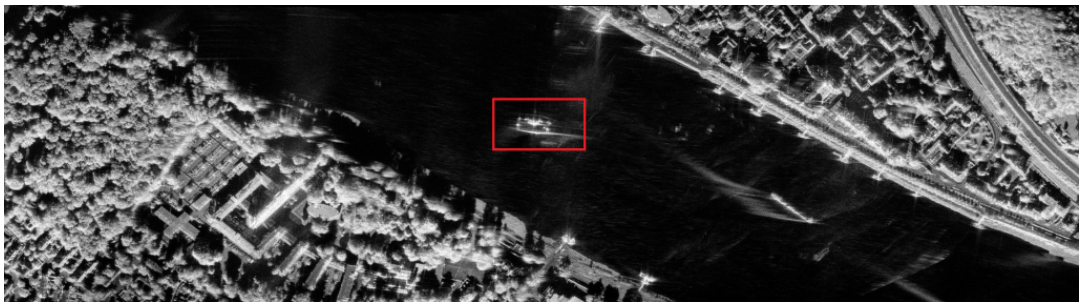

FIGURE 3.3: Experiment #1, exemplary SAR image: target of interest (red).

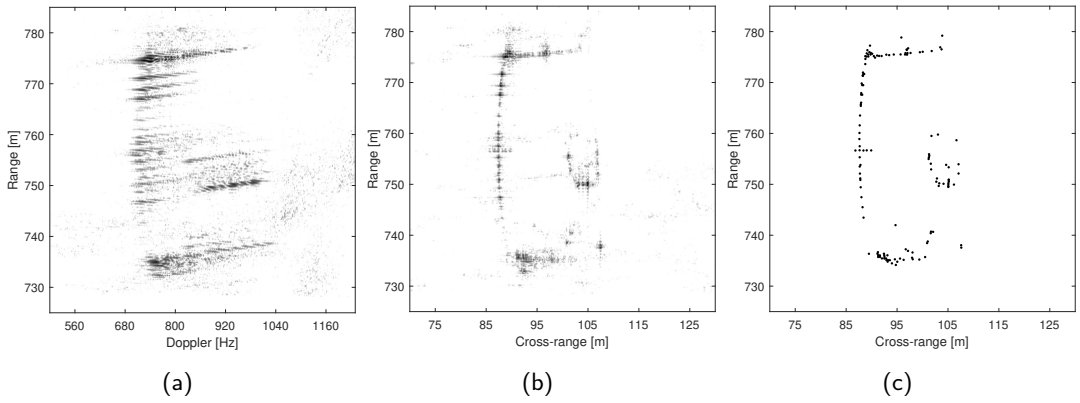

FIGURE 3.4: Experiment #1, exemplary data-take. (a) Range/Doppler image before refocusing. (b) Range/cross-range image after refocusing. (c) CLEAN image.

Moreover, both targets were equipped with differential GPS systems composed of a Trimble Zephyr 2 antenna and a Trimble R7 GNSS receiver. The estimated standard deviations of the GPS positions showed an approximately constant trend during the integration times, with values ranging between 0.026 m and 0.040 m according to the specific data-take and experiment. The recorded dynamics are used in order to obtain the *true* radial velocity and acceleration, therefore allowing for an accurate validation of the motion estimates. Furthermore, for Experiment #1, the derived main geometric features (e.g., length and width) are compared with the design values obtained from the ferry's construction project.

3.4 Results

3.4.1 Experiment #1

The exemplary SAR image depicted in Fig. 3.3 was fed to the implemented algorithm. The range/Doppler image of the target before refocusing is depicted in Fig. 3.4a. The autofocusing algorithm converges when using $(v_r, a_r) = (-3.32\,\mathrm{m\,s^{-1}}, 1.64\,\mathrm{m\,s^{-2}})$, thereby yielding the refocused image of Fig. 3.4b. The estimated motion parameters were then compared with the ones provided by

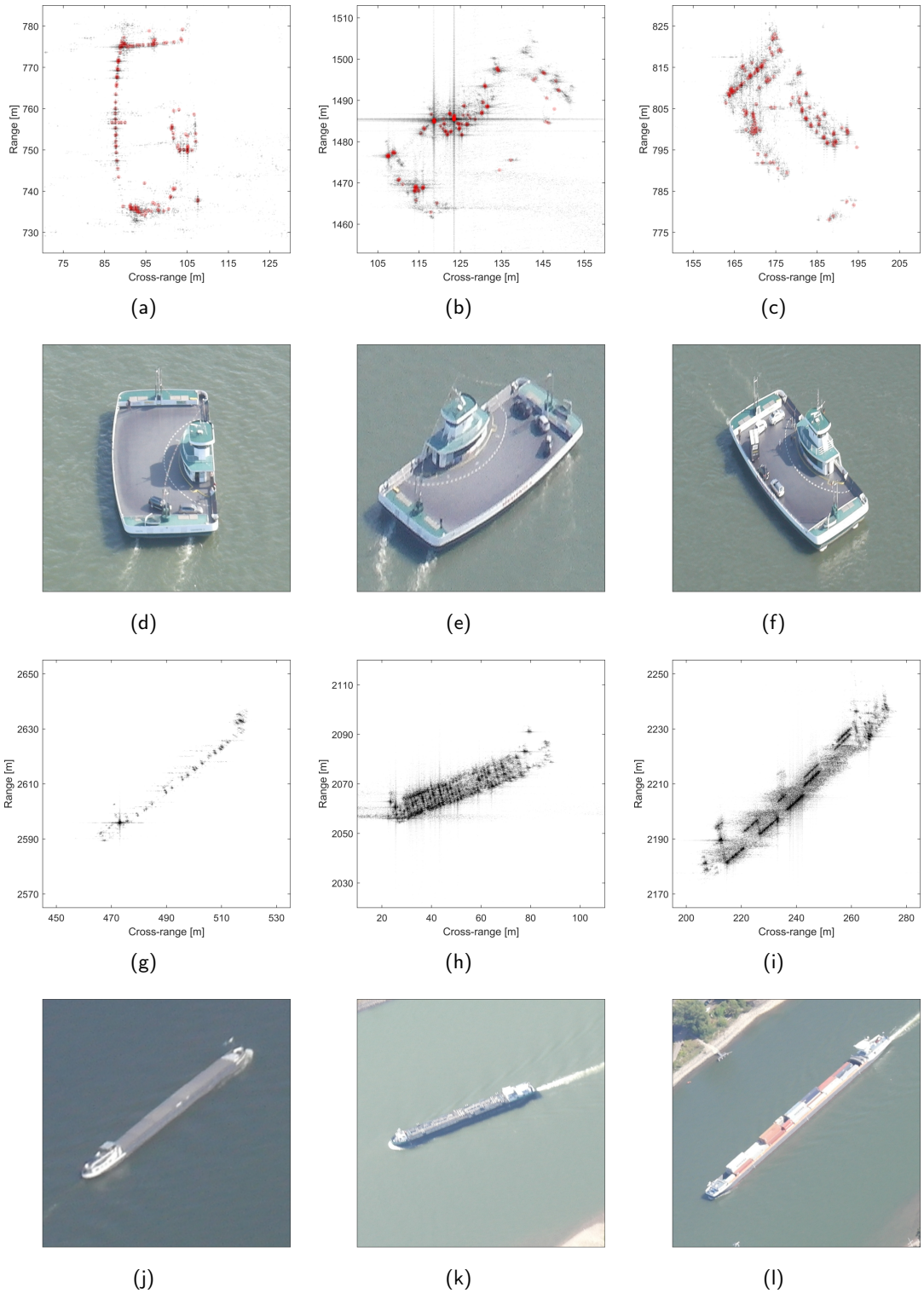

FIGURE 3.5: Experiment #1, data-take #1–3. (a–c) Target of interest; range/cross-range images after refocusing and CLEAN images (red). (d–f) Target of interest; optical images. (g–i) Targets of opportunity; range/cross-range images after refocusing. (j–l) Targets of opportunity; optical images.

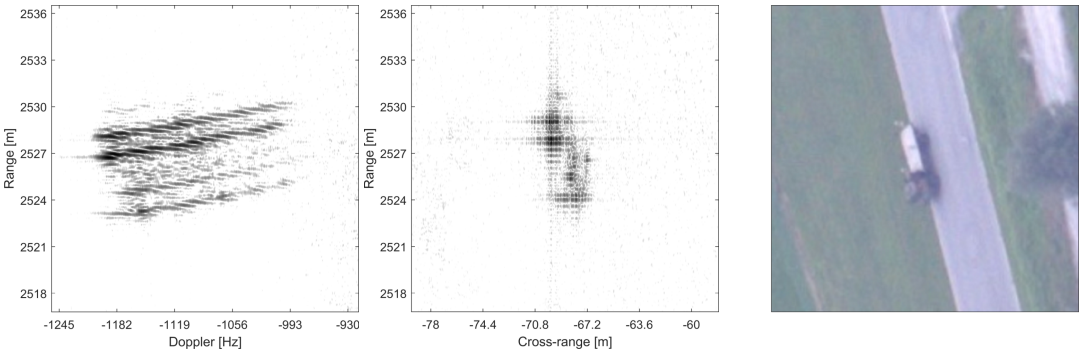

FIGURE 3.6: Experiment #2, data-take #1. (a) Range/Doppler image before refocusing. (b) Range/cross-range image after refocusing. (c) Optical image.

the GPSs, thus defining a percent error of $(1.78\,\%, 0.73\,\%)$. Lastly, the dominant scatterers of Fig. 3.4b were extracted by making use of the CLEAN technique, and were exploited to derive the target length L and width W. The SAR derived dimensions are $(44.55\,\mathrm{m}, 19.36\,\mathrm{m})$, thus defining a percent error of $(3.65\,\%, 3.63\,\%)$. The remaining data-takes were processed through the same procedure: the refocused images, superimposed with the extracted dominant scatterers, are depicted in Figs. 3.5a–3.5c, whereas the respective optical images are shown in Figs. 3.5d–3.5f. The retrieved parameters are summarized in Table 3.3: the mean value of the percent error is 2.37 % and 2.02 % for the radial velocity and acceleration, respectively, and 4.27 % for the target dimensions.

Additionally, targets of opportunity, for which no direct ground-truth measurements are available (neither motion parameters nor dimensions), were processed: the obtained refocused images are depicted in Figs. 3.5g–3.5i, and the respective optical images are shown in Figs. 3.5j–3.5l.

3.4.2 Experiment #2

The range/Doppler images before and after refocusing for an exemplary data-take are shown in Fig. 3.6a and Fig. 3.6b, respectively, whereas the corresponding optical image is shown in Fig. 3.6c. The best degree of focusing is obtained when using $(v_r, a_r) = (-2.64\,\mathrm{m\,s^{-1}}, 1.23\,\mathrm{m\,s^{-2}})$, thus defining a percent error of $(1.18\,\%, 3.23\,\%)$. The same procedure was then adopted to process the remaining data-takes, thus retrieving the estimates summarized in Table 3.4: the mean value of the percent error results to be 1.73 % and 2.19 % for the radial velocity and acceleration, respectively. As the data-takes were acquired under almost identical configurations, no substantial visual differences arise, thereby the refocused images of the remaining data-takes are not shown herein.

Data-take	#1	#2	#3
$(v_r,\, \epsilon_{v_r})$	$(-3.32,\, 1.78)$	$(-5.02,\, 2.67)$	$(-4.97,\, 2.65)$
$(a_r,\, \epsilon_{a_r})$	$(1.64,\, 0.73)$	$(0.96,\, 5.05)$	$(1.31,\, 0.28)$
$(\mathrm{L},\, \epsilon_l)$	$(44.55,\, 3.65)$	$(44.53,\, 3.70)$	$(43.03,\, 6.94)$
$(\mathrm{W},\, \epsilon_w)$	$(19.36,\, 3.63)$	$(19.18,\, 4.53)$	$(19.46,\, 3.14)$

* $[v_r] = \mathrm{m\,s^{-1}},\ [a_r] = \mathrm{m\,s^{-2}},\ [L] = \mathrm{m},\ [W] = \mathrm{m},\ [\epsilon] = \%$

TABLE 3.3: Results: Experiment #1

Data-take	#1	#2	#3
$(v_r,\, \epsilon_{v_r})$	$(-2.64,\, 1.18)$	$(-1.89,\, 2.98)$	$(-1.57,\, 1.02)$
$(a_r,\, \epsilon_{a_r})$	$(1.23,\, 3.23)$	$(0.66,\, 2.20)$	$(1.00,\, 1.13)$

* $[v_r] = \mathrm{m\,s^{-1}},\ [a_r] = \mathrm{m\,s^{-2}},\ [\epsilon] = \%$

TABLE 3.4: Results: Experiment #2

3.5 Discussion

3.5.1 Refocusing Algorithm

The performances obtained for Experiment #1 are summarized as follows. The percent error of the radial velocity ranges between 1.78 % and 2.67 %, and has a mean value of 2.37 %. As for the radial acceleration, its estimates yielded an error ranging between 0.28 % and 5.05 %, with a mean value of 2.02 %. The resulting refocused images (see Figs. 3.5a–3.5c) exhibit strong similarities with the corresponding optical images (see Figs. 3.5d–3.5f). Nonetheless, some structures that are clearly visible for one data-take (e.g., see the left contour of the ferry deck in Fig. 3.5a) are either barely detectable or even missing in the remaining ones. When interpreting and comparing the visual outputs of Figs. 3.5a–3.5c, it is worth bearing in mind that they were obtained under different conditions: not only crucial RADAR parameters such as PRF and bandwidth varies (see Table 3.1), but, more importantly, different illumination conditions (e.g., incidence angle, integration time, etc.) were experienced. A meaningful example is given by the signatures of the parked vehicles on the ferry deck, which clearly emerge from the white (low energy) floor only for data-take #3 (see Fig. 3.5c). The causes behind such behaviors are not easily traceable, and the explanations proposed herein are merely speculative. One plausible cause is given by the different acquisition geometries: for data-take #1–2, planar surfaces, such as the roof or the vehicles sides, reflect the electromagnetic energy away from the sensor, whereas only edges back-scatter a detectable signal.

All targets' signatures were mapped from the range/Doppler domain to the range/cross-range domain after estimation of Ω_{eff}. However, the accuracy of

such estimates, and thereby of the resulting dimensions, could be assessed only for the target of interest of Experiment #1. The percent error of the length (i.e., the dimension along the longer main axis) ranges between 3.65 % and 6.94 %, and has a mean value of 4.76 %. As for the width (i.e., the dimension of the ferry along its shorter main axis), its estimates yielded a percent error ranging between 3.14 % and 4.53 %, with a mean value of 3.77 %. For all available data-takes, both dimensions were always underestimated. The aforementioned values were obtained by exploiting the CLEAN images: the retrieved dominant scatterers were projected onto the axis of interest, and the pair defining the largest distance was used in order to define the estimate. When adopting such an approach, measurements from different data-takes are not completely coherent with each other as different pairs of dominant scatterers are used to estimate the same geometric feature. Nonetheless, though the images were acquired under completely different conditions, the estimates summarized in Table 3.3 are similar, thereby they represent a reliable indicator of the algorithm performances.

The RADAR and optical images of three additional targets are shown in Figs. 3.5g–3.5l, respectively. The amount of back-scattered energy is directly linked to the target characteristics: the deck surface depicted in Fig. 3.5j appears to be flat, and, as a consequence, most of the energy is reflected away from the sensor, thus producing an image with only few visible features (see Fig. 3.5g). On the other hand, Figs. 3.5k–3.5l present surfaces with complicated and edgy structures, thereby justifying the considerable amount of back-scattered energy (see Figs. 3.5h–3.5i).

Similar to Experiment #1, the GPS derived values were used to validate the estimates of Experiment #2. The percent error of the radial velocity ranges between 1.02 % and 2.98 %, and has a mean value of 1.73 %. The estimates of the radial acceleration, vice-versa, defined a percent error ranging between 1.13 % and 3.23 %, with a mean value of 2.19 %. Neither the front nor the rear of the truck are clearly imaged in Fig. 3.6b, thereby making the image interpretation more difficult. Nonetheless, the following remarks have to be taken into account. The largest ratio of back-scattered energy is due to the deployed corner reflectors. However, from a visual inspection of the resulting images, only the pair of reflectors installed in the vehicle's rear is clearly recognizable (see farther contributions in either Fig. 3.6a or Fig. 3.6b). Identifying the causes that lie behind such behaviors is a challenging task, and validating the findings is no longer possible. A likely explanation is given by an erroneous implementation of the experiment's set-up: during the SAR acquisition, and thus while the truck was moving, the reflectors might have shaken, thereby inducing centimeter scale range variations, which cannot be accurately described by the adopted range history model.

One limiting factor of the implemented algorithm is represented by the inability to handle low Signal-to-Noise-and-Clutter Ratio (SNCR) environments. The superimposition of clutter, in combination with the spreading of the target energy outside of the cropped sub-image, decreases the SCNR and affects the derived estimates. Nevertheless, such effects were minimized due to the adopted experiments' set-ups. In fact, all targets of Experiment #1 were imaged inside the Rhine river, which back-scatters a marginal amount of energy. On the other hand, for Experiment #2, ground-clutter competes with the signal of interest, though the use of corner reflectors makes the useful signal emerge from the stationary back-ground. In light of the above, it is safe to assume clutter to have a limited impact for the cases discussed herein, thus making unnecessary the use of clutter rejecting techniques. However, it remains an open question as to how the performance would degrade in case the aforementioned conditions were not experienced. Moreover, it should be noted that the range registration coordinate for moving targets in FMCW SAR data-sets is a function of both round-trip delay *and* Doppler frequency. This, in turn, translates into an invalid range measurement, thereby affecting the estimates of the motion parameters obtained from the range-compressed signal. However, for the examples shown herein, the undesired contribution affecting the radial velocity estimates in Table 3.3 and 3.4 reaches values up to $2\,\mathrm{cm\,s^{-1}}$, and it is therefore considered negligible. Lastly, it is worth highlighting that the implemented method is designed on the assumption of using short integration times (i.e., of the order of 1 s). Within such a time span, the effective rotation vector is approximately constant and the range Doppler technique is successful. However, when longer integration times are needed to maximize the azimuth resolution, or when the target undergoes exceptionally strong angular motions, the adopted imaging method is no longer optimum and other solutions are necessary [96].

3.5.2 Summary and Outlook

This paper has proven the capabilities of FMCW Ka-band data-sets for RADAR imaging purposes. The authors combined a number of state-of-the-art techniques to produce high resolution images of moving targets. The main core of the implemented algorithm is represented by the range Doppler technique which, in combination with autofocusing, allows to produce RADAR images with high resolution. Though the deployed method consists of well-known techniques, the authors believe that the results shown herein are of particular importance. Firstly, although the demand for low-cost and compact imaging systems has increased over the last few years, only few publications have dealt with the imaging of moving targets in FMCW SAR environments. Moreover, Ka-band data-sets have rarely been used for moving targets imaging, and the resulting

products (e.g., images, derived motion parameters and geometric features) have never been validated as thoroughly as in the current work. The choice of the band is crucial in determining the system performances: for a given variation of the viewing angle, shorter wavelengths – or, equivalently, higher frequencies – allows to obtain a better cross-range resolution. Lastly, assessing whether ultra-light-weight airborne platforms are capable of guaranteeing satisfying performances is a question which needs to be addressed as the current technological advances push for the exploitation of even lighter platforms. However, such carriers usually present an unstable motion: for the data-takes discussed herein, the standard deviations of the angular motions result to be at least an order of magnitude larger than that for heavier carriers (e.g., the Transall C-160).

The implemented method has been tested and its performances have been precisely assessed: the motion estimates were validated by making use of ground measurements, whereas the retrieved target dimensions were compared with the design values obtained from the target construction project. Both motion and geometric estimates resulted to produce marginal percent errors, thereby validating the implemented algorithm and verifying the usefulness of the data-sets.

Future researches shall focus on designing imaging algorithms which can successfully process millimeter-wave data-sets acquired by SAR sensors mounted on board ultra-light-weight, or even lighter, airborne platforms. As MoComp plays a crucial role in defining the final degree of focusing, especially when exploiting shorter wavelengths, particular attention shall be paid to designing algorithms which are not constrained to simplified range history models. Moreover, choosing whether to use time or frequency domain processors is not trivial, as the latter appear to be not sufficiently flexible to handle strongly non-linear flight-paths. The use of a lighter platform, and thereby of a more compact system, might dictate physical design constraints that prevent from exploiting multiple channels, thus making it impossible to implement efficient clutter rejecting techniques. In light of the above, it is of interest to quantify the minimum SCNR that still allows for an acceptable degree of focusing, and how the accuracy of the derived estimates degrade as a function of the SCNR. Moreover, particular attention shall be paid to assessing how the target angular motions affect the final products, and to modifying the implemented method for it to be capable of handling longer integration times. Alternatively, it is also of interest to study the feasibility of merging either coherently or incoherently a sequence of ISAR images after mapping them into a common reference frame.

Chapter 4

Multi-View Three-Dimensional Radar Imaging of Moving Targets with Time-Domain Processing

Emiliano Casalini, Elías Méndez Domínguez and Daniel Henke

This chapter is based on an article submitted to the peer-reviewed IEEE Transactions on Geoscience and Remote Sensing in 2021. The article was submitted under the title "Multi-View Three-Dimensional Radar Imaging of Moving Targets with Time-Domain Processing."

E. Casalini and D. Henke conceptualized the study. E. Casalini and E. M. Domínguez elaborated the methodology. E. Casalini performed the analysis and interpreted the results. E. M. Domínguez and D. Henke contributed to the analysis and the interpretation of the results. E. Casalini and E. M. Domínguez wrote the first draft of the manuscript. E. Casalini, E. M. Domínguez and D. Henke participated in the writing and editing of the final manuscript.

4.1 Abstract

Conventional SAR processing can be adapted to obtain Two-dimensional (2-D) high-resolution images of moving targets. The resulting images, however, suffer from layover effects, therefore making their interpretation more challenging. This problem can be dealt with by combining RADAR imaging with interferometry, which allows for Three-dimensional (3-D) target reconstruction. This article presents a 3-D imaging technique built upon the well-known Global Backprojection (GBP) algorithm, which has been adapted to focus moving targets rather than the stationary scene. The proposed algorithm is tested on real data-sets acquired with a circular acquisition geometry. Using a non-linear flight-path allows to monitor the target from multiple viewing angles, therefore overcoming the limitations that are common to stripmap SAR (e.g., shadowing effects, geometrically adverse cases, etc.). The obtained results, which were compared with independent ground measurements, demonstrate the accuracy of the proposed method.

4.2 Introduction

SAR systems are popular RS solutions for earth surface monitoring in all-weather and all-light conditions. Such systems are usually mounted onto airborne or spaceborne platforms, and move along a desired trajectory while radiating electromagnetic waves towards the ground [32]. SAR processing converts the recorded signal into a high-resolution RADAR image, which can then be used for numerous applications. Important among these are maritime applications, such as the monitoring of shipping routes, surveillance of coastal areas, border control, etc. [87, 97]. Conventional SAR processing was primarily designed to compensate only for the relative motion between sensor and ground. As a consequence, stationary targets (e.g., streets, buildings, parked vehicles, etc.) are correctly imaged whereas moving targets are defocused and displaced from their real position [39, 40]. Oftentimes, the moving target signal is so spread that it is challenging to extract any useful information, thus making it meaningless for applications such as target recognition and classification.

The problem of moving target refocusing has been extensively treated, and many different methods are nowadays available in the literature [45,46,49,66,89]. Jao [49] identifies the moving target response in the SAR image and derives its corresponding spectrum, which is then used to perform matched filtering. Similarly, Zhu *et al.* [89] propose a two-dimensional matched filtering that can successfully compensate for the range cell migration without *a-priori* knowledge of the accurate motion parameters. Alternatively, SAR processors can be modified in order to match the moving target signal. In [45], Cristallini *et al.* achieve

this through a bank of chirp scaling algorithm-based filters, each one tuned to a different relative azimuth velocity. Moreover, in [46] and [66], the authors suggest the use of the so-called normalized relative speed to refocus moving targets in both pulsed and frequency-modulated continuous-wave SAR images. Though the aforementioned algorithms produce reasonably good results, they are unable to automatically estimate the motion parameters, therefore having to rely on computationally burdening solutions. This can be prevented by using autofocus algorithms [53, 98–100]. Martorella *et al.* [53] model the target range history via a finite-order polynomial, and estimate its coefficients by maximizing the contrast of the target range-Doppler image. In a similar fashion, Noviello *et al.* [98] compensate for the target motion by automatically estimating the target Doppler parameters. The backprojection autofocus algorithm was first introduced in [99], and later on extended in [100]: Sommer *et al.* decompose the target image into sub-images, and implement a pulse-by-pulse phase correction at sub-image level. Despite these algorithms are designed to tackle the same problem, they are intrinsically different. The methods in [53, 98] work in the frequency-domain, and provide good results when dealing with short observation times. On the other hand, the algorithm in [100] operates in the time-domain, and can utilize data-sets with longer observation times.

Regardless of how well moving targets are refocused, 2-D images are difficult to interpret due to the projection of a 3-D object on the imaging plane. State-of-the-art techniques for 3-D moving target reconstruction combine ISAR images acquired by multiple receiving channels, therefore introducing the concept of InISAR [62–65, 101]. Wang *et al.* [62] propose a system that uses three receiving channels arranged in two orthogonal baselines. Similarly, in [101], Xu *et al.* use a pair of antennae located at different altitudes in order to produce the 3-D target image. Given *et al.* [63] provide the basis for a generalized ISAR algorithm specifically designed for imaging large vessels. Martorella *et al.* [64] present the theoretical foundations for 3-D InISAR imaging. The authors pay special attention to estimating the so-called effective rotation vector, which univocally identifies the imaging plane. Lastly, in [65], Salvetti *et al.* show how 3-D target reconstruction largely benefits from merging information acquired from different sensors. The solutions proposed in [64, 65] are computationally efficient as the reconstruction process is performed on a limited number of bright scattering points. However, the algorithm performances are directly linked to how accurately the imaging plane is determined. Hence, even small errors in estimating the effective rotation vector might translate into unreliable height estimates.

In this article, we propose an algorithm to derive a 3-D image, or point cloud, of a moving target using single-pass interferometric SAR data acquired with an arbitrary flight-path. The proposed algorithm combines a well-known

frequency-domain-based autofocus method [53] with the GBP algorithm [102]. The former is computationally efficient and capable of retrieving reliable motion estimates directly from raw data-sets. However, the resulting images are usually expressed in the non-homogeneous range-Doppler domain, thus requiring a mandatory scaling step [94]. This is not an issue when using the GBP algorithm, as the focused images are naturally expressed in homogeneous coordinates. Therefore, the estimation of the imaging plane is no longer necessary, and the accuracy of the height estimates depends only on the reliability of the interferometric phase.

Finally, it is worth highlighting that the data-sets presented herein are of particular interest as they were acquired with a Circular SAR (CSAR) acquisition geometry. Such acquisition mode allows the target to be observed over a long period and from different viewing angles, thereby easing its detection and increasing the amount of information that can be extracted [103]. Time-domain processors, due to their specific design, are more suitable for handling strongly non-linear flight-paths [104], and they can provide better image quality than frequency-domain processors. Nonetheless, while much effort has been devoted to deriving autofocus algorithm in the time-domain [99, 100], almost no attention has been paid to assessing whether they can be used to implement 3-D moving target reconstruction.

The remainder of this article is organized as follows. Section 4.3.1 introduces the F-SAR sensor and its specifications, and describes the experimental set-up. Section 4.3.2 reviews the well-known GBP algorithm. The proposed method is thoroughly described in Section 4.3.3, whereas the available ground measurements are listed in Section 4.3.4. Experimental results, obtained by processing real data-sets, are summarized in Section 4.4. Finally, a detailed analysis of the results and potential research directions are given in Section 4.5.

4.3 Method

4.3.1 Sensor and Experimental Set-up

The F-SAR sensor is an airborne multi-frequency pulsed-SAR sensor designed by the German Aerospace Center (DLR) [105]. For our experiment, we used X-band in combination with a 384 MHz range bandwidth, which translates into a nominal resolution of circa 39 cm. Moreover, the system features single-pass interferometric SAR capabilities, as two receiving channels are arranged in a cross-track baseline. The main system parameters are summarized in Table 4.1.

The experiment was conducted on the 28th of June 2019, and took place on Lake Constance, between the cities of Constance and *Meersburg*, Germany.

Parameter	Value
Carrier frequency [GHz]	9.6
Bandwidth [MHz]	384
PRF [kHz]	1.25
Mid-swath slant-range [m]	6245.56
Swath width [m]	4219.45
Cross-track baseline [m]	1.67
Azimuth beam-width [deg]	7.58
Off-Nadir angle [deg]	50

TABLE 4.1: System Parameters

FIGURE 4.1: Google Earth image of the Lake Constance test-site: sensor flight-path (red), and target path (yellow).

The aim of the experiment was to record the activities of the vessels on the lake. The airborne platform, the DLR Dornier 228 research aircraft, flew at an altitude of 4331 m with a speed of $85\,\mathrm{m\,s^{-1}}$, and drew two subsequent circular trajectories with a 4074 m radius. In order to maximize the chances of observing moving targets, the acquisition geometry was designed so that the antenna would illuminate a highly trafficked area. In this portion of the lake, which connects Constance with Meersburg, a fleet of six different-sized ferries, transporting passengers and private vehicles, is continuously underway. The acquisition geometry and the test-site are depicted in Fig. 4.1.

4.3.2 GBP Algorithm

In this section, we briefly review how to focus the signal back-scattered from a point-like stationary target. In the equations, we neglect the operations that do not impact the focusing of the SAR image (e.g, calibration factors, signal weightings, etc.). Let the band-pass range-compressed signal be referred to as $s(\cdot)$ (i.e., after matched filtering, up-sampling and signal band-pass conversion), whereas the discrete slow time variable is identified by τ. The GBP algorithm achieves focusing by projecting a sequence of range-compressed signals onto a desired grid, typically a Digital Terrain Model (DTM) of the illuminated area. This can be expressed as

$$\gamma_0(x, y, h_0) = \sum_{\tau=-\frac{T}{2}}^{+\frac{T}{2}} s\left[\frac{2R(\tau)}{c}\right] \cdot \exp\left[j \cdot \frac{2\pi f_c}{c} \cdot 2R(\tau)\right] \tag{4.1}$$

with c and f_c representing the speed of light and the carrier frequency, respectively. Within the aperture integration, defined by the minimum and maximum slow time $\pm\frac{T}{2}$, the platform motion induces a slant-range variation $R(\cdot)$ between the sensor and the point of interest. The latter is located at coordinates

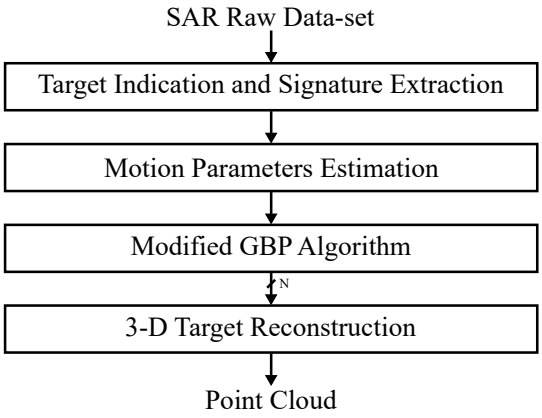

FIGURE 4.2: Block diagram of the implemented algorithm.

(x, y, h_0), with h_0 being the height. The exponential term in (4.1) compensates for the slow time-dependent phase rotation produced by the round-trip delay, thus allowing for coherent integration of the recorded samples. The antenna phase center position is assumed to be known with sub-wavelength accuracy in order to achieve the nominal resolution and to reduce targets defocusing. The resulting image $\gamma_0(\cdot)$ represents the non-calibrated reflectivity of the scene.

4.3.3 Moving Target Imaging

4.3.3.1 Overview of the Processing Chain

The main steps of the implemented algorithm are summarized in Fig. 4.2. The input consists of a SAR raw data-set, which is mapped from the original slow time-domain into the Doppler frequency-domain through a Fourier transform. Then, moving targets are indicated by using any of the available detectors designed in the range-Doppler domain. The resulting image is fed to a state-of-the-art autofocus algorithm to retrieve accurate estimates of the motion parameters, as described in Section 4.3.3.2. Consequently, in Section 4.3.3.3, the GBP algorithm is modified on the basis of the previously obtained estimates, producing a refocused image in map geometry. For 3-D target reconstruction, the previous step is iterated a number of times for each available receiving channel. The resulting 3-D cubes are further processed to obtain the target point cloud, according to the procedures in Section 4.3.3.4.

4.3.3.2 Motion Parameters Estimation

Autofocus algorithms are designed with the objective of retrieving the moving target motion parameters directly from the received signal. Such techniques are usually subdivided into two different categories: parametric and non-parametric [92]. The results presented herein were obtained by using the image contrast based technique [53], a parametric technique that models the range history via

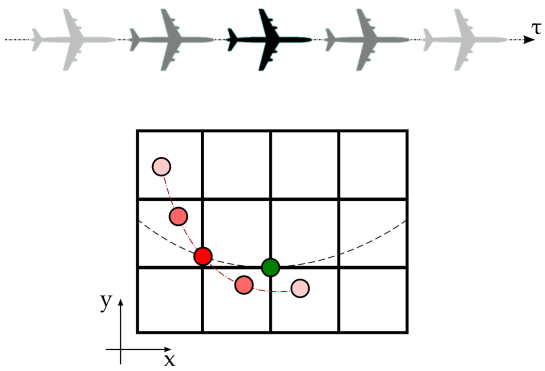

FIGURE 4.3: Top-view of the simplified geometry: point-like stationary target (green circle), iso-range line at central time instant $\tau = 0$ (black dashed line), point-like moving target (red circles) and corresponding trajectory (red dashed line).

a finite-order polynomial. Let the slant-range variation with respect to the central time instant $\tau = 0$ be referred to as $\delta R'(\cdot)$. This can be approximated as

$$\delta R'(\tau) = \sum_{n=1}^{\infty} \frac{a_n \tau^n}{n!} \approx \delta \tilde{R}'(\tau) = \sum_{n=1}^{N} \frac{\tilde{a}_n \tau^n}{n!} \tag{4.2}$$

with N and a_n being the polynomial degree and the polynomial coefficient, respectively. The order N depends on multiple factors, the most important being how *smooth* the slant-range variation is within the observation time. When the desired cross-range resolution is of the order of the meter, or worse, and for reasonably regular relative motions, three coefficients (i.e., the radial velocity, acceleration and jerk) describe the range history with sufficient accuracy.

The estimation of the polynomial coefficients a_n is designed as follows. First, the Radon transform is used to obtain an initial estimate of the motion parameters. Then, the estimate is refined through a semi-exhaustive search, and the best solution is derived based on the contrast values of the resulting images. Last, the estimate is further refined by solving an optimisation problem: similarly to the previous step, the function to be maximised is directly linked to the image contrast. For a more detailed explanation of the method, please refer to [53].

4.3.3.3 Modified GBP Algorithm

Let the vector describing the position of the antenna phase center and of a point-like moving target be referred to as $\boldsymbol{P_S}(\tau)$ and $\boldsymbol{P}'(\tau)$, respectively. Moreover, let us assume that the resulting relative motion is such that the moving target is registered at coordinates $\boldsymbol{P}$ at $\tau = 0$, as depicted in Fig. 4.3. The corresponding range histories can be computed as follows:

$$R(\tau) = \|\boldsymbol{P_S}(\tau) - \boldsymbol{P}\| = R(0) + \delta R(\tau) \tag{4.3}$$

$$R'(\tau) = \|\boldsymbol{P_S}(\tau) - \boldsymbol{P'}(\tau)\| = R(0) + \delta R'(\tau) \tag{4.4}$$

with $\|\cdot\|$ being the Euclidean norm operator. By replacing (4.2) into (4.4), the difference between the two range histories can be expressed as follows:

$$\Delta(\tau) = R(\tau) - R'(\tau) \approx \delta R(\tau) - \sum_{n=1}^{N} \frac{\tilde{a}_n \tau^n}{n!} \tag{4.5}$$

Assuming that the degree N has been correctly chosen, and that the estimates $\tilde{a}_n$ are accurate enough, $\Delta(\cdot)$ represents the residual slant-range variation which is responsible for moving target defocusing. This contribution can be compensated for in the GBP algorithm by modifying the sensor position on the basis of $\Delta(\cdot)$.

Let the unit vector identifying the line-of-sight between the sensor position and the target registration coordinates $\boldsymbol{P}$ be referred to as $\boldsymbol{i}(\cdot)$. This is computed as follows:

$$\boldsymbol{i}(\tau) = \frac{\boldsymbol{P_S}(\tau) - \boldsymbol{P}}{R(\tau)} \tag{4.6}$$

Hence, the fictitious sensor position $\boldsymbol{P'_S}(\tau)$ is derived from (4.5) and (4.6), and can be written as

$$\boldsymbol{P'_S}(\tau) = \boldsymbol{P_S}(\tau) - \Delta(\tau) \cdot \boldsymbol{i}(\tau) \tag{4.7}$$

Thus, when replacing $\boldsymbol{P_S}(\tau)$ with $\boldsymbol{P'_S}(\tau)$ in the GBP algorithm, the resulting image can be expressed as

$$\gamma'_0(x, y, h_0) \approx \sum_{\tau=-\frac{T}{2}}^{+\frac{T}{2}} s\left[\frac{2R'(\tau)}{c}\right] \cdot \exp\left[j \cdot \frac{2\pi f_c}{c} \cdot 2R'(\tau)\right] \tag{4.8}$$

where the approximation sign is a consequence of using the finite-order polynomial (4.2). When the error caused by this approximation is negligible, $\gamma'_0(\cdot)$ represents the non-calibrated reflectivity function of the point-like moving target.

4.3.3.4 3-D Reconstruction

The height information can be derived by means of interferometric SAR datasets acquired with $K-1$ baselines. Let us assume that a point-like moving target is lying on a plane at height $h_i \neq h_0$. When using (4.8), the resulting image exhibits a sub-optimal degree of focusing since the signal has been projected onto a grid at the wrong height h_0. However, this problem can be easily tackled by using a grid at the correct height h_i. The newly obtained image is indicated with $\gamma'_{k,i}(\cdot)$, where the indexes k and i identify the receiving channel and the grid layer, respectively. Hence, the signal impinging on the antenna array can

be expressed as

$$\boldsymbol{y} = [\gamma'_{1,i}(x, y, h_i), \ldots, \gamma'_{K,i}(x, y, h_i)]^T = \boldsymbol{M}\boldsymbol{x} + \boldsymbol{\epsilon} \tag{4.9}$$

with $\boldsymbol{x}$ and $\boldsymbol{\epsilon}$ being vectors of size $L \times 1$ representing the unknown reflectivity vector and noise, respectively. The matrix $\boldsymbol{M}$ has size $K \times L$ and contains the steering vectors in its columns. The l-th steering vector can be written as follows:

$$\boldsymbol{m}_l = \left\{1, \exp\left[j \cdot \phi(2, l)\right], \ldots, \exp\left[j \cdot \phi(K, l)\right]\right\}^T \tag{4.10}$$

where

$$\phi(k, l) = -\frac{2\pi f_c}{c} \cdot 2 \cdot \left[R'_S(k, l) - R'_S(1, l)\right] \tag{4.11}$$

with $R'_S(\cdot)$ being the slant-range of minimum approach.

Multiple studies are available in the literature as to how to retrieve the 3-D information of a target [106, 107]. In this work, we adopted the Maximum Likelihood Estimator (MLE) [108]. This method performs a multi-dimensional search to derive the elevation and amplitude of the layovered scatterers within each resolution ground cell. MLE provides Digital Surface Models (DSMs) with a height accuracy comparable to that of compressive sensing-based approaches, and with less outliers [109]. However, its computational complexity makes it impractical for use with data acquired from a large number of baselines [110]. For this reason, we applied a single-dimensional search-based MLE operating in a similar fashion to MUSIC [111–113]. The height information of each scatterer, the DSM, is computed by applying MLE to all the images $\gamma'_{k,i}(\cdot)$ of the 3-D grid. Although this increases the computational time, the coherence matrices can be obtained for each height level. This approach provides the DSMs that better resemble those acquired by airborne laser scanning sensors [109].

With MLE, the power of the compressed signals in elevation can be expressed as

$$\boldsymbol{x_{MLE}}(x, y, h_i) = e^{-\boldsymbol{m}^H(h_i)\hat{\boldsymbol{\Gamma}}_i^{-1}\boldsymbol{m}(h_i)} \tag{4.12}$$

where $\boldsymbol{m}(h_i)$ is the steering vector for the coordinates (x, y, h_i), and $\hat{\boldsymbol{\Gamma}}_i$ is the sample coherence matrix at height h_i. The elements of the coherence matrix are derived from those of the covariance matrix [108,109]. To compute the latter, we performed a multi-looking operation to reduce outliers caused by phase noise. The covariance matrix of the received signal at coordinates (x, y, h_i) is given by

$$\hat{\boldsymbol{C}} = \frac{1}{L_k}\sum_{n=1}^{N}(\boldsymbol{y}_n\boldsymbol{y}_n^H) \tag{4.13}$$

where $\boldsymbol{y}_n$ is the n-th look and N is the number of looks.

Maxima detection is applied to the output power resulting from (4.12). For

each ground cell (x, y), we retain the 3-D coordinates (x, y, h_i) of the n_s largest peaks in $\boldsymbol{x_{MLE}}(\boldsymbol{n}(x, y))$, with n_s being the number of layovered scatterer that can be unambiguously resolved. The unit vector $\boldsymbol{n}(\cdot)$ identifies the normal line for the ground cell of interest, and it is computed as in [109]. After applying maxima detection, we obtain a 3-D image of the target, where an empty voxel implies the absence of a scatterer.

4.3.4 Validation Methods

One of the operating ferries was equipped with a differential GPS, composed of a Trimble Zephyr 2 antenna and a Trimble R7 GNSS receiver. The recorded data were used in order to recognize the target of interest in the SAR data-sets, and to derive the *true* motion parameters, thus making it possible to validate the obtained estimates. Furthermore, the derived 3-D reconstructions were compared with the corresponding designs, which provide the ferry's main geometric features (i.e., length, width and height) and the front-, side- and top-view. Due to the lack of available 3-D computer-aided designs of the targets of interest, a thorough validation of the obtained point clouds could not be performed.

4.4 Results

The data-sets acquired from the two circular acquisitions were subdivided into a number of partially overlapping sub-apertures. The sub-aperture length and the overlapping time period were set equal to 3 s and 0.5 s, respectively, therefore defining more than 600 sub-apertures per acquisition. During the acquisitions, two ferries, from now on referred to as Target #1 and Target #2, were illuminated. The results for both targets were obtained by using a DTM of size $130\,\mathrm{m} \times 130\,\mathrm{m} \times 20\,\mathrm{m}$, and with pixel spacing 10 cm. The grid size was designed on the basis of *a-priori* knowledge of the target dimensions, whereas the pixel spacing was set slightly smaller than the RADAR range resolution to avoid aliasing.

The obtained results for Target #1 are summarized in Figs. 4.4–4.5. The six refocused images with the highest contrast are depicted in Figs. 4.4a–4.4f. Each of these images were further processed in order to reconstruct the 3-D shape of the moving target. Hence, the obtained point clouds were rotated in order to align the target longitudinal axis with the x-axis, thus yielding the results of Figs. 4.4g–4.4x. The final point cloud, the result of the fusion of the six different sub-apertures, and the corresponding optical image, are depicted in Fig. 4.5. The SAR-derived estimates of the length L, width W and

Parameter	$(\hat{L}, \epsilon_L)$	$(\hat{W}, \epsilon_W)$	$(\hat{H}, \epsilon_H)$
Sub-aperture #1	(68.27, 0.39)	(13.68, 2.06)	(11.90, 3.48)
Sub-aperture #2	(63.41, 6.74)	(13.59, 1.45)	(9.30, 19.13)
Sub-aperture #3	(67.71, 0.42)	(13.68, 2.09)	(12.20, 6.09)
Sub-aperture #4	(64.96, 4.47)	(13.57, 1.29)	(12.10, 5.22)
Sub-aperture #5	(65.46, 3.74)	(13.47, 0.49)	(9.40, 18.26)
Sub-aperture #6	(67.53, 0.69)	(13.56, 1.17)	(12.10, 5.22)
Fusion	(68.62, 0.91)	(13.72, 2.38)	(12.20, 6.09)

* $[\hat{L}] = \text{m},\ [\hat{W}] = \text{m},\ [\hat{H}] = \text{m},\ [\epsilon] = \%$

TABLE 4.2: Results: Target #1

Parameter	$(\hat{L}, \epsilon_L)$	$(\hat{W}, \epsilon_W)$	$(\hat{H}, \epsilon_H)$
Sub-aperture #1	(78.20, 5.06)	(13.26, 1.01)	(10.60, 1.45)
Sub-aperture #2	(77.87, 5.46)	(13.55, 1.13)	(11.40, 5.99)
Sub-aperture #3	(78.90, 4.22)	(13.71, 2.29)	(10.90, 1.34)
Sub-aperture #4	(80.96, 1.72)	(13.65, 1.90)	(11.50, 6.92)
Sub-aperture #5	(82.29, 0.10)	(13.68, 2.09)	(11.20, 4.13)
Sub-aperture #6	(79.69, 3.25)	(13.59, 1.45)	(11.10, 3.20)
Fusion	(82.29, 0.10)	(13.71, 2.33)	(11.50, 6.92)

* $[\hat{L}] = \text{m},\ [\hat{W}] = \text{m},\ [\hat{H}] = \text{m},\ [\epsilon] = \%$

TABLE 4.3: Results: Target #2

height H were computed as the distance between the two most distant scatterers along the x-, y- and z-coordinate, respectively. The retrieved estimates were compared with the values from the ferry design, thus resulting in the percent errors ϵ summarized in Table 4.2. When considering only the point clouds derived from the single sub-apertures, the percent errors range between $(0.39\,\%, 0.49\,\%, 3.48\,\%)$ and $(6.74\,\%, 2.09\,\%, 19.13\,\%)$, and the resulting mean errors are $(2.74\,\%, 1.43\,\%, 9.57\,\%)$. After fusion of the six sub-apertures, the final point cloud exhibits an error of $(0.91\,\%, 2.38\,\%, 6.09\,\%)$.

The same procedure was adopted for Target #2. The refocused images and the corresponding point clouds are depicted in Figs. 4.6a–4.6f and Figs. 4.6g–4.6x, respectively, whereas the final point cloud, together with the target optical image, is shown in Fig. 4.7. The percent errors of the derived dimensions are summarized in Table 4.2. The minimum and maximum values range between $(0.10\,\%, 1.01\,\%, 1.34\,\%)$ and $(5.46\,\%, 2.29\,\%, 6.92\,\%)$, respectively, and the resulting mean errors are $(3.30\,\%, 1.65\,\%, 3.84\,\%)$. The final point cloud exhibits an error of $(0.10\,\%, 2.33\,\%, 6.92\,\%)$.

To assess the accuracy of the derived point clouds, the latter were superimposed onto the designs, as depicted in Fig. 4.8.

Furthermore, with the main purpose of showing how the quality of the algorithm products changes through the circular acquisition, additional images of Target #2 are shown in Fig. 4.9. The sub-apertures mid-positions are highlighted with diamond markers in Fig. 4.10. The marker color codes the azimuth angle: values equal to 0 or 180 deg (i.e., the sensor and target trajectories are parallel) are represented in red, whereas values equal to 90 deg are represented in green. The azimuth angles for the sub-apertures of Fig. 4.9 are 64.94, 120.06 and 178.60 deg, respectively. The refocused image in Fig. 4.9c clearly exhibits a much lower quality.

4.5 Discussion

4.5.1 Algorithm Performances

The results of the numerical evaluation (see Tables 4.2–4.3) show that the retrieved dimensions of the targets are consistent with the values provided in the original designs. Moreover, the final point clouds (see Fig. 4.5a and Fig. 4.7a) exhibit strong similarities with the corresponding optical images (see Fig. 4.5e and Fig. 4.7e). This is further evidenced in Fig. 4.8, which shows that the large majority of detections fall within the outer contours of the targets.

Both targets are so-called double-ended ferries: they are symmetric about center-line and about midships, and have a broad vehicle deck with rounded ends. The open areas at the extremities of the vehicle deck are accurately represented by the blue-colored detections of Figs. 4.5a–4.5d and Figs. 4.7a–4.7d. The main differences between the two targets lie in the geometry of the upper passenger deck. For Target #1, the deck extremities are open and have a rounded shape; moreover, the pilothouses are located above the passenger deck. The red-colored detections of Figs. 4.5a–4.5d are likely caused by the signal back-scattered from the pilothouses and, as expected, they are located along the vessel center-line (see Fig. 4.5b and Fig. 4.5d). On the other hand, for Target #2, the passenger deck exhibits an oval shape and, more importantly, the pilothouses are located at the same level. In this case, the points with brighter colors of Fig. 4.7b define an oval-shaped area, presumably linked to the roof of the passenger deck. Moreover, the side-views of Figs. 4.7c–4.7d indicate that the roof of the upper deck is roughly flat, and that, unlike Target #1, the pilothouses are located at the same level.

The main similarity between the products of the two targets resides in the height-dependent nature of the derived detections. Visual inspection of the products reveals that the large majority of detections are close to ground level,

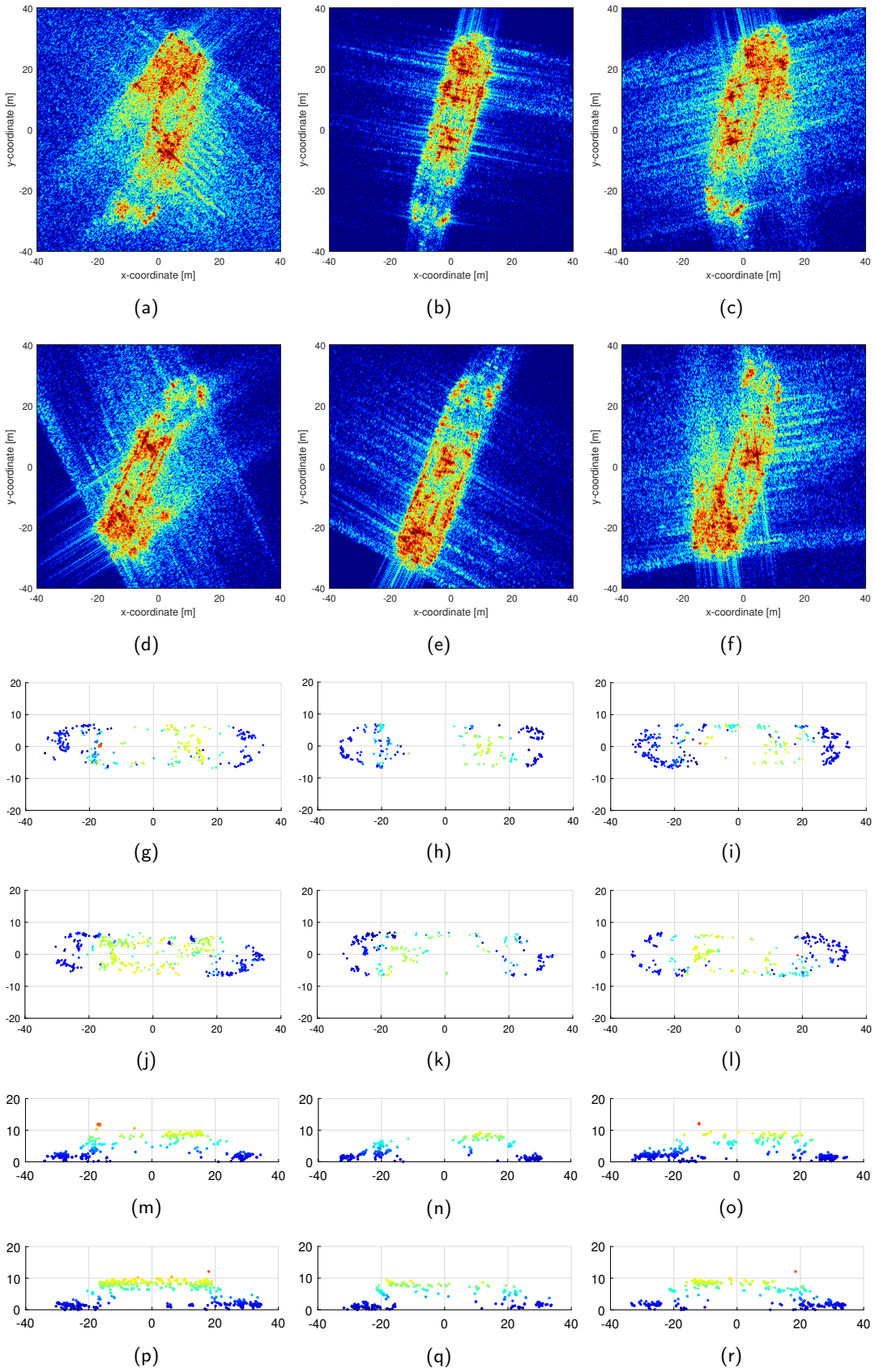
y-coordinate [m]
x-coordinate [m]
(a)
(b)
(c)
(d)
(e)
(f)
(g)
(h)
(i)
(j)
(k)
(l)
(m)
(n)
(o)
(p)
(q)
(r)

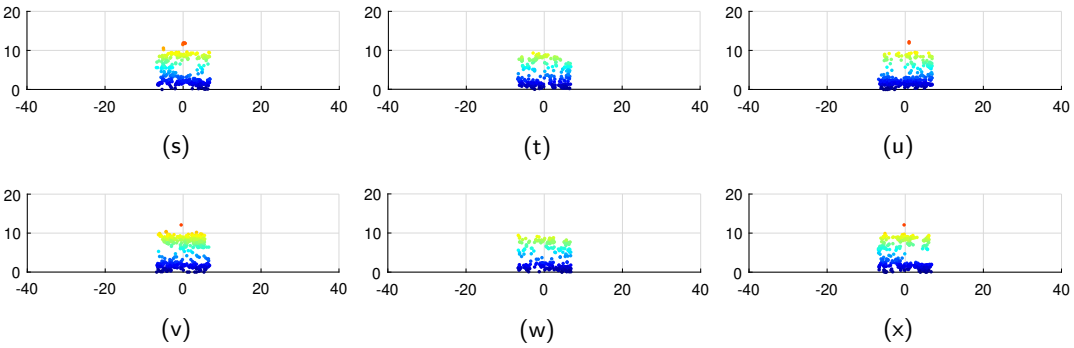

FIGURE 4.4: Target #1. (a–f) Refocused images. Point clouds: (g–l) x-y plane, (m–r) x-z plane and (s–x) y-z plane.

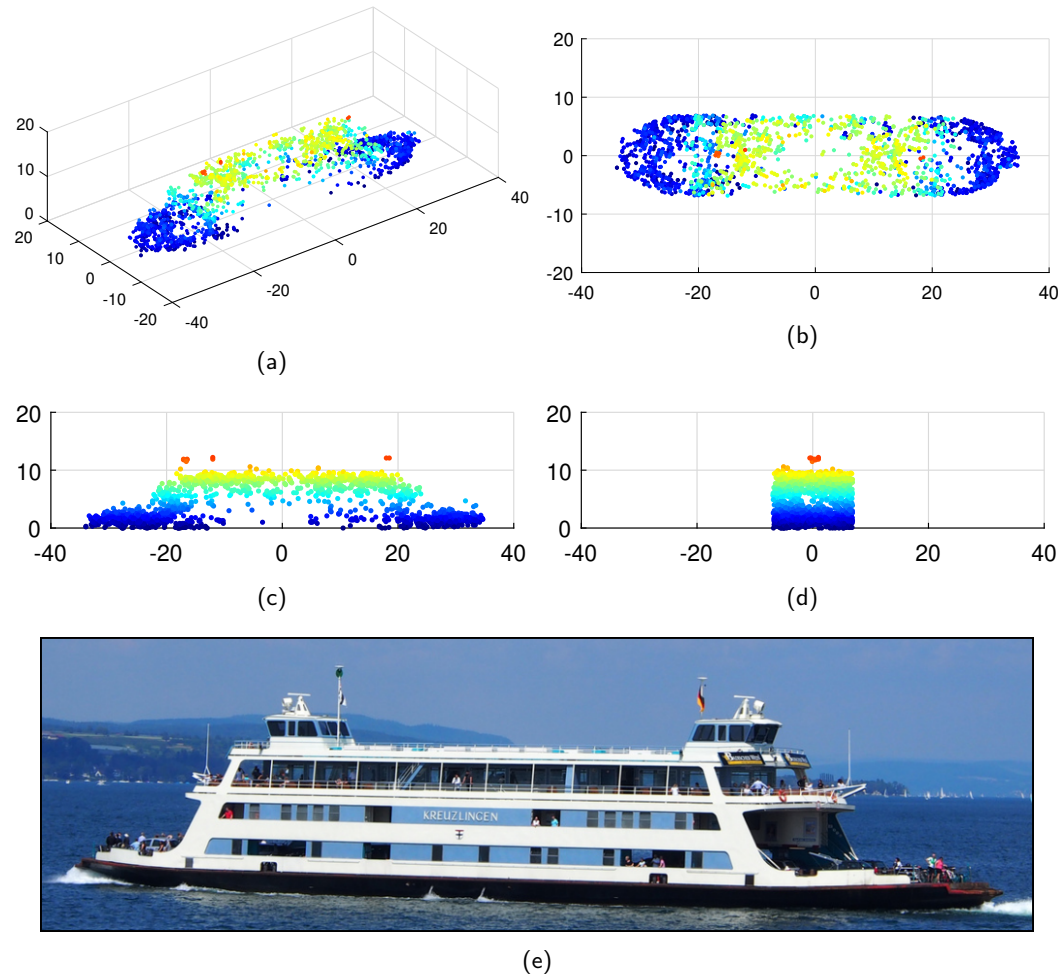

FIGURE 4.5: Target #1. Final point cloud: (a) 3-D view, (b) x-y plane, (c) x-z plane and (d) y-z plane. (e) Optical image.

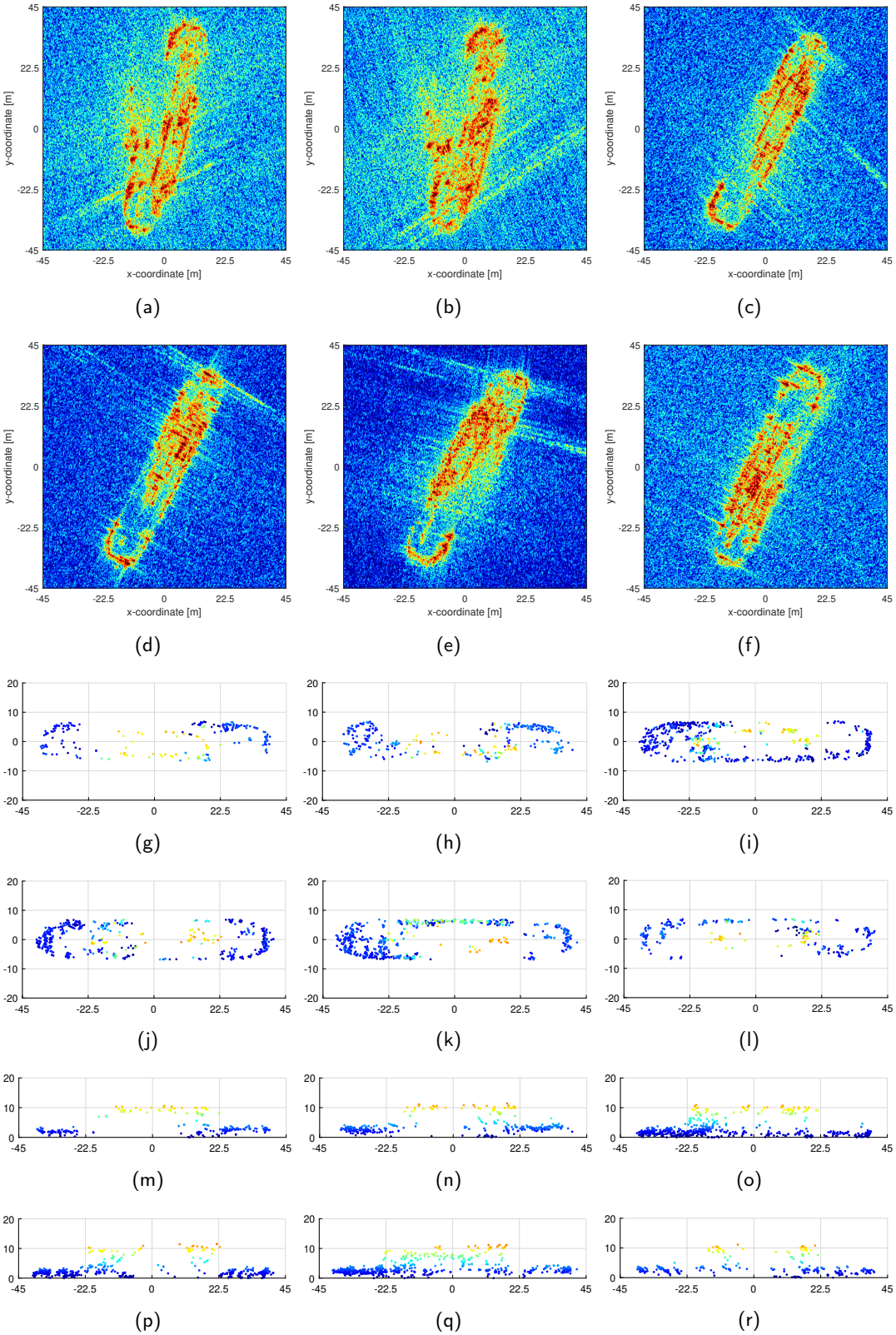
y-coordinate [m]
x-coordinate [m]
45
22.5
0
-22.5
-45
20
10
-10
-20
(a)
(b)
(c)
(d)
(e)
(f)
(g)
(h)
(i)
(j)
(k)
(l)
(m)
(n)
(o)
(p)
(q)
(r)

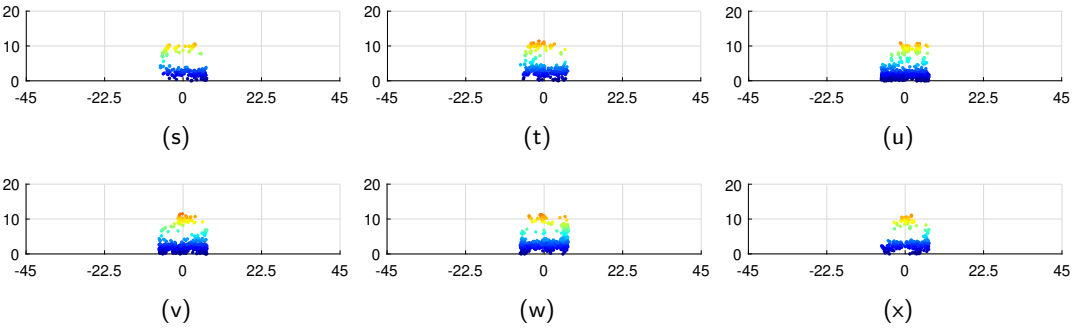

FIGURE 4.6: Target #2. (a–f) Refocused images. Point clouds: (g–l) x-y plane, (m–r) x-z plane and (s–x) y-z plane.

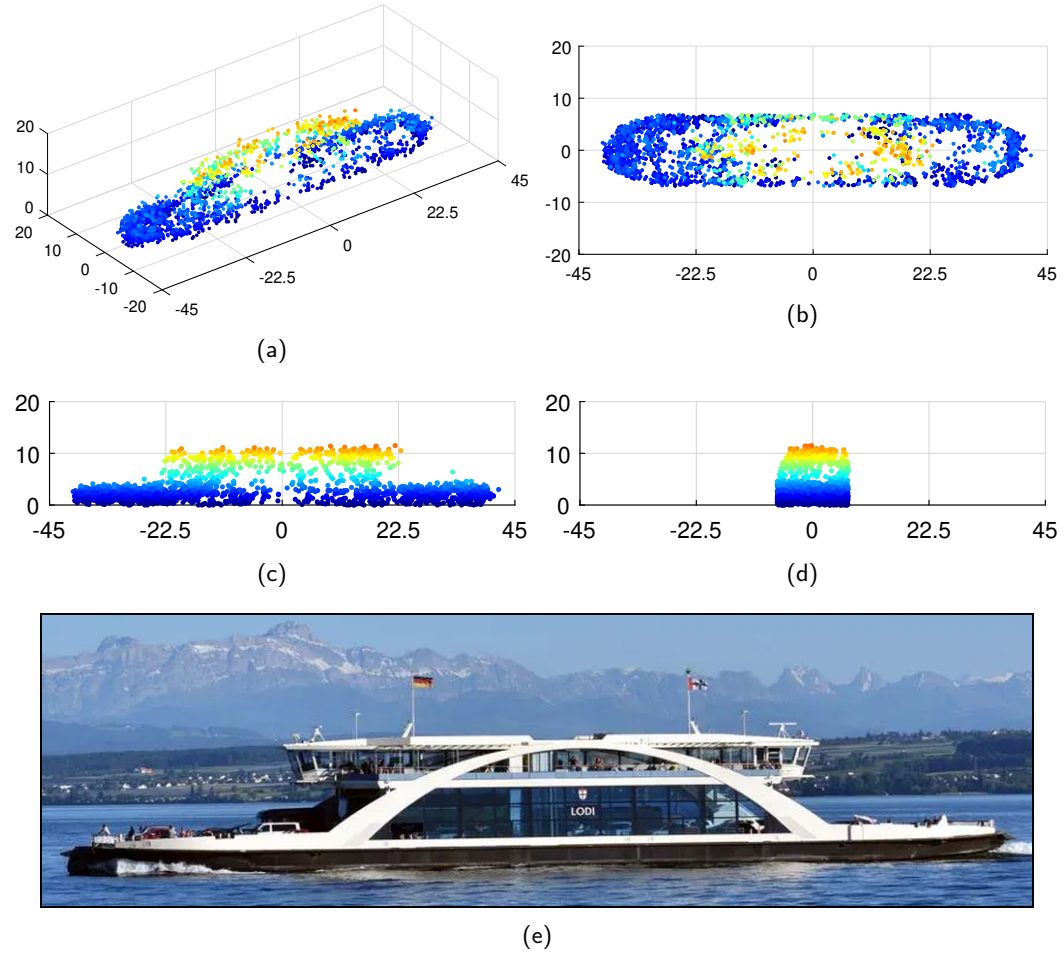

FIGURE 4.7: Target #2. Final point cloud: (a) 3-D view, (b) x-y plane, (c) x-z plane and (d) y-z plane. (e) Optical image.

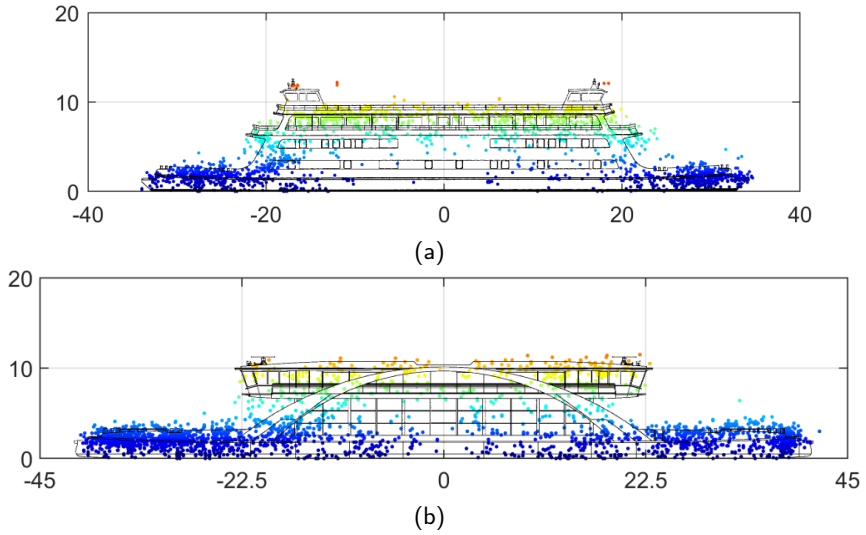

FIGURE 4.8: Superimposition of the ferry design on the derived point cloud (x-z plane). (a) Target #1. (b) Target #2.

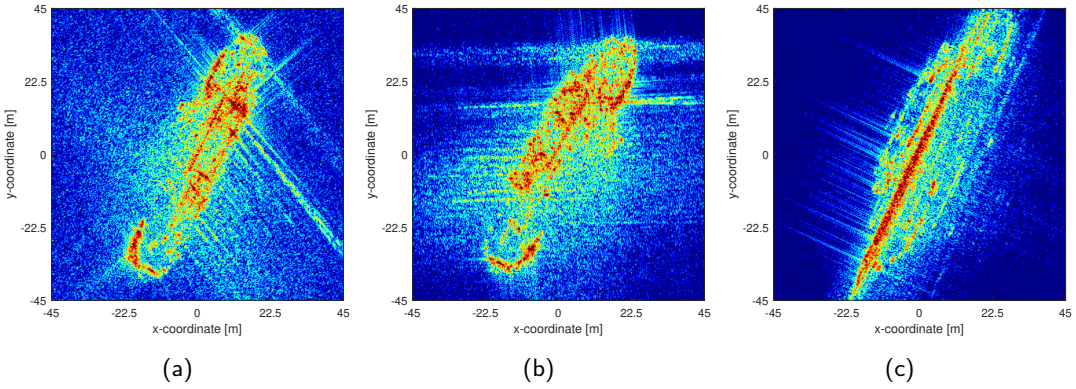

FIGURE 4.9: Additional refocused images of Target #2. The sensor position for these sub-apertures is highlighted with diamond markers in Fig. 4.10.

thus suggesting that they belong to the vehicle deck. The density decreases with height, up to the point where the higher parts of the vessel (e.g., see pilothouses in Fig. 4.8a) are represented by only a few points. This could be explained by low back-scatter with the RADAR parameters (frequency, polarization, incidence angle, etc.) in use. As evidenced in Fig. 4.5e and Fig. 4.7e, both passenger decks are open on the sides, and all pilothouses present glass side surfaces. Another explanation of the height-varying density could be found in the interaction between the targets and water. In fact, it is worth noting that most of the detections at ground level are located along the vehicle deck edges. These contributions could be due to the multiple scattering mechanisms involved in the interaction of the electromagnetic waves back-scattered by the vessel hull and the water surface.

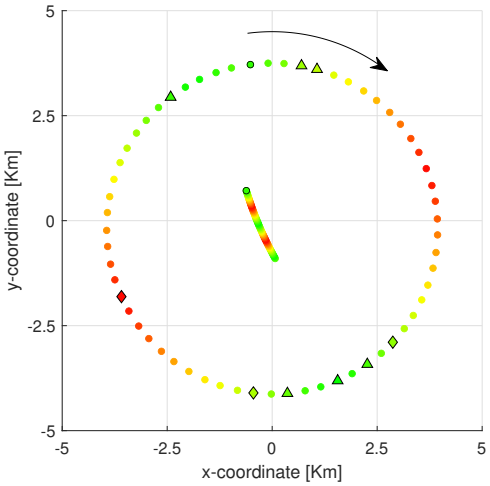

FIGURE 4.10: Sensor flight-path (circle) and Target #2 path (curve). Triangle markers identify the sensor position for sub-apertures #1–6 of Fig. 4.6. Diamond markers identify the sensor position for the additional sub-apertures of Fig. 4.9.

4.5.2 CSAR

Based on the results presented herein, CSAR was proved to be a powerful acquisition mode to obtain well-focused 2-D images and detailed point clouds of moving targets. The use of non-linear SAR acquisitions, like CSAR, offers multiple advantages in comparison to conventional stripmap SAR. For instance, linear flight-paths oftentimes suffer from shadowing effects: parts of the target with high vertical profiles block the electromagnetic signal and prevent the sensor from observing other parts of the target. This is not a problem for CSAR, as proven, for instance, by sub-apertures #2 and #5 of Target #1. From the refocused images (see Fig. 4.4b and Fig. 4.4e, respectively), one can observe that the relative geometries are almost symmetrical, the main difference being a 180 deg shift in viewing angle. In both cases, the vertical structures are layovered along the longitudinal axis of the vessel. However, their registration coordinates differ as they are imaged in the top- and bottom-half of the target in Fig. 4.4b and Fig. 4.4e, respectively. The corresponding point clouds show that, in these sub-apertures, the sensor observed different parts of the target vertical structures (see the green-colored detections in Fig. 4.4h, Fig. 4.4k, Fig. 4.4n and Fig. 4.4q).

Another advantage of CSAR is that the sub-apertures-derived point clouds can be merged to obtain a product with significantly higher point density. The merged point clouds (see Figs. 4.5a–4.5d and Figs. 4.7a–4.7d) better describe the targets of interest as they integrate the information acquired from different snapshots (see Figs. 4.4g–4.4x and Figs. 4.6g–4.6x).

Lastly, the use of a CSAR acquisition geometry allows to relate the obtained image quality to the viewing angle, giving insights on what flight geometry is the most convenient for imaging purposes. It is well-known that targets

moving along the line-of-sight induce a negligible Doppler excursion, and that the resulting images are characterized by an unsatisfactory resolution. This suggests that the most suitable images for target recognition and classification are those acquired when sensor and target move in opposite directions (see red-colored markers in the left-hand side of Fig. 4.10). Nonetheless, the obtained results rule this out, as highlighted in Fig. 4.9. A potential reason for this is the interfering behaviour of the target wake (i.e., the wave pattern on the water surface produced by a moving object), whose contribution appears to be quite disruptive when the vessel longitudinal axis is approximately parallel to the sensor flight-path. The chaotic nature of wake signal, together with the algorithm's inability to deal with intrinsically different signals (i.e., target and wake), could explain the aforementioned results.

4.5.3 General Comments

Using the GBP algorithm holds a number of implications, the most prominent one being that it does not require to estimate the imaging plane. Hence, the 2-D products (i.e, the refocused images) are naturally expressed in a homogeneous domain, thus making it possible to retrieve the target dimensions with no further steps. Moreover, the accuracy of the 3-D products is mainly limited by the phase noise, as no other sources of error are introduced. On the other hand, most of frequency-domain-based approaches have to rely on estimating the orientation of the imaging plane. As a consequence, the estimation error affects the 3-D geolocation of a given scatterer. Thus, specifically for non-linear (or CSAR) acquisitions, GBP-derived 3-D products are more accurate then the frequency-domain-based counterparts.

The main limitation of the proposed method is its higher computational complexity, a direct consequence of the adoption of the GBP algorithm. Nonetheless, the number of operations could be drastically reduced by using a more efficient processing solution, such as the fast factorized backprojection [114].

4.5.4 Summary and Outlook

This article presents a method to derive well-focused RADAR images and detailed point clouds of man-made moving targets from SAR data-sets acquired with arbitrary acquisition geometries. To this end, the conventional GBP algorithm, which is primarily designed to focus the stationary scene, has been modified in order to compensate for the relative motion between sensor and target. This approach can be iterated several times over the height dimension, therefore defining a stack of images, each one focused at a different height, for K receiving channels. The resulting 3-D cubes were further processed by making use of the MLE algorithm, and, for each resolution cell, $K-1$ scatterers were

extracted. In order to emphasize the advantages of CSAR, the resulting point clouds were merged, thus producing high density and accurate reconstructions of the targets of interest.

The algorithm has been tested on data-sets acquired with a circular acquisition geometry by the F-SAR sensor. In order to assess the performance of the proposed method, we compared the point cloud-derived dimensions of the targets, two double-ended ferries, with information provided by the original designs. Quality assessment showed that the percent errors of the estimates were marginal, thus demonstrating the capabilities of the algorithm and its potential use for target recognition and classification. In conclusion, the algorithm presented herein generates high-end tomographic images and reconstructs the 3-D shape of maritime moving targets from CSAR data-sets with excellent accuracy.

Future research shall focus on further refining the framework presented herein. To this end, particular attention shall be paid to reducing the computational burden, which has been proven to be a limiting factor. Moreover, the proposed method could be further tested with polarimetric SAR data-sets in order to differentiate the different scattering mechanism in the point cloud. Another task to be undertaken is the development of a time-domain-based autofocus algorithm. The current technological advances suggest that ultra-lightweight platforms, such as drones, might become a commonly used platform for future airborne SAR campaigns. Unfortunately, drones are not as stable as heavier aircrafts, therefore making the motion compensation process more challenging, and, in turn, prompting the need for more sophisticated autofocus algorithms.

Chapter 5

Synopsis

5.1 Main Results

The main findings of this dissertation are summarized according to the research questions presented in Section 1.5.

Moving Object Refocusing in FMCW-SAR Imagery

"How far is it possible to refocus a moving object using an algorithm based on the focusing technique that produced the input FMCW-SAR image?"

The performances of the proposed algorithm were assessed by using a variety of vehicles with different size, shape and motion. The latter was estimated with a relative error up to 4.38 % (see Experiment #1 in Chapter 2). While refocusing the moving objects, it was possible to infer the behaviour of the traffic flow (see Experiment #2 in Chapter 2). Large-sized vehicles, such as trucks, were all characterized by a low NRS, while small- and middle-sized vehicles exhibited much more diverse motion behaviours.

The SAR-derived lengths underestimate the real dimensions, with error ranging from 0.03 m to 3.26 m, and a mean value of 1.33 m. The refocused images, while not particularly accurate, allows to differentiate between small-, medium- and large-sized objects. To better appreciate the impact of the implemented algorithm, it should be noted that, prior to refocusing, the energy of a moving object would be smeared over an area as large as 120 m along the azimuth axis. Hence, the algorithm was demonstrated to estimate the range history of a moving object accurately enough to concentrate most of its energy within an area whose dimensions are of the same magnitude, or slightly smaller, than the *true* ones. The level of detail, however, is insufficient for most of the objects, making it impossible to retrieve further features. In this regard, it is worth highlighting that both range and azimuth resolution are quite low. The RADAR parameters in use defined a range resolution of only 0.5 m, while the acquisition geometry and the platform velocity limited the extension of the illumination time.

The proposed algorithm is based upon the well-known WDA with whom it shares similar assumptions, the most prominent one being that the relative motion between sensor and object is constant within the integration time. The object motion, which is modelled with a constant range and azimuth velocity, is likely to be characterized by a more complicated behaviour. Nonetheless, the algorithm was proven to be capable of estimating motion parameters with satisfying accuracy and producing RADAR images with realistic dimensions, hence making it a powerful tool for traffic monitoring applications. In this regards, it should be noted that the motion parameters were estimated with a relative error up to 4.38 %, with performances similar to that achieved by devices that are commonly used for speed limit enforcement. The speed enforcement tolerance, which takes into account the limited accuracy of the measuring device, is a function of many factors, including legislation, technology (e.g., RADAR and LIDAR), device state (i.e., stationary or moving) and location (i.e., straight or curved road), and measured velocity. In Switzerland, for a stationary RADAR speed measuring device placed on a straight road, a $5\,\mathrm{km\,h^{-1}}$ tolerance is deducted from measurements up to $100\,\mathrm{km\,h^{-1}}$. This accounts for a relative error up to 5 %, which is slightly larger than the one obtained by the proposed algorithm. The tolerance increases for measurements acquired by a device located on a curved road, or for a mobile device. In conclusion, the proposed algorithm achieves performances as good as those of close-range speed measuring devices. However, unlike the latter, the resulting products allow to contemporaneously monitor multiple moving objects over much larger areas.

Moving Object Refocusing with a Light-Weight Platform

"How good can state-of-the-art ISAR-based techniques perform when resources are poor and physical design constraints are present, such as in the case of light-weight systems?"

The need for compact and inexpensive solutions, yet characterized by state-of-the-art performances, has led to the ever-increasing number of light-weight SAR systems. The imaging capabilities of MIRANDA-35, an airborne system using FMCW technology and operating at Ka-band, were demonstrated by refocusing two types of objects (i.e., a ferry and a truck) with an ISAR-based algorithm.

The proposed algorithm is capable of estimating both velocity and acceleration of a moving object. For the ferry (see Experiment #1 in Chapter 3), the minimum, mean and maximum percent error of the radial velocity and acceleration are (1.78 %, 2.37 %, 2.67 %) and (0.28 %, 2.02 %, 5.05 %), respectively. For the truck, on the other hand, the percent errors (see Experiment #2 in Chapter 3) are (1.02 %, 1.73 %, 2.98 %) and (1.13 %, 2.19 %, 3.23 %), respectively. The

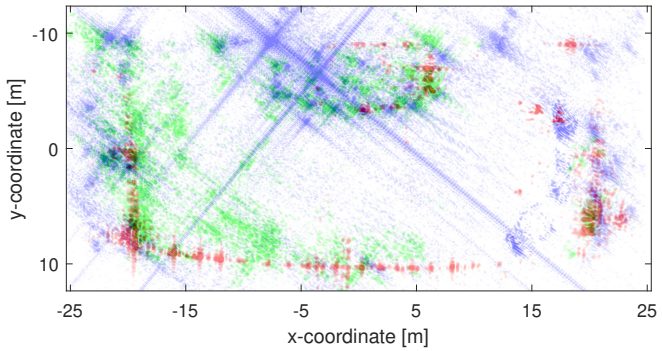

FIGURE 5.1: RGB composite of the object of interest: (red) Frame #1, (green) Frame #2, (blue) Frame #3

SAR-derived lengths and widths give a percent error with minimum, mean and maximum value equal to $(3.65\,\%, 4.76\,\%, 6.94\,\%)$ and $(3.14\,\%, 3.77\,\%, 4.53\,\%)$, respectively.

The resulting RADAR images exhibit strong similarities with the corresponding optical images. This is particularly true in the case of the ferry: not only the reconstructed shape resembles the original, but it is also possible to identify additional features, such as the pilothouse and the parked vehicles on the deck. The high quality of the obtained images is the product of a number of different factors. The adopted RADAR parameters allows to achieve a nominal range resolution of 0.15 m. Moreover, using such a short wavelength (i.e., 8.6 mm) induces a large Doppler excursion and, potentially, a high azimuth resolution. The latter, however, can only be accomplished when the imaging algorithm precisely compensates for the relative motion between sensor and object.

Despite the light-weight platform and the high operating frequency, the ISAR-based algorithm was able to perform well enough to retrieve a variety of information, including motion and geometric parameters. The high detail of the resulting images allows not only to recognize the object of interest, but also to monitor its changes over time. To appreciate this, please refer to the RGB composite image in Fig. 5.1, formed using the refocused images depicted in Fig. 3.5a–c. For frame #2, one can identify a series of rectangular-shaped contributions on the left-hand side of the image, most likely produced by a queue of vehicles. *Vice-versa*, for the remaining frames, the signatures of the parked vehicles, though being much more attenuated and confined in a smaller region (i.e., the ferry is transporting fewer vehicles), can be identified on the right-hand side of the image. Hence, from the direct comparison of RADAR images acquired at different times it is possible to detect changes, such as the arrangement of parked vehicles on a ferry deck. In a similar fashion, the proposed algorithm, in combination with a sensor capable of high-resolution imaging, could be used, for instance, to detect illegal activities at sea (i.e., discharging

of containers, barrels, etc.), monitor vessels in distress or aid search-and-rescue missions.

Three-Dimensional Imaging with a Circular Acquisition

"To what extent are three-dimensional imaging techniques capable of retrieving geometrical features of a moving object from circular SAR data?"

Conventional stripmap SAR acquisition oftentimes suffers from shadowing effects, hence giving incomplete products. The dimensions (i.e., length, width and height) of a moving object derived from such products tend to underestimate the *true* values, and the reconstructed shape does not resemble the original. This limitation can be overcome by adopting a circular acquisition geometry, which allows to observe the object from multiple viewing angles.

The capabilities of CSAR for imaging purposes were evaluated by analysing the two- and three-dimensional images of two different ferries. The length, width and height retrieved from the final point clouds (i.e., after fusion) give a percent error of $(0.91\,\%, 2.38\,\%, 6.09\,\%)$ and $(0.10\,\%, 2.33\,\%, 6.92\,\%)$, respectively. Merging the information derived from different sub-apertures allows to obtain more reliable products: for ferry #1, for instance, the height derived from the single sub-apertures results in percent errors as high as $19.13\,\%$, roughly three times larger than the estimate obtained from the final point cloud.

The reconstructed shape presents a variety of features that are present in the corresponding optical image. The projection of the final point clouds on any of the three main planes yields symmetrical results, in accordance with the real geometry of both ferries. Moreover, not only it is possible to detect the lower and upper deck of each ferry, but one can also identify the pilothouses.

In conclusion, CSAR was demonstrated to be particularly suitable for obtaining a high quality point cloud of a moving object. The main advantage of CSAR is that the final product exhibits the information acquired from different sub-apertures. Hence, the point cloud does not present gaps and is characterized by a significantly higher point density, which is crucial for object recognition. Moreover, one of the main peculiarities of the proposed algorithm is the use of a time-domain processor, which allows to back-project the refocused images directly onto a DTM of choice. Although, on the one hand, this approach increases the computational time, on the other hand, the height estimates are much more accurate than those obtained with conventional frequency-domain based processors. The resulting products, though being characterized by a fair amount of outliers mostly concentrated in the areas between lower and upper deck, result to resemble the ground truth. The ability to reconstruct the

three-dimensional geometry allows to discriminate between objects with similar horizontal dimensions (i.e., length and width), but different height and/or shape.

5.2 Conclusions

Within this dissertation, the potential and challenges of refocusing moving objects in SAR imagery were investigated through different experiments. The main contribution of this study is the development of both two- and three-dimensional imaging algorithms, which were designed paying particular attention to many aspects, including RADAR technology, platform typology and acquisition geometry.

Chapter 2 has focused on assessing the feasibility of FMCW-SAR for moving object imaging. The proposed algorithm is, in our knowledge, one of the first attempts to integrate the peculiar nature of FMCW waveforms into the imaging process. The obtained results have demonstrated the effectiveness of the proposed algorithm and the possibility of application of FMCW-technology for wide area traffic monitoring.

The capabilities of FMCW-ISAR, a newly developed state-of-the-art imaging technique, are discussed in Chapter 3. In this study, an ISAR-based approach was applied to data-sets acquired with unconventional settings, including millimeter-wave wavelength, FMCW technology, and light-weight platform. The obtained results confirm the capabilities of the proposed approach to produce highly detailed RADAR images of maritime objects.

In Chapter 4, both challenges and opportunities of using a circular acquisition geometry are discussed. Unlike most methods available in the literature, which are successful only when the platform flight-path is linear, the proposed algorithm is capable of delivering high quality products even with strongly nonlinear acquisition geometries. The high detail of the resulting three-dimensional products demonstrates that the proposed algorithm can be successfully used for object recognition.

The experiments discussed in detail throughout this dissertation appear not to be linked to a specific application. However, it should be noted that they were primarily designed to help define new methods, and to gain insights on how to overcome the technical challenges associated with moving objects in SAR imagery. Thanks to the analysis of the acquired data-sets, and the newly-designed methods, it is now possible to better interpret SAR images, which is oftentimes challenging, even for an experienced specialist. A successful compensation of the motion-induced blurring effects allows to unveil hidden information, which is crucial for a variety of real-world applications. Among these, the analysis of traffic flows, whether on land or at sea, benefits greatly from high quality

products produced by two- and three-dimensional imaging algorithms. Reliable and detailed traffic data are a prerequisite to retrieve traffic flow characteristics, an essential information for the planning and design of new transportation systems, or for the renovation of already existing ones. Moreover, a thorough analysis of traffic flows and their spatio-temporal dynamics allows, for instance, to assess the socio-economic status of countries or regions, or to evaluate the environmental impact of activities such as commercial trading and tourism. The proposed algorithms are capable of estimating both motion and geometric parameters of a moving object with satisfying accuracy, and thus can be used to deliver detailed traffic data at regional-to-global scale.

Furthermore, maritime surveillance is another field that benefits immensely from the emergence of RADAR imaging techniques. Safety and security management at sea has become a major concern in the past decade due to the increase in commercial trading, fishing activities and migration flows. An efficient and effective monitoring of maritime activities can only be carried out provided that fast, detailed and reliable information is made available to law enforcement agencies. This shall include accurate geolocation of the vessel of interest, as well as further data such as vessel type, geometry and trajectory. Unfortunately, oftentimes these data are deliberately not provided (i.e., in the case of illegal activities) or cannot be provided (i.e., in the case of an emergency). In all these cases, situational awareness can be significantly improved by processing SAR imagery with properly designed imaging algorithms. This is confirmed by the results of this thesis: the proposed three-dimensional imaging algorithm guarantees such a high level of detail that allows to discriminate between different parts of a vessel. Hence, this algorithm is well suited, for instance, to identifying vessels conducting illegal activities, or to monitoring the status of a vessel in distress.

Lastly, it is important to highlight that the proposed methods are of great importance in many other fields. A few examples are the detection and monitoring of illegal activities, such as illegal fishing or logging, which have great socio-economic and environmental impacts, or the monitoring of environmental disasters, such as in the case of an oil spill at sea, which have tremendous impacts on the marine ecosystems.

5.3 Outlook

5.3.1 Pixel-Dependent Refocusing

All proposed algorithms rely on using the same phase correction to refocus the entire object of interest. Obviously, this solution is an approximation since each scatterer is characterized by a slightly different range history. Hence, one

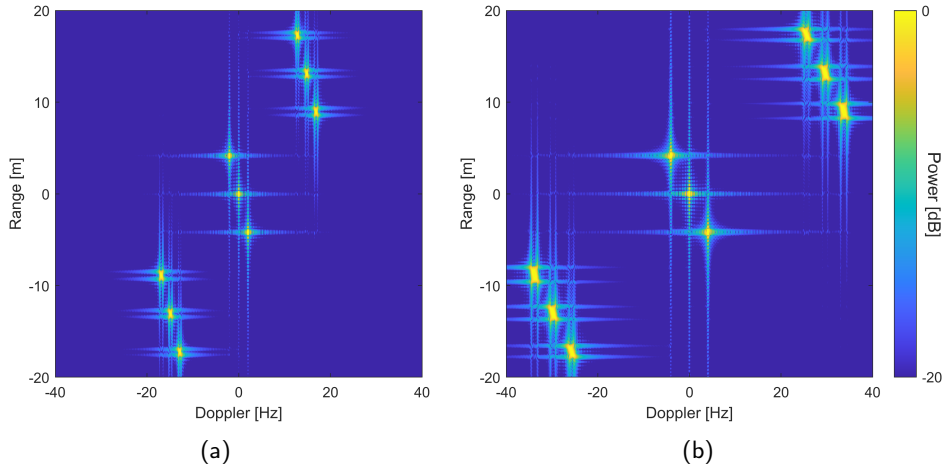

FIGURE 5.2: Range/Doppler image of a simulated moving object for different ranges of minimum approach R: (a) $R = 10\,\text{km}$, (b) $R = 5\,\text{km}$

specific point, the so-called focusing point, will be optimally focused while the remaining ones will exhibit lower degrees of focusing.

The errors introduced by this approximation are marginal when the object physical dimensions are much smaller than the distance between sensor and object. This is particularly valid for spaceborne applications, where even the largest moving object is small compared to the distance to the sensor. For airborne applications, however, the distance can decrease as low as few hundreds of meters, or even lower when using an ultra-light-weight platform such as a small-sized drone.

Fig. 5.2 illustrates the decrease in focusing quality obtained when this approximation no longer holds. The figure depicts the range/Doppler image of an object with dimensions $\{L = 68\,\text{m}, W = 13.4\,\text{m}, H = 0\,\text{m}\}$ (i.e., the same horizontal dimensions of ferry #1 in Chapter 4) moving with a linear trajectory at a typical vessel speed. In order to simulate the SAR data, the object was modelled as a set of nine ideal point-like scatterers with unit reflectivity, while the system parameters were set equal to the ones summarized in Table 4.1. For both images, the focusing quality degrades the further away the scatterers are from the focusing point, which, for the given example, is located in the origin of the coordinate system. However, it should be noted that the defocusing is much more evident for Fig. 5.2a, for which the distance between sensor and object is shorter.

In conclusion, short-range RADAR imaging cannot use the aforementioned approximation, hence prompting the need for a pixel-dependent refocusing algorithm, capable of compensating for the range histories of the different scatterers.

5.3.2 Terahertz RADAR Imaging

The main advantage of terahertz RADAR technology is that it provides a bandwidth as large as several tens of gigahertz, hence allowing to achieve millimeter resolution. Due to the extreme level of detail and the high image quality, terahertz RADAR products result to be useful for many RS applications. Safety and security management is the field that benefits most from such products: millimeter wavelengths, in fact, can penetrate clothes and other disguising material, thus making them particularly suitable for detecting and imaging concealed weapons (e.g., guns and explosive materials).

Unfortunately, atmospheric attenuation and technological challenges substantially limit the range of operation. At this moment, short-range airborne applications up to few hundreds of meters, though being extremely challenging, are possible, while longer range applications are simply not viable. In contrast to these limitations, terahertz imaging systems offer a very compact and light-weight design, and can be mounted on-board of any platform, including a small sized UAV.

RADAR imaging in terahertz band, whether of a static scene or of a moving object, has only marginally been researched. Despite the challenging aspects, many of them still unknown, preliminary results for both SAR and ISAR applications have shown the feasibility and efficacy of such systems [115–117]. However, the imaging of a moving object has only been carried out in a safe and controlled environment, where the object of interest is placed on a turntable [115, 116]. Hence, it remains an open question as to whether it is possible to produce well-focused images of a moving object with a more realistic motion behaviour. In this regard, particular attention shall be paid to designing new imaging algorithms, as the current state-of-the-art methods, most of them specifically designed for lower bands, are likely to fail. Moreover, of particular interest will be the analysis of the information content of the final products, especially when illuminating small objects (e.g., small-sized cars or motorbikes), which oftentimes appear as an unshaped blob of pixels when operating at lower frequencies.

5.3.3 Further Applications

In the past, the most commonly used platforms for airborne RADAR imaging were medium to large-sized airplanes capable of carrying quite heavy and voluminous payloads. Nowadays, RADAR systems are much more compact and light-weight, and therefore they can be mounted on-board smaller aircrafts, such as an ultra-light-weight airplane or even a commercial off-the-shelf drone. Drones are much more efficient in terms of costs, manpower and time, and

thus have been recently acknowledged as a potential platform for SAR data collection [118, 119].

Drone-borne SAR systems could be deployed, for instance, to address problematic phenomena such as human trafficking and illegal migration activities. The large availability of drones and their limited costs makes it possible to deploy a network of RADAR sensors in sensitive areas, be it a sea or the border between two states. This would provide the possibility to detect such events and, more importantly, to promptly react in case of an emergency. However, for such a system to be effective, several factors have to be taken into consideration during design, including the shorter distances between sensor and earth's surface as well as the higher vulnerability to flight turbulence. Particular attention shall be paid to accurately reconstructing the drone trajectory, which has a crucial impact on the quality of SAR imagery and subsequent products.

Furthermore, the high maneuverability of drones allows them to *follow* an object of interest, hence increasing the chances of a successful recognition. This prompts the question as to whether or not drone-based solutions are effective for carrying out safety and security management at sea, or for ensuring the protection of marine environments. Vessels conducting illegal activities can be detected with remotely sensed satellite data. However, the revisit time of satellites usually ranges from few hours up to several days, therefore making it impossible to continuously illuminate the same area. A potential solution to this problem consists in combining satellites with drones, therefore preserving the unique features of both approaches. Satellite imagery would be exploited to accurately geolocate the vessel conducting illegal activities, while a drone, or a fleet of drones, would be used to track the vessel and continuously observe it. The design of a sophisticated tracking algorithm, as well as the definition of optimal flight trajectories to maximize the quality of the final RADAR products, are only few of the many challenges that need to be carefully addressed.

Despite being cost-intensive and technically challenging, satellite platforms remain a fundamental source of information in the field of RS. Spaceborne SAR data-sets contain an incredible amount of information and can be used, among others, to derive global scale traffic networks and to evaluate their dynamics over the years. From a geographical perspective, this is particularly interesting as trends in trading activity are directly linked to the socio-economic status of a country. In fact, from global scale traffic data we can infer the geographical distribution of trade flows, and identify, for instance, the emerging role of developing economies, or the leading position of developed ones. Moreover, being able to recognize the mode of transport (e.g., container ship, dry cargo, tanker, bulker and ro-ro) is crucial as it uniquely identifies what type of goods are being transported. Container ships are used to transport goods such as televisions, computers, clothing and toys, while dry cargos transport huge quantities of

non-packaged items such as grain, coal, iron and cement. Combining space-borne SAR imagery with a properly designed imaging algorithm would allow to discriminate between ship types, hence delivering even more detailed and thorough traffic characteristics. To this end, particular attention shall be paid to designing automatic detection schemes, further refining the proposed imaging algorithms to reduce the computational time, and designing automatic procedures to recognize a given ship from its reconstructed point cloud.

Bibliography

[1] T. Lillesand, R. W. Kiefer, and J. Chipman, *Remote sensing and image interpretation.* John Wiley & Sons, 2015.

[2] J. B. Campbell and R. H. Wynne, *Introduction to remote sensing.* Guilford Press, 2011.

[3] R. O. Green, M. L. Eastwood, C. M. Sarture, T. G. Chrien, M. Aronsson, B. J. Chippendale, J. A. Faust, B. E. Pavri, C. J. Chovit, M. Solis, *et al.*, "Imaging spectroscopy and the airborne visible/infrared imaging spectrometer (AVIRIS)," *Remote sensing of environment*, vol. 65, no. 3, pp. 227–248, 1998.

[4] M. E. Schaepman, S. L. Ustin, A. J. Plaza, T. H. Painter, J. Verrelst, and S. Liang, "Earth system science related imaging spectroscopy—An assessment," *Remote Sensing of Environment*, vol. 113, pp. S123–S137, 2009.

[5] C. Mallet and F. Bretar, "Full-waveform topographic lidar: State-of-the-art," *ISPRS Journal of photogrammetry and remote sensing*, vol. 64, no. 1, pp. 1–16, 2009.

[6] J. Shan and C. K. Toth, *Topographic laser ranging and scanning: principles and processing.* CRC Press, 2018.

[7] M. I. Skolnik, *Introduction to radar systems.* McGraw Hill, 1962.

[8] J. A. Richards *et al.*, *Remote sensing with imaging radar.* Springer, 2009.

[9] M. Steven and J. A. Clark, *Applications of remote sensing in agriculture.* Elsevier, 2013.

[10] C. Atzberger, "Advances in remote sensing of agriculture: Context description, existing operational monitoring systems and major information needs," *Remote sensing*, vol. 5, no. 2, pp. 949–981, 2013.

[11] T. J. Schmugge, W. P. Kustas, J. C. Ritchie, T. J. Jackson, and A. Rango, "Remote sensing in hydrology," *Advances in water resources*, vol. 25, no. 8-12, pp. 1367–1385, 2002.

[12] G. A. Schultz and E. T. Engman, *Remote sensing in hydrology and water management.* Springer Science & Business Media, 2012.

[13] D. Hall, *Remote sensing of ice and snow.* Springer Science & Business Media, 2012.

[14] A. J. Dietz, C. Kuenzer, U. Gessner, and S. Dech, "Remote sensing of snow–a review of available methods," *International Journal of Remote Sensing*, vol. 33, no. 13, pp. 4094–4134, 2012.

[15] D. J. Quincey and A. Luckman, "Progress in satellite remote sensing of ice sheets," *Progress in Physical Geography*, vol. 33, no. 4, pp. 547–567, 2009.

[16] C. Linard, M. Gilbert, R. W. Snow, A. M. Noor, and A. J. Tatem, "Population distribution, settlement patterns and accessibility across Africa in 2010," *PLoS ONE*, vol. 7, no. 2, p. e31743, 2012.

[17] F. R. Stevens, A. E. Gaughan, C. Linard, and A. J. Tatem, "Disaggregating census data for population mapping using random forests with remotely-sensed and ancillary data," *PLoS ONE*, vol. 10, no. 2, p. e0107042, 2015.

[18] J. E. Patino and J. C. Duque, "A review of regional science applications of satellite remote sensing in urban settings," *Computers, Environment and Urban Systems*, vol. 37, pp. 1–17, 2013.

[19] M. Kuffer, K. Pfeffer, and R. Sliuzas, "Slums from space—15 years of slum mapping using remote sensing," *Remote Sensing*, vol. 8, no. 6, p. 455, 2016.

[20] C. V. Tao and J. Li, *Advances in mobile mapping technology*. CRC Press, 2007.

[21] D. Cerutti-Maori, J. Klare, A. R. Brenner, and J. H. Ender, "Wide-area traffic monitoring with the SAR/GMTI system PAMIR," *IEEE Transactions on Geoscience and Remote Sensing*, vol. 46, no. 10, pp. 3019–3030, 2008.

[22] D. Cerutti-Maori, I. Sikaneta, and C. H. Gierull, "Optimum SAR/GMTI processing and its application to the radar satellite RADARSAT-2 for traffic monitoring," *IEEE Transactions on Geoscience and Remote Sensing*, vol. 50, no. 10, pp. 3868–3881, 2012.

[23] J. C. Perez, M. A. Alvarez, J. Heikkonen, J. Guillen, and T. Barbas, "The efficiency of using remote sensing for fisheries enforcement: Application to the Mediterranean bluefin tuna fishery," *Fisheries research*, vol. 147, pp. 24–31, 2013.

[24] B. Fiscella, A. Giancaspro, F. Nirchio, P. Pavese, and P. Trivero, "Oil spill detection using marine SAR images," *International Journal of Remote Sensing*, vol. 21, no. 18, pp. 3561–3566, 2000.

[25] A. H. Solberg, C. Brekke, and P. O. Husoy, "Oil spill detection in Radarsat and Envisat SAR images," *IEEE Transactions on Geoscience and Remote Sensing*, vol. 45, no. 3, pp. 746–755, 2007.

[26] T. N. Arnesen and R. Olsen, "Literature review on vessel detection," tech. rep., Norwegian Defence Research Establishment, 2004.

[27] U. Kanjir, H. Greidanus, and K. Oštir, "Vessel detection and classification from spaceborne optical images: A literature survey," *Remote sensing of environment*, vol. 207, pp. 1–26, 2018.

[28] F. Topputo, M. Massari, R. Lombardi, M. Gianinetto, A. Marchesi, M. Aiello, S. Tebaldini, and F. Banda, "Space shepherd: Search and rescue of illegal immigrants in the mediterranean sea through satellite imagery," in *Proc. IGARSS*, (Milan, Italy), pp. 4852–4855, IEEE, July 2015.

[29] U. Kanjir, "Detecting migrant vessels in the Mediterranean Sea: Using Sentinel-2 images to aid humanitarian actions," *Acta Astronautica*, vol. 155, pp. 45–50, 2019.

[30] P. Lanz, A. Marino, T. Brinkhoff, F. Köster, and M. Möller, "The InflateSAR Campaign: Evaluating SAR Identification Capabilities of Distressed Refugee Boats," *Remote Sensing*, vol. 12, no. 21, p. 3516, 2020.

[31] P. Lanz, A. Marino, T. Brinkhoff, F. Köster, and M. Möller, "The InflateSAR Campaign: Testing SAR Vessel Detection Systems for Refugee Rubber Inflatables," *Remote Sensing*, vol. 13, no. 8, p. 1487, 2021.

[32] J. C. Curlander and R. N. McDonough, *Synthetic Aperture Radar: Systems and Signal Processing*. Wiley, New York, 1991.

[33] I. G. Cumming and F. H. Wong, *Digital processing of synthetic aperture radar data*. Artech House, 2005.

[34] W. Dierking, "Sea ice monitoring by synthetic aperture radar," *Oceanography*, vol. 26, no. 2, pp. 100–111, 2013.

[35] X. Li, S. Lehner, and W. Rosenthal, "Investigation of ocean surface wave refraction using TerraSAR-X data," *IEEE Transactions on Geoscience and Remote Sensing*, vol. 48, no. 2, pp. 830–840, 2009.

[36] L. C. Graham, "Synthetic interferometer radar for topographic mapping," *Proceedings of the IEEE*, vol. 62, no. 6, pp. 763–768, 1974.

[37] M. Yeremy, J. Campbell, K. Mattar, and T. Potter, "Ocean surveillance with polarimetric SAR," *Canadian Journal of Remote Sensing*, vol. 27, no. 4, pp. 328–344, 2001.

[38] E. Casalini, E. M. Domínguez, and D. Henke, "Multi-View Three-Dimensional Radar Imaging of Moving Targets with Time-Domain Processing," *IEEE Transactions on Geoscience and Remote Sensing*, 2021.

[39] R. K. Raney, "Synthetic aperture imaging radar and moving targets," *IEEE Transactions on Aerospace and Electronic Systems*, vol. AES-7, no. 3, pp. 499–505, 1971.

[40] R. Perry, R. Dipietro, and R. Fante, "SAR imaging of moving targets," *IEEE Transactions on Aerospace and Electronic Systems*, vol. 35, no. 1, pp. 188–200, 1999.

[41] E. Chapin and C. W. Chen, "Airborne along-track interferometry for GMTI," *IEEE Aerospace and Electronic Systems Magazine*, vol. 24, no. 5, pp. 13–18, 2009.

[42] D. Cerutti-Maori and I. Sikaneta, "A generalization of DPCA processing for multichannel SAR/GMTI radars," *IEEE Transactions on Geoscience and Remote Sensing*, vol. 51, no. 1, pp. 560–572, 2013.

[43] J. H. G. Ender, "Space-time processing for multichannel synthetic aperture radar," *Electronics & Communication engineering journal*, vol. 11, no. 1, pp. 29–38, 1999.

[44] D. Henke, E. M. Dominguez, D. Small, M. E. Schaepman, and E. Meier, "Moving target tracking in SAR data using combined exo-and endo-clutter processing," *IEEE Transactions on Geoscience and Remote Sensing*, vol. 56, no. 1, pp. 251–263, 2017.

[45] D. Cristallini, D. Pastina, F. Colone, and P. Lombardo, "Efficient detection and imaging of moving targets in SAR images based on chirp scaling," *IEEE Transactions on Geoscience and Remote Sensing*, vol. 51, no. 4, pp. 2403–2416, 2012.

[46] V. T. Vu, M. I. Pettersson, and T. K. Sjögren, "Moving target focusing in SAR image with known normalized relative speed," *IEEE Transactions on Aerospace and Electronic Systems*, vol. 53, no. 2, pp. 854–861, 2017.

[47] F. Zhou, R. Wu, M. Xing, and Z. Bao, "Approach for single channel SAR ground moving target imaging and motion parameter estimation," *IET Radar, Sonar & Navigation*, vol. 1, no. 1, pp. 59–66, 2007.

[48] Z. Li, J. Wu, Z. Liu, Y. Huang, H. Yang, and J. Yang, "An optimal 2-D spectrum matching method for SAR ground moving target imaging," *IEEE Transactions on Geoscience and Remote Sensing*, vol. 56, no. 10, pp. 5961–5974, 2018.

[49] J. K. Jao, "Theory of synthetic aperture radar imaging of a moving target," *IEEE Transactions on Geoscience and remote sensing*, vol. 39, no. 9, pp. 1984–1992, 2001.

[50] J. L. Walker, "Range-Doppler imaging of rotating objects," *IEEE Transactions on Aerospace and Electronic systems*, vol. AES-16, no. 1, pp. 23–52, 1980.

[51] D. A. Ausherman, A. Kozma, J. L. Walker, H. M. Jones, and E. C. Poggio, "Developments in radar imaging," *IEEE Transactions on Aerospace and Electronic Systems*, vol. AES-20, no. 4, pp. 363–400, 1984.

[52] G. Y. Delisle and H. Wu, "Moving target imaging and trajectory computation using ISAR," *IEEE Transactions on Aerospace and Electronic Systems*, vol. 30, no. 3, pp. 887–899, 1994.

[53] M. Martorella, F. Berizzi, and B. Haywood, "Contrast maximisation based technique for 2-D ISAR autofocusing," *IEE Proceedings-Radar, Sonar and Navigation*, vol. 152, no. 4, pp. 253–262, 2005.

[54] M. Martorella, E. Giusti, F. Berizzi, A. Bacci, and E. Dalle Mese, "ISAR based technique for refocusing non-cooperative targets in SAR images," *IET Radar, Sonar & Navigation*, vol. 6, no. 5, pp. 332–340, 2012.

[55] M. Martorella, D. Pastina, F. Berizzi, and P. Lombardo, "Spaceborne radar imaging of maritime moving targets with the Cosmo-SkyMed SAR system," *IEEE Journal of Selected Topics in Applied Earth Observations and Remote Sensing*, vol. 7, no. 7, pp. 2797–2810, 2014.

[56] E. Giusti and M. Martorella, "Range Doppler and image autofocusing for FMCW inverse synthetic aperture radar," *IEEE Transactions on Aerospace and Electronic Systems*, vol. 47, no. 4, pp. 2807–2823, 2011.

[57] M. Martorella, E. Giusti, A. Bacci, F. Berizzi, and A. Meta, "Non-cooperative maritime target imaging with an FMCW SAR system," in *Proc. EUSAR*, (Nuremberg, Germany), pp. 127–130, VDE, Apr. 2012.

[58] M. Iwamoto and T. Kirimoto, "A novel algorithm for reconstructing three-dimensional target shapes using sequential radar images," in *Proc. IGARSS*, (Sydney, NSW, Australia), pp. 1607–1609, IEEE, July 2001.

[59] F. E. McFadden, "Three-dimensional reconstruction from ISAR sequences," in *Proc. SPIE*, (Orlando, FL, USA), pp. 58–67, International Society for Optics and Photonics, July 2002.

[60] L. Liu, F. Zhou, X.-R. Bai, M.-L. Tao, and Z.-J. Zhang, "Joint cross-range scaling and 3D geometry reconstruction of ISAR targets based on factorization method," *IEEE Transactions on Image Processing*, vol. 25, no. 4, pp. 1740–1750, 2016.

[61] T. Morita and T. Kanade, "A sequential factorization method for recovering shape and motion from image streams," *IEEE Transactions on Pattern Analysis and Machine Intelligence*, vol. 19, no. 8, pp. 858–867, 1997.

[62] G. Wang, X.-G. Xia, and V. C. Chen, "Three-dimensional ISAR imaging of maneuvering targets using three receivers," *IEEE Transactions on Image Processing*, vol. 10, no. 3, pp. 436–447, 2001.

[63] J. A. Given and W. R. Schmidt, "Generalized ISAR-Part II: Interferometric techniques for three-dimensional location of scatterers," *IEEE Transactions on Image Processing*, vol. 14, no. 11, pp. 1792–1797, 2005.

[64] M. Martorella, D. Stagliano, F. Salvetti, and N. Battisti, "3D interferometric ISAR imaging of noncooperative targets," *IEEE Transactions on Aerospace and Electronic Systems*, vol. 50, no. 4, pp. 3102–3114, 2014.

[65] F. Salvetti, M. Martorella, E. Giusti, and D. Stagliano, "Multiview three-dimensional interferometric inverse synthetic aperture radar," *IEEE Transactions on Aerospace and Electronic Systems*, vol. 55, no. 2, pp. 718–733, 2018.

[66] E. Casalini, M. Frioud, D. Small, and D. Henke, "Refocusing FMCW SAR moving target data in the wavenumber domain," *IEEE Transactions on Geoscience and Remote Sensing*, vol. 57, no. 6, pp. 3436–3449, 2019.

[67] E. Casalini, J. Fagir, and D. Henke, "Moving Target Refocusing With the FMCW SAR System MIRANDA-35," *IEEE Journal of Selected Topics in Applied Earth Observations and Remote Sensing*, vol. 14, pp. 1283–1291, 2020.

[68] A. Meta, P. Hoogeboom, and L. P. Ligthart, "Signal processing for FMCW SAR," *IEEE Transactions on Geoscience and Remote Sensing*, vol. 45, no. 11, pp. 3519–3532, 2007.

[69] R. Wang, O. Loffeld, H. Nies, S. Knedlik, M. Hagelen, and H. Essen, "Focus FMCW SAR data using the wavenumber domain algorithm," *IEEE Transactions on Geoscience and Remote Sensing*, vol. 48, no. 4, pp. 2109–2118, 2010.

[70] J. De Wit, A. Meta, and P. Hoogeboom, "Modified range-Doppler processing for FM-CW synthetic aperture radar," *IEEE Geoscience and Remote Sensing Letters*, vol. 3, no. 1, pp. 83–87, 2006.

[71] A. Meta, P. Hoogeboom, and L. P. Ligthart, "Non-linear frequency scaling algorithm for FMCW SAR data," in *Proc. EuRAD*, (Manchester, UK), pp. 9–12, IEEE, Sept. 2006.

[72] A. Ribalta, "Time-domain reconstruction algorithms for FMCW-SAR," *IEEE Geoscience and Remote Sensing Letters*, vol. 8, no. 3, pp. 396–400, 2011.

[73] A. Meta and P. Hoogeboom, "Signal processing algorithms for FMCW moving target indicator synthetic aperture radar," in *Proc. IGARSS*, (Seoul, Korea), pp. 316–319, IEEE, July 2005.

[74] Y. Luo, H. Song, R. Wang, Y. Deng, and S. Zheng, "An accurate and efficient extended scene simulator for FMCW SAR with static and moving targets," *IEEE Geoscience and Remote Sensing Letters*, vol. 11, no. 10, pp. 1672–1676, 2014.

[75] P. Cheng, Q. Xin, J. Wan, and Z. Wang, "Efficient detection of ground moving targets in FMCW SAR by focusing," in *Proc. IGARSS*, (Milan, Italy), pp. 3156–3159, IEEE, July 2015.

[76] P. Cheng, Q. Xin, J. Wan, and Z. Wang, "Refocusing of ground moving targets for range migration algorithm in FMCW SAR," in *Proc. SPIE*, (Toulouse, France), pp. 1–7, International Society for Optics and Photonics, Oct. 2015.

[77] V. T. Vu, T. K. Sjogren, M. I. Pettersson, A. Gustavsson, and L. M. Ulander, "Detection of moving targets by focusing in UWB SAR——Theory and experimental results," *IEEE Transactions on Geoscience and Remote sensing*, vol. 48, no. 10, pp. 3799–3815, 2010.

[78] V. T. Vu, T. K. Sjogren, and M. I. Pettersson, "Moving Target Detection by Focusing for Frequency Domain Algorithms in UWB Low Frequency SAR," in *Proc. IGARSS*, (Boston, MA), pp. 161–164, IEEE, July 2008.

[79] V. Vu, M. Pettersson, and T. Sjögren, "Experimental results on focusing moving targets in TerraSAR-X and TanDEM-X images," in *Proc. RadarCon*, (Philadelphia, PA, USA), pp. 1–5, IEEE, May 2016.

[80] S. Stanko, W. Johannes, R. Sommer, A. Wahlen, J. Wilcke, H. Essen, A. Tessmann, and I. Kallfass, "SAR with MIRANDA-millimeterwave radar using analog and new digital approach," in *Proc. EuRAD*, (Manchester, UK), pp. 214–217, IEEE, Oct. 2011.

[81] K. Robinson and P. F. Whelan, "Efficient morphological reconstruction: a downhill filter," *Pattern Recognition Letters*, vol. 25, no. 15, pp. 1759–1767, 2004.

[82] R. Klette and A. Rosenfeld, *Digital geometry: Geometric methods for digital picture analysis*. Morgan Kaufmann, 2004.

[83] L. Xi, L. Guosui, and J. Ni, "Autofocusing of ISAR images based on entropy minimization," *IEEE Transactions on Aerospace and Electronic Systems*, vol. 35, no. 4, pp. 1240–1252, 1999.

[84] W. C. Carrara, R. S. Goodman, and R. M. Majewski, *Spotlight Synthetic Aperture Radar: Signal Processing Algorithms*. Artech House, 1995.

[85] G. Franceschetti and R. Lanari, *Synthetic aperture radar processing*. CRC Press, 1999.

[86] G. Sun, M. Xing, X.-G. Xia, Y. Wu, and Z. Bao, "Robust ground moving-target imaging using Deramp–Keystone processing," *IEEE Transactions on Geoscience and Remote Sensing*, vol. 51, no. 2, pp. 966–982, 2013.

[87] S. Brusch, S. Lehner, T. Fritz, M. Soccorsi, A. Soloviev, and B. van Schie, "Ship surveillance with TerraSAR-X," *IEEE Transactions on Geoscience and Remote Sensing*, vol. 49, no. 3, pp. 1092–1103, 2010.

[88] A. R. Brenner and J. H. Ender, "Demonstration of advanced reconnaissance techniques with the airborne SAR/GMTI sensor PAMIR," *IEE Proceedings-Radar, Sonar and Navigation*, vol. 153, no. 2, pp. 152–162, 2006.

[89] S. Zhu, G. Liao, Y. Qu, Z. Zhou, and X. Liu, "Ground moving targets imaging algorithm for synthetic aperture radar," *IEEE Transactions on Geoscience and Remote Sensing*, vol. 49, no. 1, pp. 462–477, 2010.

[90] S. Chiu, "A constant false alarm rate (CFAR) detector for RADARSAT-2 along-track interferometry," *Canadian Journal of Remote Sensing*, vol. 31, no. 1, pp. 73–84, 2005.

[91] M. Martorella and F. Berizzi, "Time windowing for highly focused ISAR image reconstruction," *IEEE Transactions on Aerospace and Electronic Systems*, vol. 41, no. 3, pp. 992–1007, 2005.

[92] F. Berizzi, M. Martorella, B. Haywood, E. Dalle Mese, and S. Bruscoli, "A survey on ISAR autofocusing techniques," in *Proc. ICIP*, (Singapore), pp. 9–12, IEEE, Oct. 2004.

[93] F. Berizzi and G. Corsini, "Autofocusing of inverse synthetic aperture radar images using contrast optimization," *IEEE Transactions on Aerospace and Electronic Systems*, vol. 32, no. 3, pp. 1185–1191, 1996.

[94] M. Martorella, "Novel approach for ISAR image cross-range scaling," *IEEE Transactions on Aerospace and Electronic Systems*, vol. 44, no. 1, pp. 281–294, 2008.

[95] M. Martorella, N. Acito, and F. Berizzi, "Statistical CLEAN technique for ISAR imaging," *IEEE Transactions on Geoscience and Remote Sensing*, vol. 45, no. 11, pp. 3552–3560, 2007.

[96] F. Berizzi, E. D. Mese, M. Diani, and M. Martorella, "High-resolution ISAR imaging of maneuvering targets by means of the range instantaneous Doppler technique: Modeling and performance analysis," *IEEE Transactions on Image Processing*, vol. 10, no. 12, pp. 1880–1890, 2001.

[97] H. Greidanus, "Satellite imaging for maritime surveillance of the European seas," in *Remote Sensing of the European Seas*, pp. 343–358, Springer, 2008.

[98] C. Noviello, G. Fornaro, and M. Martorella, "Focused SAR image formation of moving targets based on Doppler parameter estimation," *IEEE Transactions on Geoscience and Remote Sensing*, vol. 53, no. 6, pp. 3460–3470, 2015.

[99] J. N. Ash, "An autofocus method for backprojection imagery in synthetic aperture radar," *IEEE Geoscience and Remote Sensing Letters*, vol. 9, no. 1, pp. 104–108, 2011.

[100] A. Sommer and J. Ostermann, "Backprojection subimage autofocus of moving ships for synthetic aperture radar," *IEEE Transactions on Geoscience and Remote Sensing*, vol. 57, no. 11, pp. 8383–8393, 2019.

[101] X. Xu and R. M. Narayanan, "Three-dimensional interferometric ISAR imaging for target scattering diagnosis and modeling," *IEEE Transactions on Image Processing*, vol. 10, no. 7, pp. 1094–1102, 2001.

[102] H. Hellsten and L. E. Andersson, "An inverse method for the processing of synthetic aperture radar data," *Inverse problems*, vol. 3, no. 1, p. 111, 1987.

[103] S. V. Baumgartner, "Circular and polarimetric ISAR imaging of ships using airborne SAR sensors," in *Proc. EUSAR*, (Aachen, Germany), pp. 116–121, VDE, June 2018.

[104] O. Frey, C. Magnard, M. Ruegg, and E. Meier, "Focusing of airborne synthetic aperture radar data from highly nonlinear flight tracks," *IEEE transactions on geoscience and remote sensing*, vol. 47, no. 6, pp. 1844–1858, 2009.

[105] R. Horn, M. Jaeger, M. Keller, M. Limbach, A. Nottensteiner, M. Pardini, A. Reigber, and R. Scheiber, "F-SAR-recent upgrades and campaign activities," in *Proc. IRS*, (Prague, Czech Republic), pp. 1–10, IEEE, June 2017.

[106] C. Rambour, A. Budillon, A. C. Johnsy, L. Denis, F. Tupin, and G. Schirinzi, "From Interferometric to Tomographic SAR: A Review of Synthetic Aperture Radar Tomography-Processing Techniques for Scatterer Unmixing in Urban Areas," *IEEE Geoscience and Remote Sensing Magazine*, vol. 8, no. 2, pp. 6–29, 2020.

[107] G. Fornaro, F. Lombardini, A. Pauciullo, D. Reale, and F. Viviani, "Tomographic processing of interferometric SAR data: Developments, applications, and future research perspectives," *IEEE Signal Processing Magazine*, vol. 31, no. 4, pp. 41–50, 2014.

[108] M. Schmitt, *Reconstruction of urban surface models from multi-aspect and multi-baseline interferometric SAR*. PhD thesis, Technische Universität München, 2014.

[109] E. M. Domínguez, D. Small, and D. Henke, "Deriving Digital Surface Models from Geocoded SAR Images and Back-Projection Tomography," *IEEE Journal of Selected Topics in Applied Earth Observations and Remote Sensing*, vol. 14, pp. 4339–4351, 2021.

[110] X. X. Zhu and R. Bamler, "Tomographic SAR inversion by L_1-Norm Regularization — The compressive sensing approach," *IEEE Transactions on Geoscience and Remote Sensing*, vol. 48, no. 10, pp. 3839–3846, 2010.

[111] O. Frey and E. Meier, "3-D time-domain SAR imaging of a forest using airborne multibaseline data at L-and P-bands," *IEEE Transactions on Geoscience and Remote Sensing*, vol. 49, no. 10, pp. 3660–3664, 2011.

[112] F. Gini, F. Lombardini, and M. Montanari, "Layover solution in multibaseline SAR interferometry," *IEEE Transactions on Aerospace and Electronic Systems*, vol. 38, no. 4, pp. 1344–1356, 2002.

[113] M. Nannini, R. Scheiber, R. Horn, and A. Moreira, "First 3-D reconstructions of targets hidden beneath foliage by means of polarimetric SAR tomography," *IEEE Geoscience and Remote Sensing Letters*, vol. 9, no. 1, pp. 60–64, 2011.

[114] L. M. Ulander, H. Hellsten, and G. Stenstrom, "Synthetic-aperture radar processing using fast factorized back-projection," *IEEE Transactions on Aerospace and electronic systems*, vol. 39, no. 3, pp. 760–776, 2003.

[115] S. Stanko, M. Caris, A. Wahlen, R. Sommer, J. Wilcke, A. Leuther, and A. Tessmann, "Millimeter resolution with radar at lower terahertz," in *Proc. IRS*, (Dresden, Germany), pp. 235–238, IEEE, June 2013.

[116] M. Caris, S. Stanko, S. Palm, R. Sommer, A. Wahlen, and N. Pohl, "300 GHz radar for high resolution SAR and ISAR applications," in *Proc. IRS*, (Dresden, Germany), pp. 577–580, IEEE, June 2015.

[117] S.-H. Kim, R. Fan, and F. Dominski, "ViSAR: A 235 GHz radar for airborne applications," in *Proc. RadarCon*, (Oklahoma City, OK, USA), pp. 1549–1554, IEEE, Apr. 2018.

[118] J. Svedin, A. Bernland, and A. Gustafsson, "Small UAV-based high resolution SAR using low-cost radar, GNSS/RTK and IMU sensors," in *Proc. EuRAD*, (Utrecht, Netherlands), pp. 186–189, IEEE, Jan. 2021.

[119] A. Bekar, M. Antoniou, and C. J. Baker, "Low-Cost, High-Resolution, Drone-Borne SAR Imaging," *IEEE Transactions on Geoscience and Remote Sensing*, 2021.

Acknowledgements

This dissertation was funded by armasuisse W+T, the center of technology of the Swiss Department of Defense. I would like to thank Peter Wellig for his constant support and interest in the project, and all those people who have contributed to preserving the scientific collaboration between armasuisse W+T and SARLab.

I wish to express my sincere appreciation to my former supervisor, Erich Meier, for wisely guiding me through the first half of my journey, for always being supportive and motivating, and for creating a relaxed working environment at SARLab. Erich also provided the contacts and funding sources, without which this project could have not been completed.

I owe particular thanks to my current supervisor, Daniel Henke, for steering my research in the right direction and helping me reach the final milestone of this long journey. With his vast technical knowledge, original research ideas and supervision, especially when writing scientific papers, Daniel was instrumental in this project. Moreover, Daniel also provided the contacts and funding sources, without which this project could have not been completed.

I would like to thank the former chair of my promotion committee, Michael Schaepman, for his support and valuable inputs during the PhD progress meetings, and for giving me the opportunity to join the RSL. I would also like to thank the current chair of my promotion committee, Alexander Damm-Reiser, whose advice and suggestions have been of great help in improving the quality of this manuscript.

I wish to express my gratitude to Rita Ott and Sandra Altorfer, whose infinite patience and expertise made it possible for me to navigate the bureaucracies of both the University and the City of Zurich.

I would like to thank all current and former colleagues at SARLab, with whom I spent a wonderful time during the past years. Many thanks to ..

.. Elías Méndez Domínguez and Max Frioud, who were always willing to help and share their technical knowledge.
.. Christoph Rohner, Christophe Magnard, Julian Fagir and Peter Brotzer, who helped me in different ways and contributed to creating a fun working environment in the office.
.. Adrian Schubert and David Small, who were always a pleasure to interact with.

I would like to extend my thanks to all current and former colleagues at RSL and GIUZ, who made the past years truly memorable and enjoyable. Thanks to those of you who ran the SOLA races under my impeccable supervision and coordination. Thanks to those of you who played *Töggeli-chaste* with me during afternoon breaks, and inevitably lost. Special thanks to Julian and Rémy, for the deep conversations and critical reflections while eating one of the many *pizze*. Thank to all of you!

Special thanks to Liv, my roommate and habitual client of my kitchen, who, against my will, made me an expert on the on-going bark beetles infestation in the *Sihlwald* forest, and kept me smiling along the way.

Ed infine, un Grazie ad i miei genitori, a mio fratello ed a tutta la mia famiglia, che mi hanno reso ciò che sono e che mi hanno permesso di raggiungere quanto raggiunto, compresa questa tesi.

Emiliano Casalini

Wallisellenstr. 477, 8050 Zürich, Switzerland
+41 77 520 75 59 emiliano.casalini@uzh.ch

Date of birth: 13.12.1988
Place of birth: Carrara (IT)
Civil status: Single
Nationality: Italian
Residence permit: C (since 31.08.2020)

In brief

- Scientific experience in RADAR remote sensing and signal processing
- Design, planning and implementation of synthetic aperture RADAR (SAR) campaigns
- Project work with various partners (e.g., armasuisse, Fraunhofer FHR, DLR, etc.)
- Analysis of large amounts of data for interdisciplinary cooperation
- Writing publications and reports; presentations at workshops and conferences

Work experience

Research Assistant **since 01.09.2015**
University of Zurich, Remote Sensing Laboratories, Zürich (CH)

- Development of signal processing methods for refocusing moving targets in airborne SAR imagery
- Support for field campaigns
- Programming in Matlab and, seldom, in C and C++
- Regular writing of reports and presentation of scientific results at international conferences
- Teaching assistant for GEO 443 (Specialization in remote sensing: SAR and LIDAR)

Systems engineer **2015**
Thales Alenia Space, Rome (IT)

- Development and implementation of methods for evaluating the performances of the European GNSS system Galileo
- Analysis of code observables, phase observables and navigation messages to monitor the status of the system
- Programming in Matlab

Junior engineer **2014**
Navtech Radar Ltd., Ardington (UK)

- Working in the Highways department to deliver RADAR sensors for automatic detection of pedestrians, cars and debris
- Planning, implementing and reporting on the progress of Highways projects
- Systems performance analysis, diagnosing problems and proposing and/or implementing rectification action
- Coordinating problem resolution with engineering, software and customer support
- Assisting the product development team with field testing of new products

Education

Doctor of Philosophy — **since 01.09.2015**
University of Zurich, Remote Sensing Laboratories, Zürich (CH)

Master of Science in Telecommunications Engineering — **2011–2014**
University of Pisa (IT) — *110/110 cum Laude*

Bachelor of Science in Telecommunications Engineering — **2007–2011**
University of Pisa (IT) — *100/110*

High school — **2002–2007**
Liceo scientifico Guglielmo Marconi, Carrara (IT) — *87/100*

Qualifications

- **Italian:** Mother tongue
- **English:** Fluent in speech and writing
- **German:** Basic knowledge (ca. A2/B1)
- **Programming:** Very good knowledge in Matlab, basic knowledge in C and C++
- **Computer skills:** Working with LaTeX as well as Office; very good knowledge of Windows operative systems
- **Hobbys:** Bouldering, cooking, cycling

References

Daniel Henke — **Group leader at University of Zurich**
+41 44 635 65 24 *daniel.henke@geo.uzh.ch* — *since 2017*

Erich Meier — **Group leader at University of Zurich**
+41 79 574 81 20 *erich.meier@geo.uzh.ch* — *2015–2016*

Publications

Undergoing review: **Casalini, E.**, Domínguez, E. M., & Henke, D. (2021). Multi-View Three-Dimensional Radar Imaging of Moving Targets with Time-Domain Processing. *IEEE Transactions on Geoscience and Remote Sensing*.

Casalini, E., & Henke, D. (2020, September). FMCW SAR Data Inversion. In *IGARSS 2020 IEEE International Geoscience and Remote Sensing Symposium* (pp. 2117–2120). IEEE.

Casalini, E., Fagir, J., & Henke, D. (2020). Moving Target Refocusing with the FMCW SAR System MIRANDA-35. *IEEE Journal of Selected Topics in Applied Earth Observations and Remote Sensing*, 14, 1283–1291.

Casalini, E., Frioud, M., Small, D., & Henke, D. (2019). Refocusing FMCW SAR Moving Target Data in the Wavenumber Domain. *IEEE Transactions on Geoscience and Remote Sensing*, 57(6), 3436–3449.

Casalini, E., & Henke, D. (2018, July). First GMTI Results of the MIRANDA-35 Sensor. In *IGARSS 2018 IEEE International Geoscience and Remote Sensing Symposium* (pp. 5808–5811). IEEE.

Casalini, E., Henke, D., & Meier, E. (2016, September). GMTI in circular SAR data using STAP. In *2016 Sensor Signal Processing for Defence (SSPD)* (pp. 1–5). IEEE.

Staglianò, D., Martorella, M., & **Casalini, E.** (2014, October). Interferometric bistatic ISAR processing for 3D target reconstruction. In *2014 11th European Radar Conference* (pp. 161–164). IEEE.

Zürich, 31. August 2021